Note: this Thesis Contains Color Images
Please Refer to PDF Version to Identify

STUDY OF MICROALLOY PRECIPITATION IN HOT CHARGED SLABS

by
Myra S. Dyer

A thesis submitted to the Faculty and the Board of Trustees of the Colorado School of Mines in partial fulfillment of the requirements for the degree of Masters of Science (Metallurgical and Materials Engineering).

Golden, Colorado

Date: 12/20/2010

Signed: _____
Myra S. Dyer

Signed: _____
Dr. John G. Speer
Thesis Advisor

Golden, Colorado

Date: 12/20/2010

Signed: _____
Dr. Michael J. Kaufman
Professor and Head
Department of Metallurgical and
Materials Engineering

ABSTRACT

The effects of microalloy precipitation and (tunnel furnace) dissolution during direct slab production were explored relative to the position within a slab (i.e. thermal profile of the slab) and alloy content. Niobium solute contents and precipitate fractions were quantified using electrochemical extraction and inductively coupled plasma atomic emission spectrometry (ICP-AES) techniques. The locations selected for testing three experimental CMn(Nb) steels incorporated the influence of temperature differences between different locations within the slab, differing solidification rates, and alloy segregation.

Preliminary testing involved a high strength vanadium grade which was used to determine if adequate quenching occurred during sample collection. A CMn(VNb) slab was cropped at the base of the caster and prior to hot rolling. All of the vanadium remained in the steel matrix prior to hot rolling (at furnace exit), and did not prematurely precipitate during sample collection at some point in the quenching process. The quenching method was therefore considered satisfactory.

Trial heats with low, medium, and high niobium additions were then prepared. The results showed that the greatest amount of alloy precipitation occurred at the slab surface/edge/corner region of the continuously cast thin slab at the base of the caster. The extent of precipitation appeared greatest in the high niobium steel, where dissolution subsequently occurred during reheating and equalization in the tunnel furnace. There did not appear to be substantial changes (i.e. precipitation or dissolution) in the tunnel furnace for the low and medium niobium steels. The columnar region represented the bulk of the slab volume and exhibited the lowest amount of precipitated niobium. Precipitation behavior was generally consistent with expectations based on solubility considerations related to applicable thermal and compositional variations. The high percentage of niobium precipitation present in the slab edges can be understood in terms of the lower slab surface temperature and corresponding lower solubility of niobium carbonitrides. The lower temperatures of the slab surface at the base of the caster are associated with an increasing driving force for alloy precipitation, and these conditions

are conducive to precipitation in the surface/edge/corner regions. Increasing the niobium content also increases the supersaturation and allows niobium precipitation to occur at higher temperatures.

The chemical analysis results were verified via microstructural analysis using transmission electron microscopy (TEM) of extraction replicas. Precipitates were observed to be of irregular-cuboidal and cuboidal morphologies. The average precipitate diameter appeared to be smallest on the slab surface and largest in the centerline region of the slab. The average particle diameter was greatest in the high niobium steel for each process location and solidification region. The character of the precipitation volume fraction results was generally similar to the trend shown by the electrochemical dissolution results.

TABLE OF CONTENTS

LIST OF FIGURES

LIST OF TABLES

ACKNOWLEDGEMENTS

First off, I would like to give the most sincere thank you to my undergraduate research assistant, Pete Stacey. Without his help during experimental testing the extent of this project would not have been possible. His dedication and hard work is one to admire and I am truly grateful for all the knowledge and enthusiasm that he brought to this study and to the research center.

I would like to thank my committee, Dr. Speer, Dr. Matlock, and Dr. Thompson, for their support and enthusiasm. I would like to thank Dr. Speer for his guidance and encouragement throughout this project, Dr. Matlock for his interest and support during this study, and Dr. Thompson for his additional insight. I would also like to sincerely thank Dr. Speer, Dr. Matlock, Dr. Brian Thomas, Kun Xu, Steve Jansto, and Adam Shutts for their insight and invaluable support during the publication of this study.

I would also like to acknowledge the support of the sponsors of the Advanced Steel Processing and Products Research Center. Without the passion and excitement for steel from each sponsor, this opportunity would not have been possible. I would like to extend a special thank you to Steve Jansto for being an outstanding mentor and for his knowledge, excitement, and enthusiasm during the duration of this project.

To everyone at Vital Yoga, thank you for your enlightenment, compassion, and positive outlook. To all of my friends that have helped me find a balance between work and play, for your support, and for the incredible memories.

And finally, I want to thank all of my family for giving me the inspiration and encouragement needed to succeed in anything I put my mind to. I am so grateful to have such a loving family who will support me in all of my endeavors. Your love means the world to me.

Thank you for everything,

Myra

CHAPTER 1 : INTRODUCTION

HSLA steels are used in a range of applications including the construction, automotive, and pipeline industries. They are defined by the presence of small amounts of alloying additions such as niobium, titanium, and vanadium, usually in conjunction with low carbon contents. The alloying elements are usually added in amounts less than 0.1 wt. pct., levels referred to as “microalloying”. Microalloying can improve mechanical properties of HSLA steel by the contribution from precipitated carbides, nitrides, and carbonitrides. Precipitate size, distribution, volume fraction, and type are all prominent factors in influencing the microstructure and engineering performance. The precipitates retard and/or prevent austenite recrystallization and encourage precipitation hardening in the final matrix. Microalloy additions retard austenite recrystallization at low finish temperatures during hot rolling resulting in a substantially fine-grained transformation microstructure [1]. Increasing niobium additions could also promote premature precipitation prior to hot-rolling however, by increasing the driving force for precipitate nucleation and growth to occur. This would be an inefficient use of alloy additions, and thus it is necessary to better understand how compositions and processing parameters influence niobium precipitation prior to hot-rolling.

Niobium, used in amounts ranging from about 0.01 to 0.10 (wt. pct.) is usually an important component in hot-rolled linepipe steels [2]. Studies have been reported related to the understanding of niobium precipitation during hot-rolling deformation relative to austenite recrystallization and the dissolution kinetics of niobium during reheat processes [1-13]. In addition, in-depth research has been carried out to better understand the effects of microalloy precipitation on the mechanical properties of high strength microalloyed steels relative to niobium content and thermomechanical processing parameters, including Compact Strip Production (CSP) processed steels [5]. However, the literature related to niobium precipitation during solidification and processing prior to hot-rolling is more limited.

This research is directed towards understanding niobium precipitation prior to hot-rolling relative to alloy content and solidification of the slab during CSP processing of HSLA steels. The testing of steels with low, medium, and high concentrations of niobium in conjunction with variations in sampling location (i.e. base of the caster and after tunnel furnace soaking) was expected to assist in understanding and optimizing niobium additions and processing for HSLA steels. Induction coupled plasma - atomic emission spectrometry (ICP-AES) techniques were used to evaluate the amount of niobium in the steel matrix and precipitate form by use of electrochemical extraction methods. The experimental procedure and in depth chemical analyses are presented later in Chapters 3 and 4, respectively. Further, particle characterization, size distribution, and precipitation volume fraction were also of interest, and are reported in Chapter 4. Testing was specifically associated with thin slabs obtained by way of the CSP thin slab casting process. However, the results should be of interest in the broader context of hot charged HSLA steels.

CHAPTER 2 : BACKGROUND

2.1 Compact Strip Production

Thin slab casting was developed, along with the first continuous CSP casting facility, in Crawfordsville, Indiana in 1989 [19]. Considerable differences exist between the CSP casting processing of steel relative to conventional ingot or thick-slab casting procedures. CSP is a complex process that combines strand casting, hot rolling, and coiling into a single production unit. The coupling of casting and rolling minimizes energy consumption and operating costs. The CSP process has been continuously developed since its introduction in 1989 to the steel industry. The production of CSP high strength steels has provided a suitable combination of strength and toughness, and is becoming an integral part of steel manufacturing [5, 17, 21, 22]. A schematic illustration of the process is shown in Figure 2.1 [26].

The CSP process at Nucor-Hickman involves a vertical copper-nickel plated, water-cooled mold with a funnel-shaped submerged entry nozzle [27]. The vertical length of the strand is approximately 15.8 m (624 in), complete with two segments of containment rolls. Subsequent to casting, the slab begins to cool before entering the equalization furnace (tunnel furnace). The slab surface temperature entering the furnace reportedly can range from about 900 °C (1652 °F) to 1100°C (2012 °F) [19]. The tunnel furnace provides an equalization temperature of about 1150 °C (2102 °F) for about 15-20 minutes. Upon furnace exit, the outgoing slab surface temperature is about 1050 °C (1922°F)]. After passing through the equalization furnace the slab is hot rolled using five tandem finishing stands, based on the Nucor-Hickman CSP configuration.

CSP processing produces a slab thickness varying from 50 mm to 70 mm at casting speeds ranging from 3.5 to 6.0 meters per minute. This is in comparison to conventional slab casting which produces a slab thickness typically ranging from 200 mm to 250 mm at casting speeds varying between 0.75 and 1.25 meters per minute [8]. Consequently, CSP processed slabs demonstrate a significantly higher cooling rate and solidify more quickly than conventional cast slabs. As a result, the CSP processed slabs

typically display less chemical segregation and a generally more homogenous overall cast microstructure [5, 17, 20, 22]. Because of the faster solidification rate, the initial as-cast austenite grain size for the thin slab is an average 1 ± 0.4 mm, compared to 2 – 3 mm for conventional casting [24, 25]. Although the as-cast grain size is smaller for the thin slab, the grains in the conventional slab transform from austenite to ferrite upon cooling and ferrite to austenite upon heating, and undergo more deformation prior to achieving a given final product dimension. Refinement of the conventional-slab grains occurs due to these mechanisms and a smaller final grain size is observed relative to thin slabs prior to hot rolling. Further differences between conventional processing, also known as cold charge rolling (CCR), and CSP processing are found in Table 2.1, which is modified from the work of Muojekwu *et al*. [28]. Muojekwu observed that the strength of a CSP AISI 1008 steel matched a CCR AISI 1015 steel. The increase in strength was attributed to a finer grain size, higher Ni and Cr residuals, and differences in MnS.

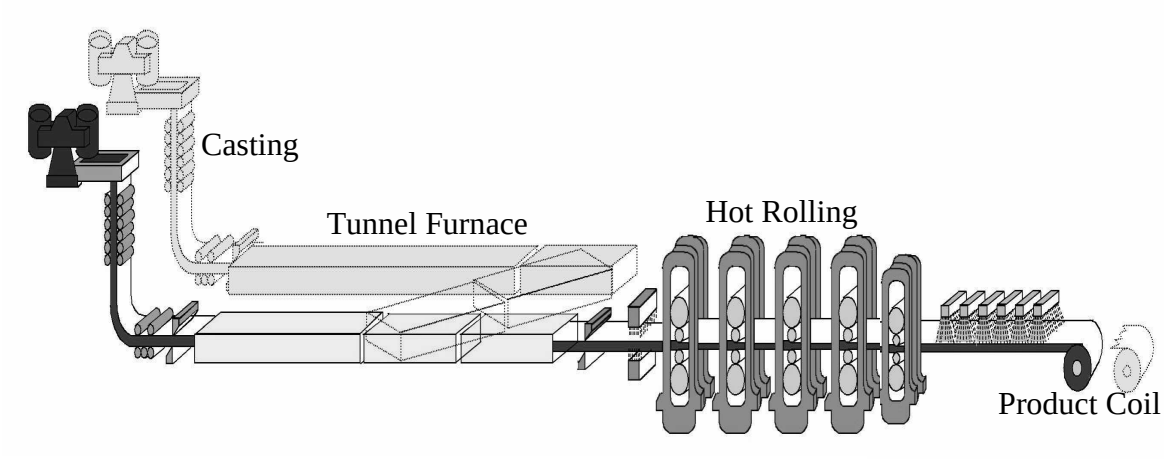

Figure 2.1 Schematic diagram of CSP process [26].

Previous research concerning the correlation between the strength of CSP steel in conjunction with lean chemistries has been conducted. It has been reported that the strengthening that occurs in CSP material is attributed to strain induced grain refinement. The amount of reduction can approximate to 2.5 times that of conventional hot-strip mill rolling for a given rolling pass [28]. For low carbon grades, precipitation hardening is an effective strengthening mechanism in addition to grain refinement [30].

Table 2.1 Comparison of CSP and CCR Processes for the Production of C-Mn Steel Strips [28].

	Cold Charge Rolling (CCR)	**Compact Strip Production (CSP)**
Steel Composition	Steel from blast furnace-BOF route followed by ladle refining. The levels of trace elements such as Al, N, Cu, Sn, Pb, Cr, Ni and Mo are more easily controlled.	Steel from EAF remelting of scrap/DRI followed by ladle refining. Higher levels of Al, N, Cu, Sn, Pb, Cr, Ni and Mo utilized.
Continuous Casting	Longer spray zone, slow solidification rate, centerline segregation and coarse as-cast grain size. AlN precipitation depends on thermal/unbending strain. AlN precipitation leads to grain boundary embrittlement and transverse cracks during casting.	Short spray zone, fast solidification rate, less segregation and finer as-cast grain size. Higher thermal strains enhance strain-induced AlN precipitation. Grain boundary embrittlement and transverse cracks more likely. Higher Cu, Sn and Pb can lead to hot shortness during casting.
Slab Reheating	Characterized by α-γ transformation, heating up to, and soaking at ~1250°C for 2-3 hours. Extensive grain growth and dissolution of precipitates. Surface layer (including shallow surface defects) converted to scale and subsequently removed by descaling.	As-cast coarse austenite. Homogenized for 12 - 20 min. at 1100 - 1150°C. Limited grain growth and dissolution of precipitates from casting. Thin adhesive scale. Surface defects remain. Cu, Cr, and Ni affect scale structure and growth.
Rolling		
Entry Microstructure	Reheated austenite at ~1250°C with finishing mill entry grain size $\leq$ 250 μm	As-cast austenite at ~1100-1150°C with ~0.6-1.4 mm grain size.
Entry Speed	~ 0.8 - 1.6 m/s into the finishing mill	~0.25 - 0.6 m/s leading to relatively lower strain rates.
Reduction	High total reduction (250 to 6 ± 4 mm) in 10 - 12 passes. Roughing ensures large reductions per pass while finishing controls the final γ-grain size and shape.	Lower total reduction (50 to 6 ± 4 mm) in 5-6 passes. Desired microstructure and shape must be achieved as the high reductions are applied during each rolling pass.
Transformation and Recrystallization	Affected by γ -grain size, cooling rate and retained strain from incomplete recrystallization in the last stands which operate at low strains.	Affected by γ -grain size and cooling rate. High reduction per pass ensures complete recrystallization at all interstand locations except the first where coarse grain size may lead to partial recrystallization.
Mechanical Properties	Determined by chemistry, ferrite grain size, ferrite fraction and free nitrogen.	Determined by chemistry, ferrite grain size, ferrite fraction and free nitrogen. Cr, Ni, and Mo microalloy additions can increase yield strength.

Additional studies on grain refinement of low carbon steel were reported by Huo *et al*. It was observed that the grain size at the center of the slab decreased after each rolling pass. The slab traveled through six separate rolling passes with a respective grain size at each pass of 41.6, 25.2, 21.4, 20.2, 13.1, and 6.7 μm [31]. For this study, two steel grades with similar chemistries were cast using conventional and continuous casting methods. The strength of the plain carbon CSP grade was nearly double that of the plain

carbon grade (Q195) produced by conventional means. Grain refinement was observed as the primary strengthening mechanism. Fast solidification rate, large reductions, and nano-sized particles (fine oxides and sulfides) contributed to grain refinement. During CSP, the solidification and cooling rate were much faster, resulting in a finer secondary dendrite arm spacing (SDAS) of the columnar zone (90-125 µm in CSP material compared to 200-500 µm in conventional material). Austenite recrystallization occurred subsequent to the first rolling pass of CSP material if exceptionally large reductions were used during the first rolling stand. Further reductions below the recrystallization stop temperature increased the strain accumulation in the austenite and increased the number of ferrite nuclei.

A study on the quality of CSP slabs reported that there was little to no chemical segregation or porosity variation relative to the through thickness of the slab [32]. The carbon, sulfur, and phosphorous amounts are demonstrated as a function of depth from the surface to the center of a CSP slab, shown in Figure 2.2. Precipitation of nano-sized particles was thought to be encouraged by microsegregation of impurities to grain boundaries during CSP processing [33].

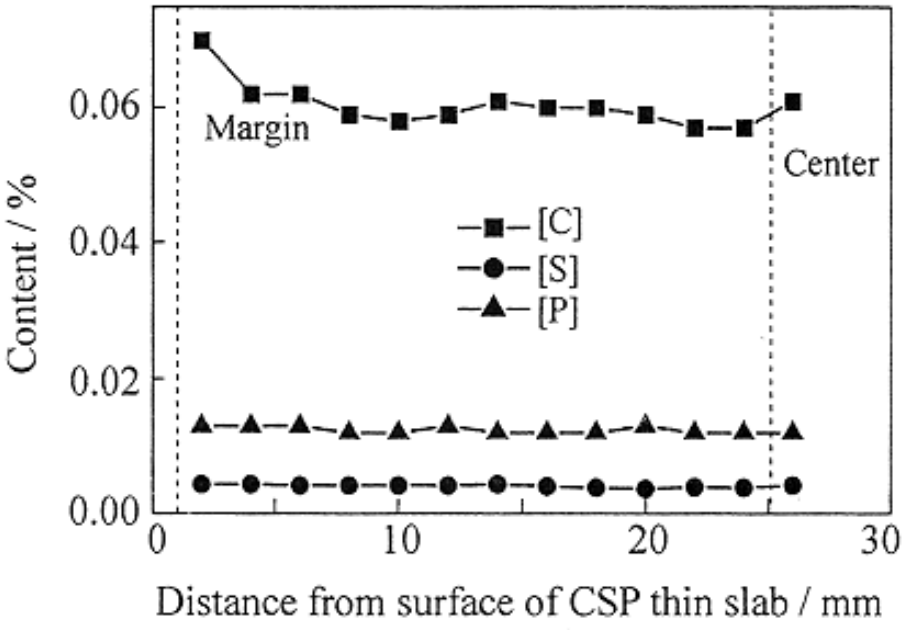

Figure 2.2 Amount of carbon, sulfur, and phosphorous relative to the through thickness of a low carbon steel produced by CSP [32].

2.2 Precipitation in Microalloyed Steels

Precipitation of carbonitrides is an important phenomenon which influences the microstructure of high-strength, low-alloy (HSLA) steels and therefore, the mechanical properties. Numerous studies have been done to better understand the precipitation behavior in microalloyed steels. The understanding of microalloy precipitation is crucial to the design of the alloy and the thermomechanical treatment necessary in order to achieve desired mechanical strengths. Several studies have related to the prediction of the chemistry and amount of precipitates formed in these steels at different temperatures [5, 26, 35, 44-46]. Optical microscopy and other techniques have been used to characterize these precipitates [47-50]. Titanium, niobium, and vanadium are the most common microalloying elements and are added in concentrations less than 0.1 wt. pct.. Microalloying elements form interstitial compounds with carbon or nitrogen in austenite (or ferrite) such as carbides, nitrides, or complex (multi-element) carbonitrides. Precipitate compounds can control austenite grain size during reheating and thermomechanical processing by pinning austenite grain boundaries and sub-boundaries and preventing recrystallization [34]. The use of microalloy additions can also increase hardenability and increase strength through precipitation in ferrite. Microalloy precipitates have a cube-cube orientation when formed in austenite, and a Kurdjumov-Sachs relationship ($[101]_{ferrite}//[111]_{MC}$; $\{111\}_{ferrite}//\{110\}_{MC}$) when formed in ferrite following the $\gamma \rightarrow \alpha$ phase transformation prior to hot rolling [35].

Austenite conditioning response is thought to be influenced by the solubility of microalloy precipitates and the amount of microalloying element in solution. The relative solubility of various carbide and nitride microalloy precipitates found by using the solubility product for the given alloy is shown in Figure 2.3 [36]. Low solubility is indicated by a low solubility product. Lower solubility is demonstrated by nitride precipitates in comparison to carbide precipitates of the same microalloying element, with titanium nitride having the lowest solubility in austenite. As the concentration of microalloy element increases, the dissolution temperature of the microalloy precipitates increases.

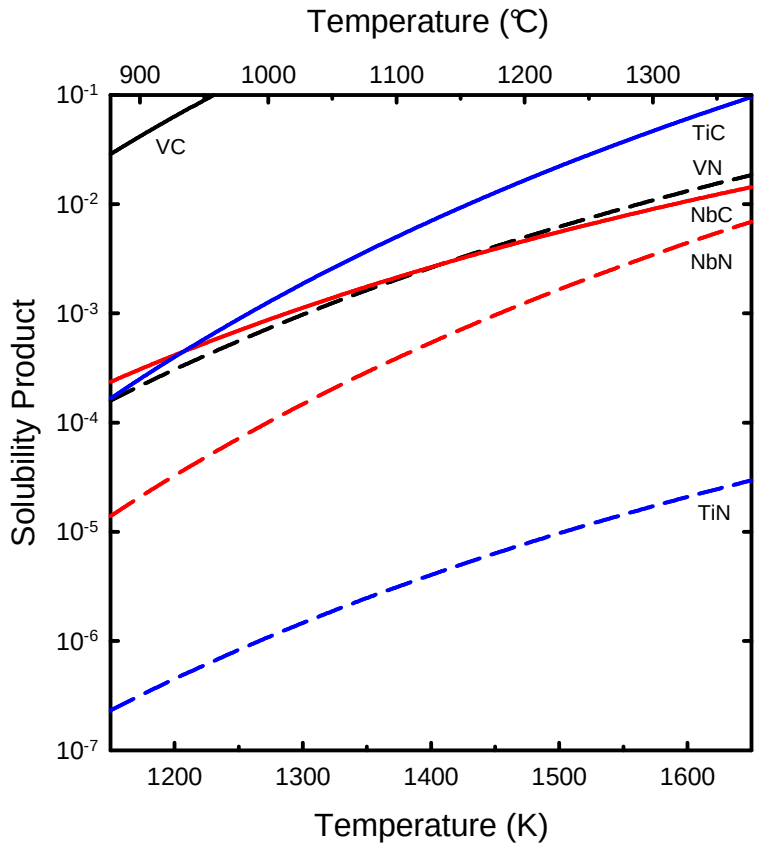

Figure 2.3 Solubility products of selected microalloy precipitates in austenite. Solubility products from [36].

Cuddy *et al*. demonstrated that the grain coarsening temperature increased approximately 200 K with an increase in niobium from 0.01 wt. pct. to 0.11 wt. pct., using a series of niobium microalloyed low-carbon steels, [12]. A similar effect has been used in industry to increase the temperature range for controlled rolling to higher temperatures (in niobium-bearing microalloyed steels) by increasing the amount of niobium [37, 38]. Other alloying elements, such as manganese, are reported to increase the solubility of niobium-rich precipitates as well as the rate of precipitation at a given temperature and prestrain, while decreasing the amount of precipitation in austenite [35, 39]. Several investigations propose that silicon can increase the rate of precipitation because of increased microalloy element diffusivities and carbon and nitrogen activities. It is also suggested that silicon decreases the solubility of niobium and vanadium carbonitrides [40-43].

Figure 2.4 is another representation of the calculated solubility products for different microalloy carbide precipitates in ferrite [51]. The carbides presented have a relatively low solubility in ferrite with niobium carbide having the lowest solubility. Microalloy carbonitride precipitates that form in ferrite or during interphase precipitation have a Baker-Nutting relationship ($[001]_{ferrite}//[110]_{MC}$; $\{200\}_{ferrite}//\{002\}_{MC}$) [52]. Microalloy precipitates that form in ferrite are often coherent with the matrix and contribute meaningfully to the strength of the steel. Precipitate size ranging from 3-20 nm has been suggested to be ideal for precipitation hardening because the corresponding interparticle spacing is most effective for hardening [53]. Observations of the precipitation contribution to strengthen Nb-Ti and V-Nb steels by Misra *et al.* showed a range of 145-260 MPa (18-46 percent of total strength) which is higher than the value of 74 MPa (11-15 percent of total strength) reported by Irvine and Baker for niobium carbide [54-56]. However, Irvine and Baker's steels contained lower niobium and carbon levels. Additional studies on the effects of precipitation in V, Nb, and Nb-Ti microalloyed steels on the relative strength caused by precipitation strengthening have reported similar values of 100-230 MPa (10-35 percent of total strength) [56, 57].

If steel is alloyed with two or more microalloying elements, complex precipitates containing multiple microalloying elements may form in austenite or ferrite [48-50, 54, 55]. Multiple alloying elements may be apparent in the complex precipitates as caps on faces of the pre-existing precipitates (e.g. Nb(C,N) nucleation on TiN) [48], by nucleation on preexisting low solubility precipitates either as a shell surrounding the precipitate (i.e. (Nb,V)(C,N) around TiN [49, 65]), or as a homogeneous mixed carbonitride (i.e. (Nb,Ti)(C,N)) [55]. Figure 2.5 illustrates some different morphologies of these complex precipitates.

Mixed carbonitrides may form in the liquid prior to austenite formation, at austenite/ferrite interfaces, or in ferrite. These mixed carbonitride precipitates can have greater thermodynamic stability compared to precipitates of a single microalloying element and consequently higher dissolution temperatures in austenite [i.e. 59, 70]. Hong *et al.* reported that cuboidal titanium-rich (Ti,Nb)(C,N) precipitates did not dissolve after reheating at 1523 K for 400 seconds despite a predicted niobium carbonitride dissolution temperature of 1467 K [60]. Approximately 8 percent of the total niobium

addition (0.0035 wt. pct. out of 0.043 wt. pct.) was measured in these undissolved precipitates [60]. Jun *et al.* reported similar fractions of precipitated niobium in solidification simulations [61]. However, it was unclear if the (Ti,Nb)N precipitates were fully dissolved and re-precipitated or if they remained undissolved throughout the entire melting/solidification cycle [61].

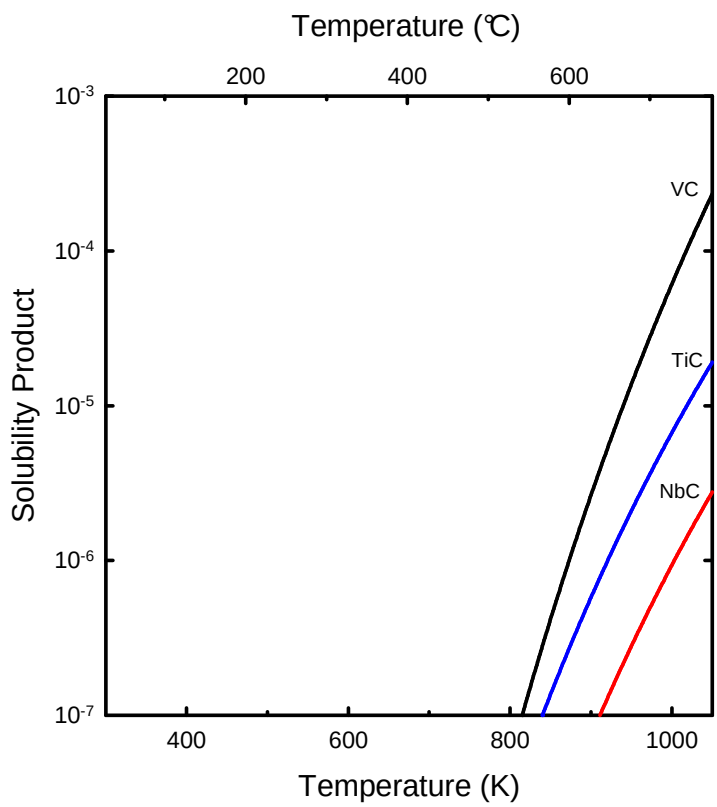

Figure 2.4 Solubility products of selected microalloy precipitates in ferrite. Solubility products from [51].

Titanium-rich (Ti,Nb)N precipitates were also described in studies by Misra *et al.* in a low-carbon steel following reheating and hot rolling as well as in a separate study of as-cast slabs [54, 55, 61]. The titanium-containing precipitates were typically in the range of 120-400 nm with morphologies including cuboidal, oblong, “triangular”, or ellipsoidal. The formation of titanium nitrides regularly occurs in the liquid steel or during solidification, and may prevent grain growth during thermomechanical processing [55]. Because TiN precipitates form in the early stages of solidification, they present a surface for nucleation of Nb(C,N).

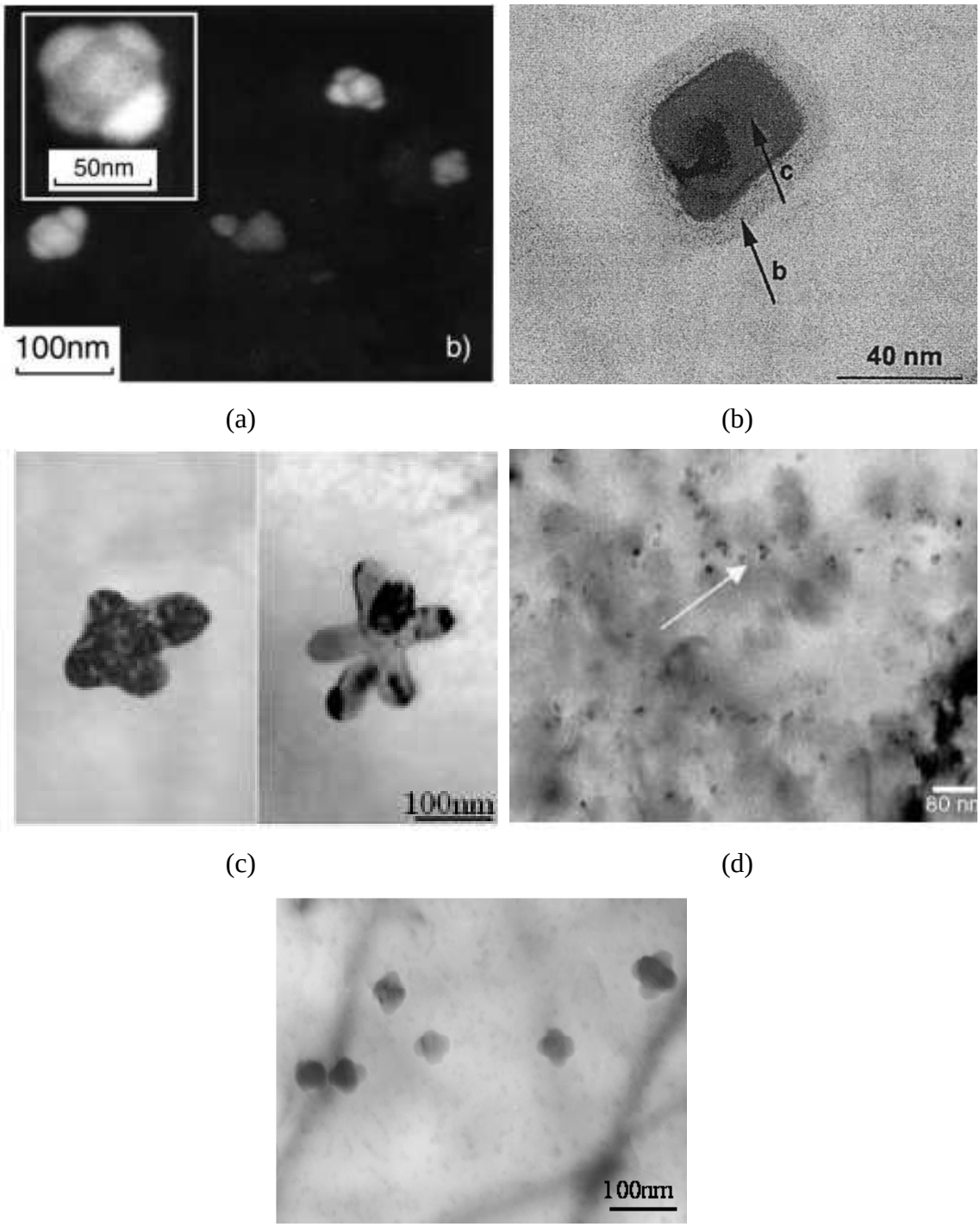

(a) (b)

(c) (d)

(e)

Figure 2.5 TEM images of complex precipitates in microalloyed steels showing (a) Nb(C,N) caps that nucleated on a TiN core [48], (b) TiN core surrounded by a shell of Nb(C,N) [49], (c) Cruciform precipitation demonstrating long arms of Nb(C,N) that nucleated on a TiN core [50], (d) strain-induced niobium-rich (Nb,Ti)(C,N) precipitates [55], and (e) cruciform complex precipitates [65].

2.3 Niobium Precipitation During Casting

Microalloying has an influential role in the production of HSLA steels. Chemical composition (i.e. microalloy concentration) is an important factor in terms of thermomechanical processing, and influences two goals concerning microstructural formation: retarding and/or preventing the recrystallization of the hot-worked austenite, especially in the late stands of the CSP rolling mill with the aim of setting a substantially fine-grained transformation microstructure, and precipitation hardening. Niobium serves each goal. It has been suggested that niobium solute retards the recrystallization of hot-worked austenite prior to alloy precipitation, as well as through precipitation on austenite substructure [9,71]. Niobium remaining in solid solution in austenite can also reduce the transformation temperature, further intensifying the grain refinement effects of microalloying [10]. Solute niobium is suggested to be more effective than solute titanium or vanadium in retarding austenite recovery [62]. Although niobium is a ferrite stabilizer and raises the A_{e3} temperature (i.e., the boundary between the ferrite + austenite and austenite phase fields), it can decrease the temperature of ferrite formation during continuous cooling due to a solute drag effects on the ferrite growth rate. On the other hand, niobium can also accelerate ferrite nucleation in conditioned austenite, due to the increased boundary surface area. Segregation and solute drag of niobium have also been reported to decrease the critical temperatures for massive transformation in ultra-low-carbon (~0.002 wt. pct.) steels [66]. Solute niobium has also been reported to retard the bainite transformation, although the effect is small [33]. When niobium is present in large undissolved precipitates, it is not available for austenite conditioning, or precipitate formation in ferrite.

Favorable sites for nucleation of niobium carbonitrides in as-cast conditions include titanium nitride or aluminum nitride particles because of the lower free energy barrier associated with creating the interface between the precipitate and matrix, and lower strain energies associated with accommodating the strain mismatch between the new precipitate and the matrix [48-50]. Multi-phase precipitates formed on pre-existing particles may take three different morphologies: cuboidal TiN with small caps or arms of Nb(C,N) on some faces (Figure 2.5a), a shell of Nb(C,N) surrounding a TiN particle (Figure 2.5b), or as cruciform-shaped precipitates with a core consisting of TiN with

multiple long arms, up to 300 nm, of Nb(C,N) (Figure 2.5c) [48-50]. Extensive precipitation of niobium on second phase particles could reduce the extent of austenite conditioning, or precipitation strengthening. Wang *et al*. examined the amount of niobium precipitated subsequent to hot rolling in an experimental Nb, Ti complex microalloyed low carbon-manganese steel (0.063 wt. pct. Nb, 0.044 wt. pct. Ti). The niobium concentration in precipitates was determined from chemical composition results from scanning transmission electron microscopy (STEM) and mass fraction from physical-chemical phase analysis. It was reported that approximately 70 percent of the available niobium can be tied up in complex Ti-Nb carbonitrides [50]. Niobium precipitation on pre-existing TiN particles typically occurs at higher temperature compared to the temperature required for isolated niobium precipitation that occurs in the matrix on dislocations and sub-boundaries [60].

Formation of single phase precipitates containing multiple microalloying elements has also been observed for strain-induced precipitation at boundaries and sub-boundaries in austenite [54, 55]. These (Nb,Ti)(C,N) precipitates are typically rich in niobium and have a spherical or irregular morphology that is common for strain-induced niobium carbonitride precipitates (Figure 2.5d).

A study completed by Hansen *et al.* using carbon extraction replica techniques on a series of niobium-bearing HSLA steels reported that no fine precipitates (<10 nm in size) were observed prior to hot rolling. It was concluded that all of the niobium dissolved at the solutionizing temperature remained in solid solution preceding hot rolling. However, undissolved coarse precipitates were observed in steels containing a higher niobium content, (0.01 wt. pct. Nb and 0.21 wt. pct. Nb), and additionally in a steel containing medium niobium levels (0.03 wt. pct. Nb), after solutionizing at a lower temperature of 1100 ºC [64]. Wang *et al.* [65] reported similar results to those explored by Hansen. As-cast Nb-Ti (0.070 wt. pct. Nb, 0.016 wt. pct. Ti) steels were produced by means of the CSP process and complex carbonitride evolution was investigated. Three types of precipitates were observed: typical cuboidal TiN particles arranged in rows with an average size of 24 nm, very fine precipitates randomly distributed in the matrix with a size range from 5-20 nm, and irregular precipitates with a slightly larger size. Figure 2.6 shows the observed precipitate types [65].

As part of transmission electron microscopy (TEM) performed on the as-cast steels [65], precipitate size distribution data of the Nb-Ti material was reported. A summary of the size distribution for the as-cast material is given in Figure 2.7. It was observed that 70 percent of the particles were in the size range of 1~36 nm, with the majority of particles ranging from 18-36 nm [65].

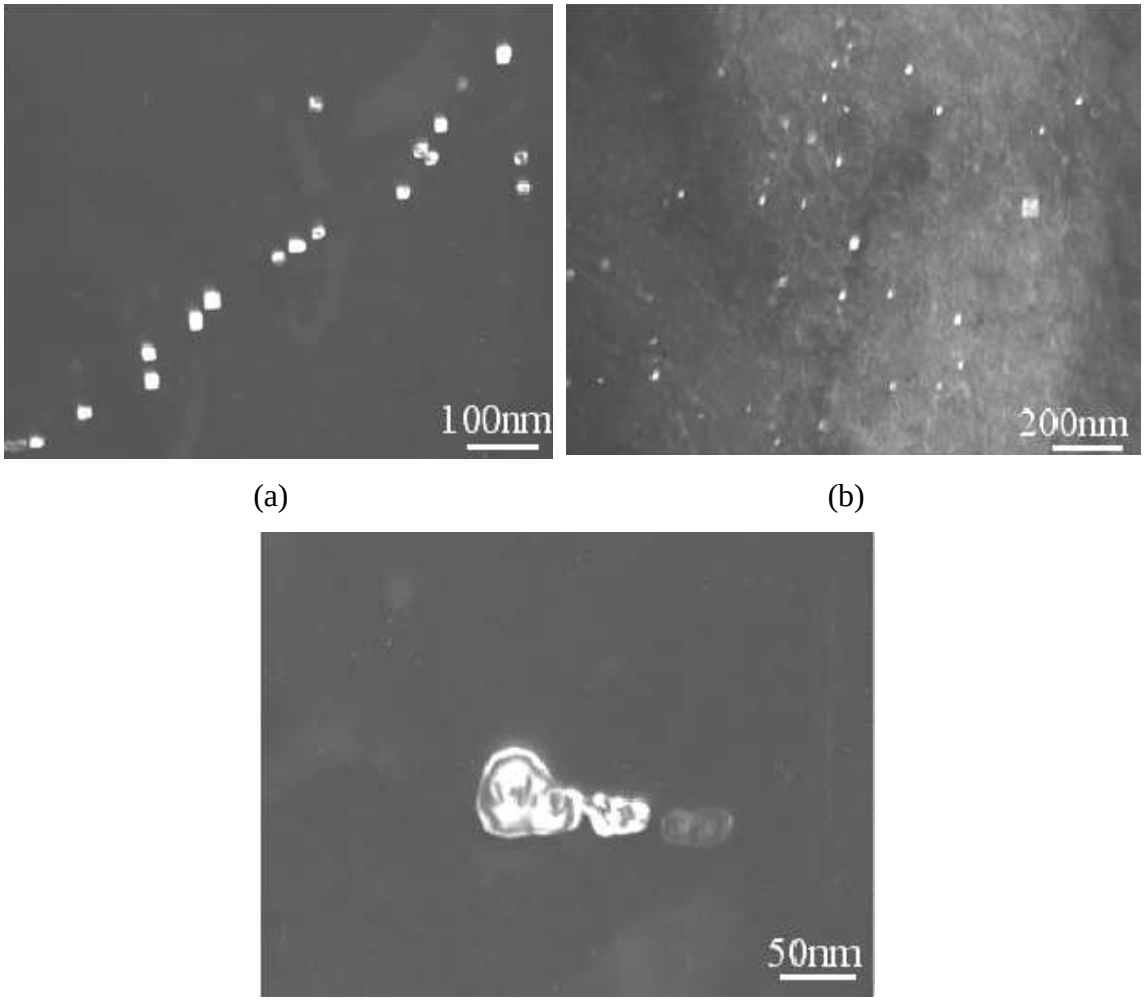

Figure 2.6 Dark field images of precipitates in the as-cast CSP slab (0.070 wt. pct. Nb, 0.016 wt. pct. Ti). (a) TiN precipitates, (b) fine precipitates, and (c) irregular precipitates [65].

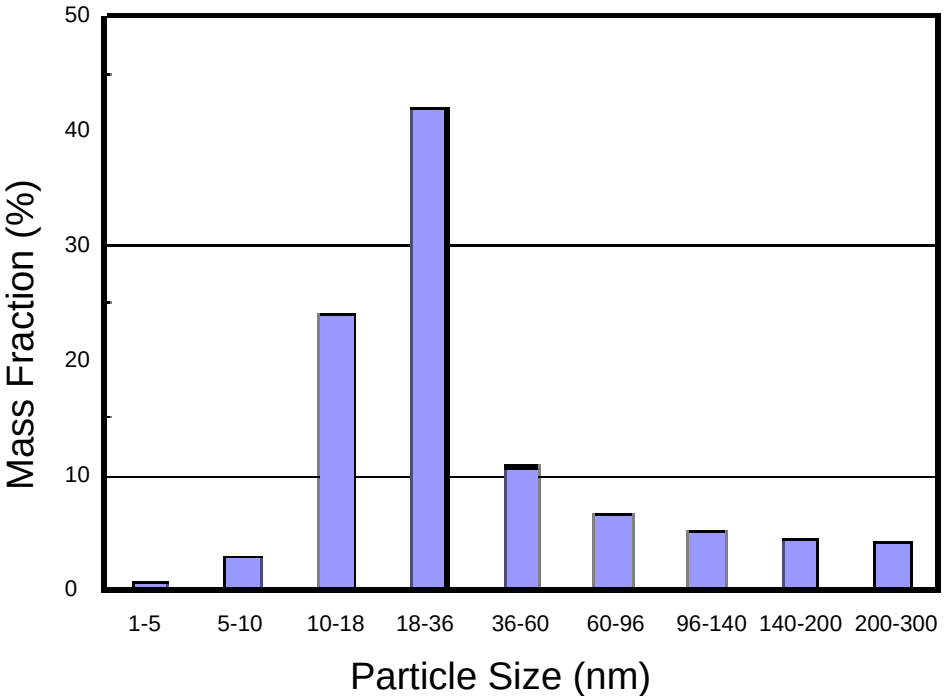

Figure 2.7 Particle size distribution for Nb-Ti CSP as-cast slab. Mass fraction plotted against particle size [65].

CHAPTER 3 : EXPERIMENTAL PROCEDURE

Numerous studies have been carried out to better understand the influence of microalloy precipitation on the mechanical properties of high strength microalloyed steels relative to niobium content and thermomechanical processing practices, where niobium is a strong grain refiner and precipitation strengthener as discussed earlier. However, studies of niobium precipitation during solidification and processing prior to hot-rolling are more limited. This research was directed towards an understanding of niobium precipitation prior to hot-rolling relative to alloy content and solidification during thin slab processing of HSLA steels. Testing was specifically associated with CSP thin slabs. However, the results should be of interest in the broader context of hot-charged HSLA steels.

The material used for microalloy precipitation studies was provided by Nucor Steel-Hickman. Electrochemical extraction techniques were used throughout this study to quantify the amount of alloy in solution and precipitate form. Preliminary testing involved a high strength vanadium-niobium grade which was used to determine if adequate quenching occurred during sample collection. Subsequent to the quenching experiment, trial heats with low, medium, and high niobium additions were prepared. The niobium trial heats were designed to study the effects of microalloy precipitation relative to alloy content, thermal profile of the slab, and process location prior to hot-rolling. Prior to niobium precipitation studies, reproducibility testing of the medium niobium trial grade was carried out to ensure that the electrochemical extraction procedure provided accurate and repeatable results. The experimental procedures are explained in the following sections.

3.1 Electrochemical Precipitate Extraction

Quantification of microalloy concentrations in solution and in precipitate form was critical to this work. Due to the dilute alloy concentrations in HSLA steels, conventional techniques have difficulty measuring the amount of microalloy in solution.

Electrochemical extraction techniques were thus employed to quantify the portions of microalloying addition dissolved in the steel matrix and in precipitate form in order to better understand niobium precipitation behavior. Previous research completed by Dr. Ana Rivas and Neal T. Porter who developed suitable electrochemical extraction techniques [7, 13, 14, 15].

3.1.1 Sample Preparation

Materials examined during this study were provided by Nucor Steel-Hickman. An in depth description of the steel used for microalloy precipitation studies will be discussed later in this chapter (Section 3.4). Samples for electrochemical dissolution were cut into approximately 13 x 13 x 2.5 mm (0.5 x 0.5 x 0.1 in) coupons. Each cut was done slowly to avoid heating during sample preparation. All cuts were made with a Leco MSX 250M2 linear sectioning saw, using a water cooled Leco 809-141 blade. The cross-section of the sample influences current density, or dissolution rate, during electrochemical dissolution, due to changes in sample resistance.

A plastic covered 18 ga. copper wire, approximately 254 mm (10 in) in length was stripped at both ends and ground using 240 grit SiC paper to ensure good connection to the steel specimen. The wire was soldered to one flat side of each 13 x 13 x 2.5 mm (0.5 x 0.5 x 0.1 in) coupon using lead-tin solder. Once the solder was cooled to room temperature, the wired samples were mounted in epoxy using 32 mm (1.25 in) molds. A sufficient amount of epoxy was used to ensure that the exposed part of the copper wire was covered, with the copper wire exiting the back of the mounted specimen. Buehler Epothin Epoxy resin and Lecoset 7007 Cold Curing Resin were used for cold mounting each specimen. The epoxy was allowed to cure for at least 8 hours. The mounted samples were then ground using 120, 240, 400, and 600 grit (water cooled) SiC paper. After grinding, samples were rinsed with water and dried with a high-pressure air jet. Samples which were prepared more than 24 hours prior to use in electrochemical tests were reground with 600 grit paper on the day of testing.

3.1.2 Electrochemical Dissolution

Electrochemical dissolution refers to dissolving the "matrix" portion of each sample using an electrochemical cell. Before dissolving, the sample was cleaned ultrasonically with methanol. After cleaning, the sample was thoroughly dried with hot air. Then it was weighed using a Scientech SA 310 balance (rated to measure up to 310g to ±0.0001g). After recording the sample mass, it was immersed in a 200 ml aqueous solution of 5 pct. hydrochloric acid and 3 pct. tartaric acid in a 90 mm (3.5 in) diameter, 50 mm (2.0 in) tall Pyrex 3140 evaporating dish. The evaporating dish and sample were placed inside a larger glass electrochemical cell with three circular openings and one half sphere opening. The purpose of using the evaporating dish in the larger cell was to reduce the amount of solution produced, while still providing enough room for the sample and electrodes. A picture of this cell set up is shown in Figure 3.1.

The wired sample (placed in the center position) acted as the working electrode in this cell. In addition to the sample, three other inputs were required. First, a 150 mm (5.91 in) platinum wire was attached to platinum mesh, which represented the counter electrode. The counter electrode completed the electrical circuit that allowed the cell to work. Platinum wire and mesh were chosen because they are inert and resistant to chemical attack in weak acid solutions. Second, a Princeton Applied Research K0077 Saturated Calomel Reference Electrode was used. The reference electrode measured the potential of the solution as compared to a standard mercury/mercury-chloride connection. To protect the reference electrode, a Luggin capillary probe was used. Use of a capillary probe allowed the reference electrode to be placed in a clean solution, but still be in contact (through a capillary) to the solution near the sample. Separation between the reference electrode and the solution was necessary because contamination or drying of the reference electrode tip could potentially lead to unstable readings. The Luggin capillary probe was attached to the half sphere opening with a metal clip. Finally, an argon bubbler with a porous ceramic tip was used, in order to both stir the solution and displace oxygen [7].

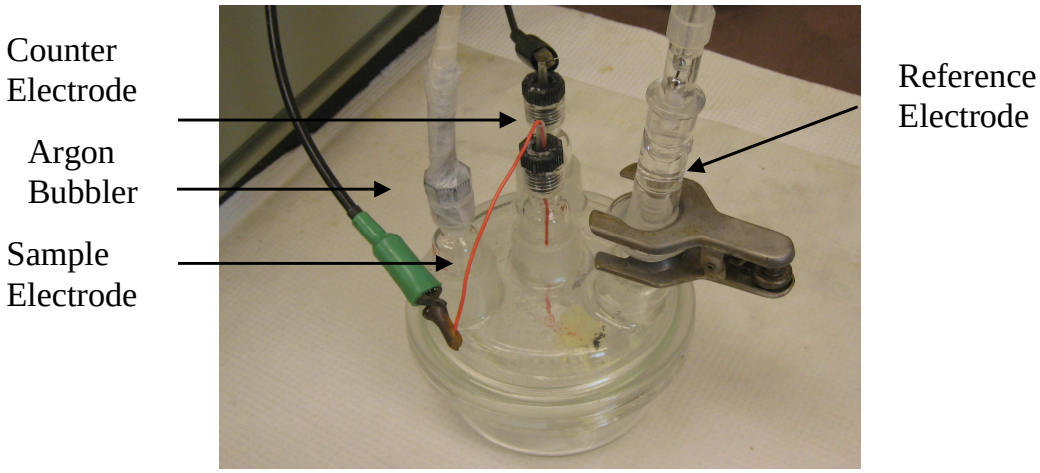

Figure 3.1 Electrochemical cell used for dissolution [7].

The three electrodes were attached to an EG and G Princeton Applied Research Potentiostat/Galvanostat Model 273. The argon flow was set at a rate which produced small bubbles over most of the solution, and induced a stirring motion. The potentiostat was set to run at a constant applied voltage of -0.150 volts. Once the potentiostat was running, the time was recorded. If the test was running properly, a stable voltage and relatively stable amperage (0.1-0.3 A) were observed. In addition, formation of small bubbles was observed on the counter electrode (platinum mesh). Each test was run for 10 hours. During the course of the 10 hours, the exposed metal surface of the sample was observed to turn black, and black particles accumulated in the solution. The undissolved particles remaining after electrochemical extraction are shown in Figure 3.2. When the test was complete, the test solution was transferred to a 400 ml beaker. The sample was placed in the beaker containing the test solution and the beaker was positioned in an ultrasonic cleaner for 5 minutes. The electrodes, evaporation plate, electrochemical cell, and sample were rinsed with deionized water over the beaker containing the test solution to ensure that no particles were lost during cleaning. The sample was then removed from the solution, and rinsed with deionized water and methanol. After rinsing, the sample was dried thoroughly with hot air and weighed, to quantify the total mass lost during dissolution. The solution was covered with two layers of Parafilm "M" laboratory film to prevent evaporation until the solution was filtered [7].

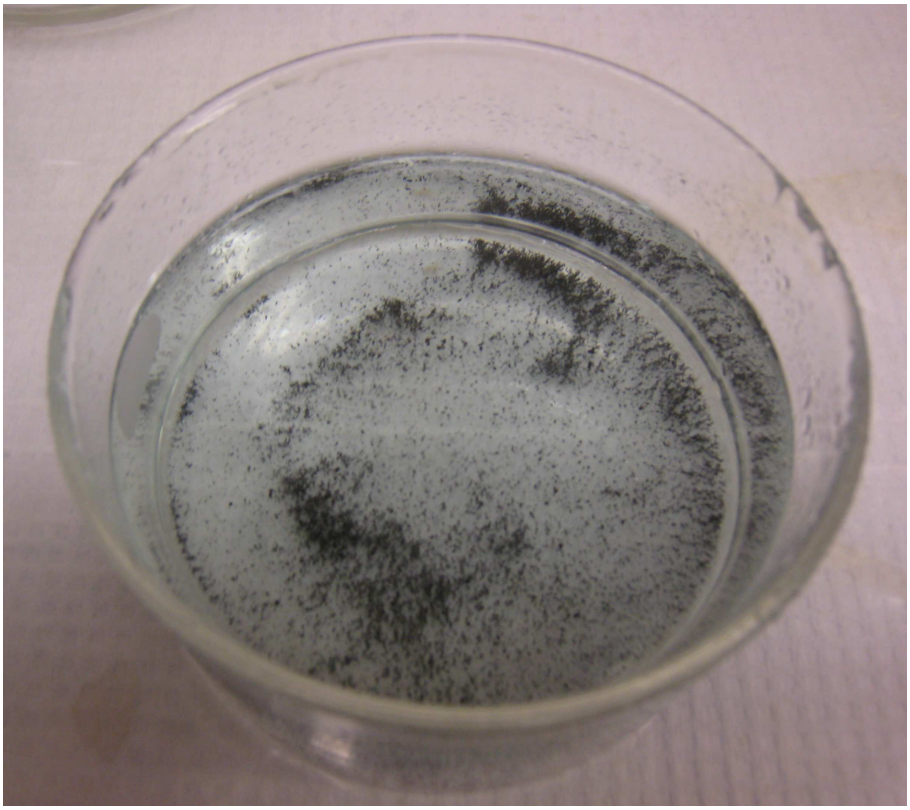

Figure 3.2 Solution of hydrochloric acid and tartaric acid containing the dissolved steel matrix and undissolved precipitates after electrochemical dissolution [7].

Samples from a preliminary quenching trial (discussed later in Section 3.3) used the potenitostat as the sole power supply. However, alternate arrangements were made for the later microalloy precipitation studies due to the large number of samples (approximately 200) tested. The large number of samples for electrochemical extraction for the niobium trial steels in conjunction with the time available for electrochemical testing required that two tests be run simultaneously. Because only one EG and G Princeton Applied Research Potentiostat/Galvanostat Model 273 was available, the niobium precipitation studies used two BK precision 1735A: 30V/3A DC power supplies. The electrochemical cell was set up as discussed previously, except the use of the Princeton Applied Research K0077 Saturated Calomel Reference Electrode was unnecessary when using the DC power supplies. Parafilm “M” film was placed over the half sphere opening where the Luggin capillary probe would have been located to ensure that no solution was lost during electrochemical extraction. Reproducibility testing

(discussed in Section 4.1) was conducted using the DC power supplies to make certain that the results were comparable to those completed using the potentiostat.

3.1.3 Filtration Method

The solution produced by electrochemical dissolution contained the dissolved steel matrix and undissolved precipitates. In order to determine the different amounts of niobium in the dissolved steel matrix and in the undissolved particles, it was necessary to filter the particles out of the solution. Vacuum filtration was used. A polycarbonate filter system was used to hold 47 mm (1.9 in) diameter millipore nitrocellulose filters. The filter holders contained the filter between two plastic grates. Two rubber gaskets were used to prevent leakage. The filter and holders were mounted to a 250 ml heavy walled vacuum flask, using a #6 ceramic stopper and Parafilm "M" laboratory film. A Gast Model DOA Oil-less Diaphragm Vacuum Pump was attached to the vacuum flask's detachable plastic side arm using nalgene reinforced PVC tubing with a 7.9 mm (0.3 in) inner diameter. The filtration setup is illustrated in Figure 3.3(a).

The filtering method required three separate steps: the first two steps used a 0.45 μm pore size, and the third used a 0.22 μm pore size. The selection of filter pore sizes was based on prior research [13], which demonstrated that using smaller filter pore sizes did not significantly change the amount of precipitate collected during filtration. Each filtering step resulted in a visible layer of precipitate residue on the filter. A photograph of the precipitate residue is shown in Figure 3.3(b).

The beaker used to hold the dissolved steel matrix solution was rinsed twice with deionized water after the solution had been completely filtered. The rinse water was filtered last, and additional deionized water was run though the filter. The vacuum flask was rinsed with deionized water after the solution was transferred back to the 400 ml beaker for each filtering step. When the filtering was complete, the filters were placed in a 200 ml Berzelius tall form beaker and dried at a low setting (35ºC) on a hot plate. The beaker was sealed with a layer of Parafilm "M" laboratory film for storage until the filters were dissolved [7].

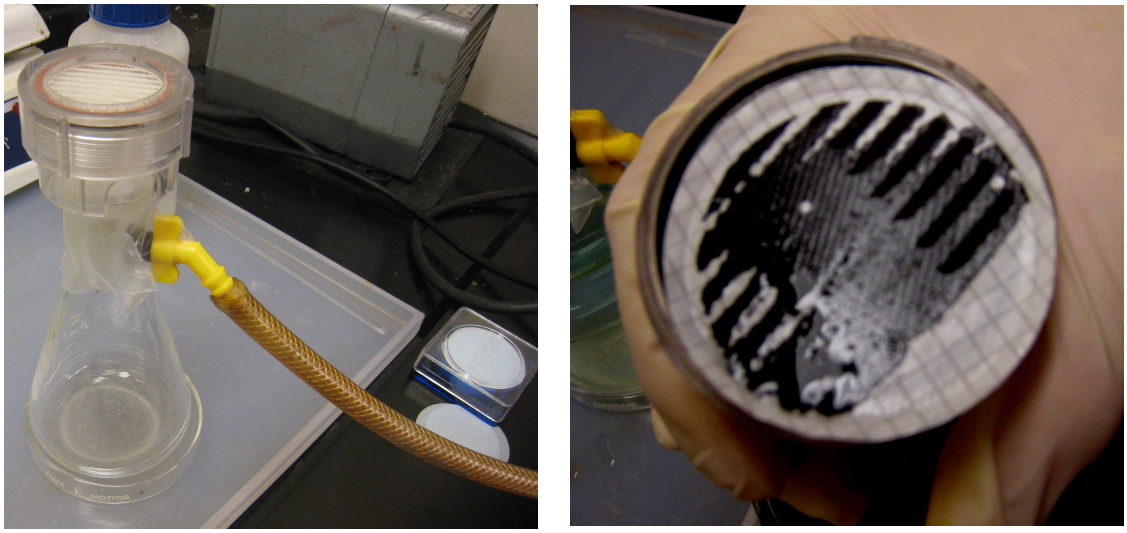

(a) (b)

Figure 3.3 (a) Filtration method used to separate the dissolved steel matrix and undissolved precipitates (b) Undissolved precipitate residue [7].

The filtered solution was transferred to a 500 ml (±0.20 ml) volumetric flask. The solution was diluted to 500 ml using deionized water. The diluted solution was then transferred to nalgene bottles for storage until further analysis was preformed. The nalgene bottles were rinsed with a small amount of the solution to prevent contamination or further dilution.

The precipitate particles were firmly attached to the dried nitrocellulose filters; therefore the filters and precipitate particles were dissolved together. All three filters from each specimen were dissolved in the same 200 ml Berzelius tall form beaker they were stored in to ensure that any particles that attached to the sides of the beaker during drying would not be lost. The filter papers and precipitate residue were dissolved using a heated solution containing hydrogen peroxide, sulfuric acid, and nitric acid. After the solution cooled, it was transferred to a 100 ml volumetric flask, and diluted to 100 ml (± 0.08 ml) with deionized water. As with the solution containing the dissolved steel matrix, the solution containing the dissolved precipitates was stored in nalgene bottles. The bottles were first rinsed with a small amount of the solution to prevent contamination or dilution.

3.2 Induction Couple Plasma – Atomic Emission Spectrometry

In order to quantitatively measure the amount of niobium in solution and in precipitate form, inductively coupled plasma – atomic emission spectroscopy (ICP-AES) was performed. In this method, the wavelength and intensity of light emitted by a solution being transferred through a plasma torch are measured. Both the dissolved steel matrix (niobium in solution) and dissolved filtrate (niobium in precipitate form) solutions were analyzed. Analysis was performed with a Perkins Elmer Atomic Emission Inductively Coupled Plasma Spectrometer.

For this analysis, the diluted solutions were transferred to 15 ml centrifuge tubes. The use of the centrifuge tubes allowed a preprogrammed robotic sipper to sample each specimen as part of an automated process. This analysis process was based on a default analysis procedure set up by the CSM Chemistry Department that was modified to include niobium. A series of standards with known chemical compositions were used to calibrate the equipment. A 10 ppm niobium standard was used to accurately identify the amount of niobium within each solution.

During analysis, the amount of instrument drift was checked, based on standard scandium levels. Additionally, a set of standard analysis samples were checked intermittently during testing. If the deviation of the standards from expected values was too large, the run was restarted. The results of the analysis were reported in concentration units of mg/L. This concentration value was used to calculate an amount of niobium, based upon the mass of sample dissolved, and the amount of dilution used. To calculate the amount of niobium measured by ICP-AES, it is necessary to multiply the concentration by the volume of the solution being analyzed:

$$Nb\ in\ solute\left(\frac{mg}{L}\right)\times 0.500L \tag{3.1}$$

$$Nb\ in\ precipitate\left(\frac{mg}{L}\right)\times 0.100L \tag{3.2}$$

The sum of the two niobium amounts in Equations 3.1 and 3.2 gives the total niobium measured, in milligrams, using ICP-AES analysis. The total value is then divided by the measured mass removed from the sample during electrochemical extraction, giving the

total amount of alloy found by ICP-AES in wt. pct.. The chemical analysis completed by ICP-AES can also be compared to the reported alloy content given by the steel producer. This comparison can be represented as a percentage difference:

$$\left(\frac{ICP\ Total\ \ Nb(wt\%) - Nb\ reported(wt\%)}{Nb\ reported(wt\%)}\right)\times 100 \tag{3.3}$$

With respect to Equation 3.3, a negative percentage difference indicated that ICP-AES measured less alloy than expected, potentially demonstrating alloy depletion. In turn, a positive percentage difference indicates that the ICP-AES measurement is greater than the expected amount of alloy indicating a potentially alloy rich region.

3.3 Preliminary Quenching Trial

The HSLA steels used for this study were provided by Nucor Steel-Hickman. Preliminary testing involved a high strength CMn(VNb) grade which was used to determine if adequate quenching occurred during sample collection. The quenching method was considered satisfactory if all the vanadium remained in solution during quenching, avoiding premature precipitation during sample collection. A CMn(VNb) slab was cropped at the base of the caster and prior to hot rolling. Additional samples were also taken from the inner diameter and outer diameter of the coil product. Figure 3.4 is a schematic illustration of the continuous casting process, where the stars indicate both process locations examined. The steel contained niobium and vanadium levels of 0.04 and 0.047 (wt. pct.), respectively. This steel was specifically chosen due to its vanadium alloying addition. Since vanadium is expected to remain in solution at all temperatures experienced during casting, quenching of the slab crop was to be considered satisfactory if all vanadium remained in solution. In order to verify the sample collection and quenching techniques before additional trial heats were prepared, the amount of vanadium in solution and in precipitate form was quantified using electrochemical extraction.

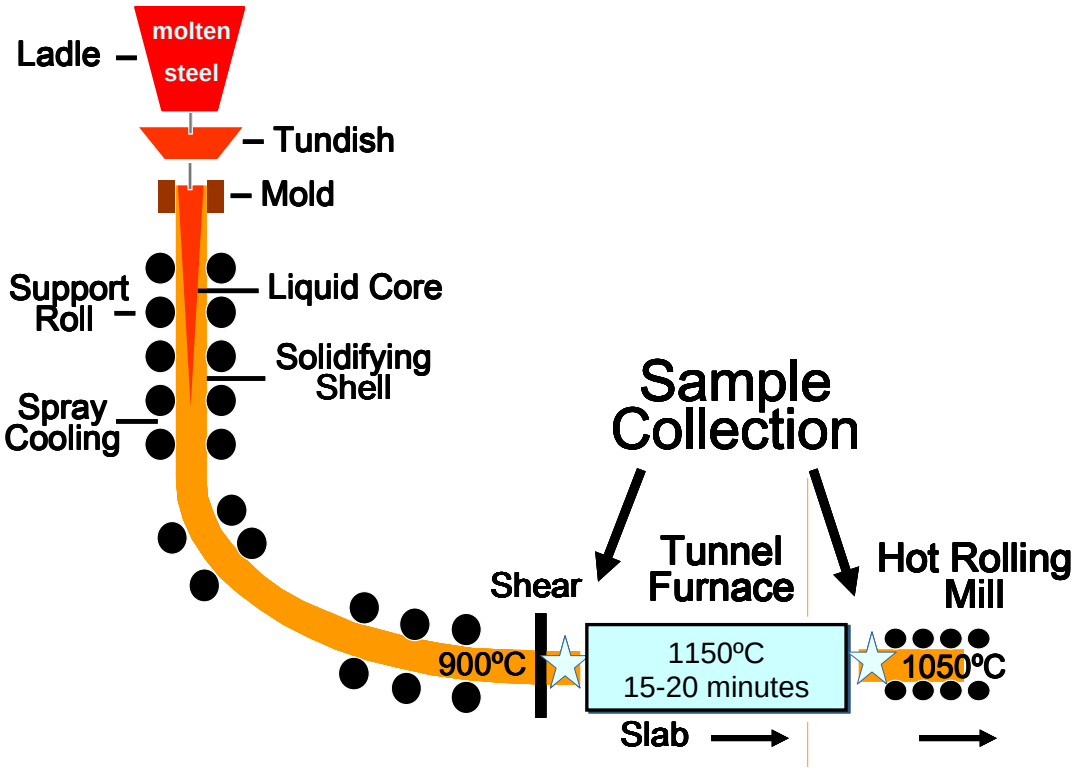

Figure 3.4 Schematic of process locations for the study of microalloy precipitation prior to hot rolling.

3.3.1 Material for Preliminary Quenching Trial

The chemical composition of the CMn(VNb) steel is shown in Table 3.1. The surface temperature of the thin slab at the base of the caster was approximately 900 ºC and prior to hot rolling was approximately 1050 ºC at the furnace exit. The slab traveled through an equalization tunnel furnace for approximately 15-20 minutes prior to hot rolling. The temperature of the tunnel furnace was approximately 1150 ºC. The steel was cast at a speed of approximately 5 m/min (190 in/min) with a slab thickness of 51 mm (2 in). The initial width of the mold at the time of casting was recorded as 1.55 m (61 in). Sample collection was possible with the use of a flying-shear at the Nucor Steel-Hickman facility at both the base of the caster and prior to hot rolling. Following shear cutting, the slabs were quenched in water. The water was highly agitated using high pressure hoses to reduce the likelihood of premature precipitation during sample collection. The processing parameters were monitored to ensure that casting conditions were consistent throughout sample collection. The sample collection technique was

employed at both the base of the caster and prior to hot rolling, subsequent to the tunnel furnace exit.

Each slab was approximately 1500 x 700 x 50 mm (60 x 28 x 2 inches) when cropped. Figure 3.5(a) illustrates the final dimensions of the cropped section. The 127 mm (5 in) longitudinal section parallel to the 1500 mm (60 in) edge was cut following sample collection to allow for easier handling and transit. The area of sample collection within the cropped slab was chosen to avoid any effects that may have occurred near the sheared edge. The 127 mm (5 in) section was then cut into five separate pieces with dimensions 300 x 127 x 50 mm (12 x 5 x 2 inches) as shown in Figure 3.5(b). Three separate solidification regions within the slab, discussed in Section 3.4, were examined. The circled section in Figure 3.6(a) was used to obtain the three sampling locations. The sample locations for preliminary tests are shown in Figure 3.6(b). Locations A, B, and C were tested from both process locations, 305 mm (12 inches) from the (narrow face) of the slab edge.

Table 3.1 Chemical Composition of CMn(VNb) Steel (wt %) for Quenching Trial

	C	Mn	Si	Ni	Cr	Mo	Ti	Nb	V	Al	N	S	P
Med Nb	0.040	1.265	0.204	0.035	0.043	0.008	0.004	0.040	0.047	0.031	0.007	0.001	0.011

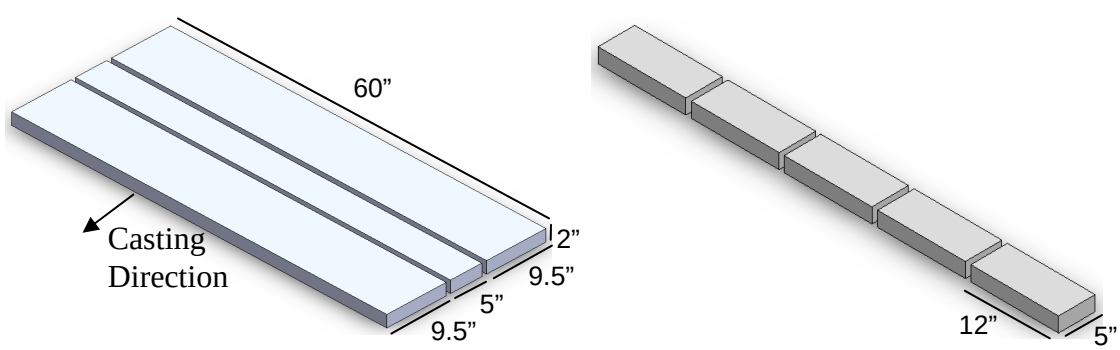

(a) (b)

Figure 3.5 On the left (a), initial slab dimensions (in inches) after cropping at the base of the caster and just prior to entry into the roll mill. Five inch middle region illustrates the location within the slab of the delivered material for easier handling. To the right (b), delivered material dimensions.

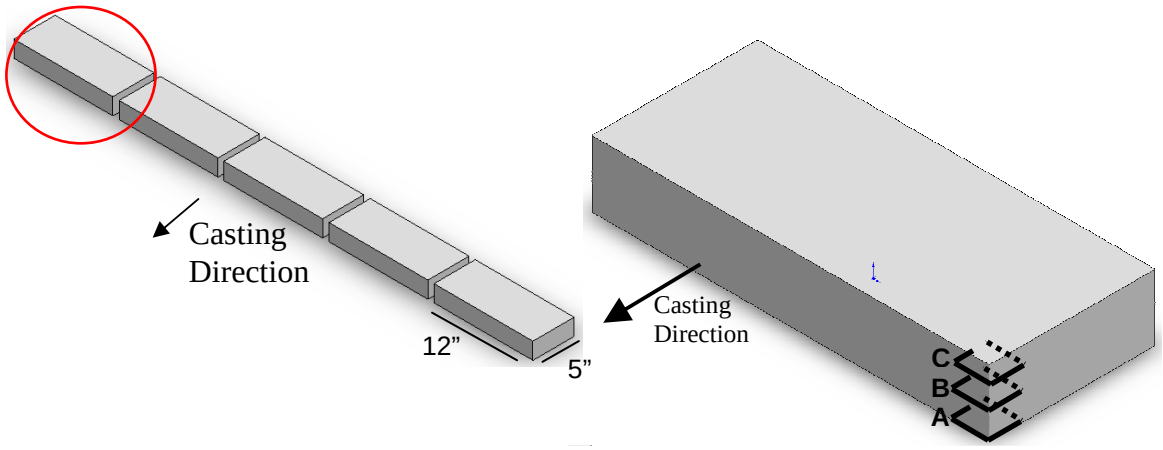

(a) (b)

Figure 3.6 Sample locations for preliminary testing. The circled section in (a) was used to obtain the three sampling locations. Locations A, B, and C in (b) were tested from the base of the caster and prior to entry into the rolling mill.

3.3.2 Results for Preliminary Quenching Trial

The specified locations of samples A, B, and C were chosen to evaluate microalloy precipitation trends relative to the thermal profile of the slab (i.e. different solidification regions prior to hot rolling). Sample A is on the surface of the thin cast slab, B represents the centerline of the slab, while C encompasses the columnar region of the cast slab approximately 13 mm (0.5 inches) below the top surface. The preliminary tests were specifically intended to determine whether or not the method for sample collection during continuous casting was adequate.

The results for vanadium precipitation from preliminary testing are shown in Table 3.2. The position of each sample relative to casting direction and specimen location within the slab is shown in Figure 3.6. One sample was tested at each location. It was observed that all of the vanadium remained in solution at the base of the caster for each sampling location. At the slab surface, 15 percent of vanadium precipitated through the tunnel furnace, while nearly all vanadium remained in solution in the columnar and centerline sampling locations. Nearly all of the vanadium remained in solution at the inner diameter (ID) of the coil. However, close to 30 percent of the vanadium precipitated in the outer diameter (OD) location. It was concluded that essentially all of the vanadium remained in the steel matrix prior to hot rolling, and did not prematurely

precipitate upon sample collection during the quenching process. Thus, the quenching method used for sample collection was considered suitable.

Table 3.3 presents the electrochemical extraction results for niobium precipitation in the preliminary CMn(VNb) steel. It is observed that approximately 30 percent of the niobium precipitates in the columnar and centerline regions of the slab through the tunnel furnace. However, the slab surface showed that nearly 50 percent of niobium precipitated through the tunnel furnace. The specimen located on the OD of the coil showed the highest amount of niobium precipitated (80 percent). The greater amount of precipitation in product material along the OD could be due to temperature and cooling rate differences.

Table 3.2 Vanadium Measured in Solution and Precipitate Form in CMn(VNb) - Quenching Trial

Sample	Precipitate (wt% V)	Solution (wt% V)	Total (wt% V)	Percentage of V precipitated	Percentage of V in solution	Reported Alloy Content (wt% V)	Precentage Difference
Caster A	0.000	0.023	0.023	0	100	0.047	-51
Caster B	0.000	0.062	0.062	0	100	0.047	32
Caster C	0.000	0.039	0.040	0	100	0.047	-16
Furnace Exit A	0.004	0.019	0.023	16	84	0.047	-51
Furnace Exit B	0.002	0.042	0.043	4	96	0.047	-8
Furnace Exit C	0.000	0.025	0.025	1	99	0.047	-47
ID of Coil	0.000	0.027	0.027	1	99	0.047	-42
OD of Coil	0.011	0.029	0.039	27	73	0.047	-16

Table 3.3 Niobium Measured in Solution and Precipitate Form in CMn(VNb) - Quenching Trial

Sample	Precipitate (wt% Nb)	Solution (wt% Nb)	Total (wt% Nb)	Percentage of Nb precipitated	Percentage of Nb in solution	Reported Alloy Content (wt% Nb)	Precentage Difference
Caster A	0.001	0.016	0.017	8	92	0.040	-58
Caster B	0.002	0.042	0.044	5	95	0.040	10
Caster C	0.002	0.026	0.028	7	93	0.040	-30
Furnace Exit A	0.016	0.011	0.026	60	40	0.040	-34
Furnace Exit B	0.007	0.021	0.028	25	75	0.040	-31
Furnace Exit C	0.005	0.012	0.017	28	72	0.040	-58
ID of Coil	0.005	0.010	0.015	32	68	0.040	-62
OD of Coil	0.020	0.005	0.025	80	20	0.040	-37

3.4 Material for Niobium Studies

Research trial heats with low, medium, and high niobium additions and similar levels of carbon, manganese, silicon, aluminum, and nitrogen were prepared. The steels were designed to evaluate the extent of niobium precipitation prior to entry into the hot

rolling mill relative to position within the slab (i.e. thermal profile of the slab) and alloy content. The three steels were cast sequentially, to ensure that processing parameters at the time of casting were equivalent. For each steel grade, samples were taken at the base of the caster and prior to entry into the rolling mill. The sample collection method developed during the quenching trials was used for the sample collection of the research trial steels. Slab dimensions were approximately 1500 x 700 x 50 mm (60 x 28 x 2 inches) when cropped. The surface temperature of the thin slab at the base of the caster was approximately 900 ºC, and approximately 1050 ºC prior to hot rolling. The equalization temperature of the tunnel furnace was approximately 1150 ºC, and the soaking time was about 20 minutes. The chemical compositions of the three CMn(Nb) steels are shown in Table 3.4. Equilibrium Nb(C,N) precipitate fractions shown in Figure 3.7, as a function of temperature, were calculated using the method of K. Xu *et al.* [16].

Table 3.4 Chemical Compositions of CMn(Nb) Steels (wt. pct.) for Microalloy Precipitation Studies

	C	Mn	Si	Ni	Cr	Mo	Ti	Nb	V	Al	N	S	P
Low Nb	0.035	0.937	0.152	0.030	0.034	0.009	0.002	0.014	0.002	0.027	0.007	0.002	0.011
Med Nb	0.036	1.065	0.184	0.030	0.029	0.010	0.002	0.030	0.002	0.029	0.008	0.002	0.009
High Nb	0.031	1.039	0.194	0.031	0.032	0.010	0.003	0.046	0.001	0.031	0.006	0.003	0.012

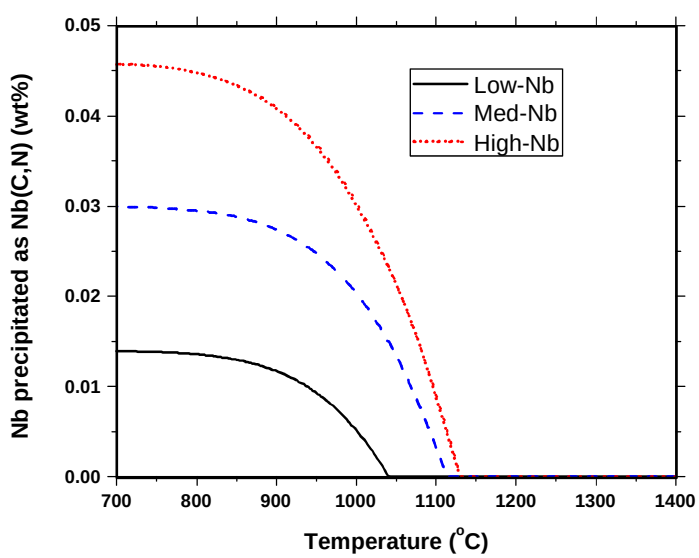

Figure 3.7 Calculated wt. pct. Nb precipitated as a function of temperature for low, medium, and high niobium additions [16].

The influence of temperature differences between varying locations within the slab and solidification rates are of special interest. Effects of alloy composition and temperatures relative to casting and equalization constitute an important aspect of this work. Different areas within a continuously cast slab were studied and characterized with respect to niobium precipitation. These areas include the chill zone, columnar zone, and central equiaxed zone. Brimacombe described the characteristics of different solidification regions and locations of special interest relative to continuous casting of thin slabs [17]. When casting thin slabs, the first solid forms along the mold wall or just below the mold perimeter and acts as a shell. From the newly solidified shell, solidification continues inward towards the center of the slab. Over time, the shell thickness increases as the solidification rate decreases within the slab. This decrease in solidification rate is caused by the outer shell acting as a barrier to heat flow from the core. Previous research reported by Brimcombe on continuous casting of thin slabs, subdivides the specific solidification regions and intended locations of special interest relative to slab cooling for this research [17]. The chill zone of the slab results from rapid solidification and steep thermal gradients experienced at the slab surface. The columnar zone is an area of dendritic growth where crystals grow from the outer shell inward toward the equiaxed zone. The equiaxed zone is a region located in the middle of the slab where equiaxed grain growth occurs. Equiaxed grain growth is caused by independent crystal growth that occurs in the last liquid remaining in the core of the slab.

The different solidification regions and specimen orientation in each sample region are illustrated in Figure 3.8. The separate locations selected for testing the experimental CMn(Nb) steels incorporate the influence of temperature differences between different locations within the slab, solidification rates, and alloy segregation. The circled section in Figure 3.8(c) was the segment of slab from which samples were obtained. Figure 3.8(d) presents the sampled regions and orientations examined in this study. Sample location A was specifically from the slab corner region and was chosen to observe the extent of microalloy precipitation on the slab surface. Location B was within the centerline region. This location helped determine the amount of alloy segregation present in the centerline of the slab and the degree of alloy precipitation. Sample location C was within the columnar region. A comparison of the results between samples A, B,

and C addresses the influence of cooling rate and temperature differences between different locations within the slab.

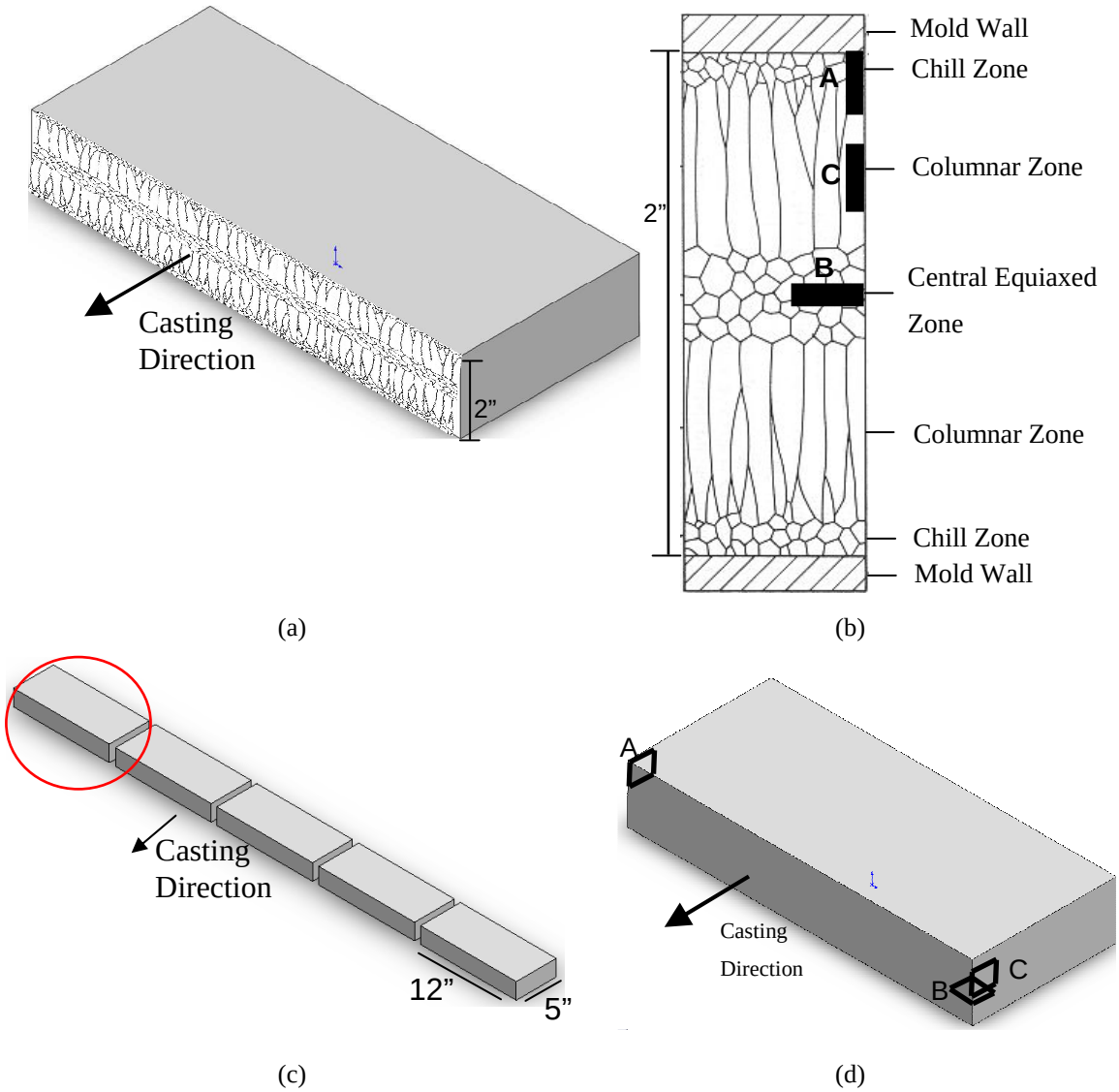

Figure 3.8 Schematic of solidification regions and sample orientations within continuous cast slab demonstrating the chill zone, columnar zone, and equiaxed zone, representing (a) the casting direction, (b) associated solidification regions and areas of interest, (c) location of sample collection relative to slab width, and (d) specimen orientation relative to casting direction.

3.5 Transmission Electron Microscopy

Transmission electron microscopy was used to analyze carbon extraction replicas from selected conditions. The high niobium steel was used initially to analyze precipitate

size and distribution because it demonstrated the most variation between solidification regions and process locations. Additionally, the low niobium steel was examined to compare the range of niobium precipitation behavior between the low and high niobium steels. These behaviors are presented in Section 4.2

Each sample was ground through 120, 240, 400, and 600 grit (water cooled) SiC paper. After grinding, the samples were polished using a 6 μm diamond grit solution and finally a 1 μm grit solution. Carbon extraction replicas were produced by first etching the polished specimen with 2 pct. nital. Carbon was deposited subsequent to etching and the film was scored. Films were floated using an aqueous solution of 3.3 pct. nitric acid, 3.3 pct. acetic acid, and 0.1 pct. hydrofluoric acid and placed on a copper grid [18]. A FEI CM200 transmission electron microscope was used to analyze the size, morphology, and distribution of microalloy precipitates. X-ray spectroscopy was conducted using a Philips CM 12 operating at 120 kV equipped with an EDAX energy dispersive spectroscopy system (PGT-EDS). At least 10 precipitates were measured for chemical analysis for each processing condition and solidification region.

CHAPTER 4 : EXPERIMENTAL RESULTS AND DISCUSSION

4.1 Reproducibility Testing

The preliminary electrochemical extraction experiments with the vanadium containing steel, although very helpful in validating the suitability of the quenching method used in sample collection (Section 3.3), were conducted with single replicates. Additional testing was therefore conducted to assess reproducibility of the test procedures for the niobium alloys that represent the bulk of this program. The reproducibility tests were carried out using the medium niobium CMn(Nb) steel sampled prior to the rolling mill. A total of ten replicates were measured to test reproducibility and effectiveness of the electrochemical extraction and ICP-AES procedures, using both of the DC power supplies, as mentioned previously in Section 3.1.2.

The ten samples were taken from the columnar region, sample location C in Figure 4.1, for its likelihood to exhibit smaller concentration gradients than the surface or centerline regions, and because it represents most of the volume of the as-cast slab. Each sample was prepared according to the method discussed in detail in Section 3.1. After electrochemical extraction and filtration, ICP-AES was conducted on both solutions: the dissolved steel matrix, and the dissolved precipitate solution. Concentrations from ICP-AES were converted to the amount of niobium (in wt. pct.) to determine the extent of alloy in precipitate form, in solution, and total alloy detected. Additionally, the data were converted into relative percentage of alloy precipitated for each alloy, process location, and solidification region. The concentrations were converted from ICP-AES to amount of alloy in weight percent, and percent of alloy detected, using Equations 3.1, 3.2, and 3.3 (discussed in Section 3.2). Conversion from concentration to weight percent is helpful in order to compare the ICP-AES results to the composition reported by the steel producer.

The ten replicates results are shown in Table 4.1. The mean niobium amount (in wt. pct.) of the ten replicates was calculated using Equation 4.1 [7]:

$$\bar{y} = \frac{\sum_{i=1}^{n} y_i}{n} \tag{4.1}$$

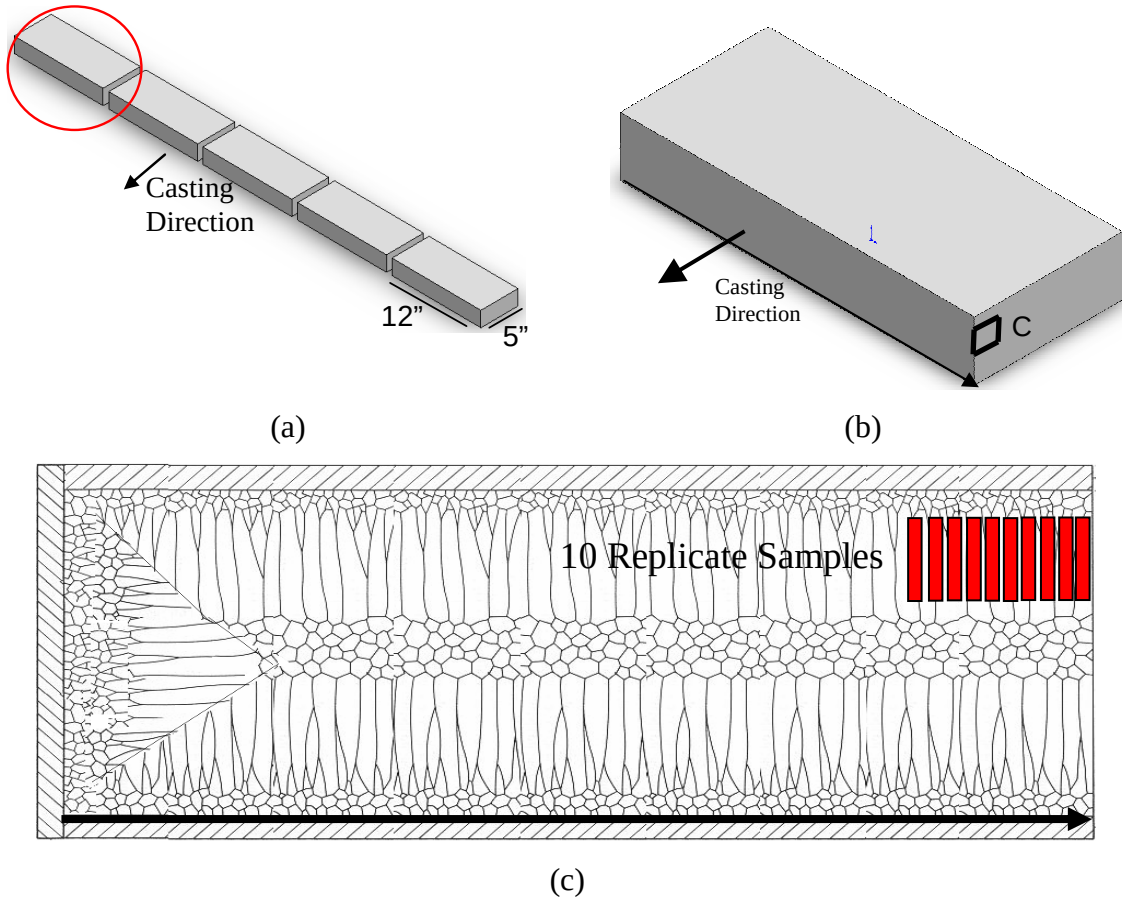

Figure 4.1 The circled section (a) was used to obtain the columnar (b) specimens used during reproducibility testing. (c) Ten replicates were examined for reproducibility testing.

where $\bar{y}$ is the mean niobium content, y_i represents a specific observation, and n is the total number of observations. After finding the sample mean, the standard deviation was found by taking the square root of the sample variance. The sample variance, s^2, was determined by Equation 4.2 [7]:

$$s^2 = \frac{\sum_{i=1}^{n} (y_i - \bar{y})^2}{n-1} \tag{4.2}$$

Therefore, the standard deviation, s, is represented by Equation 4.3 [7]:

$$s = \sqrt{\frac{\sum_{i=1}^{n}(y_i - \bar{y})^2}{n-1}} \tag{4.3}$$

The amount of niobium that precipitated was consistent within the set of ten samples at an average of 0.004 wt. pct. Nb, with a standard deviation of 0.001 wt. pct., which indicates good reproducibility. A 95pct. confidence interval was calculated using the mean niobium content, standard deviation, and total number of observations, as expressed in Equation 4.4 [7]:

$$\bar{y} \pm z_{\alpha/2}\frac{s}{\sqrt{n}} \tag{4.4}$$

where $Z_{\alpha/2}$ equals 1.960. The 95pct. confidence interval for the amount of niobium precipitated is 0.004 ± 0.0005 wt. pct. Nb. Table 4.1 also reports that the average amount of niobium in solution is 88 percent, and the average in precipitated form is 12 percent. In addition, Table 4.2 highlights the similarity of the ICP-AES results compared to the alloy content reported by the steel producer. This nominal percentage difference

Table 4.1 Reproducibility of Niobium Measured in Solution and Precipitate Form

Sample	Precipitate (wt% Nb)	Solution (wt% Nb)	Total (wt% Nb)	Percentage of Nb precipitated	Percentage of Nb in solution
1	0.004	0.025	0.029	13	87
2	0.005	0.025	0.030	15	85
3	0.003	0.027	0.031	11	89
4	0.003	0.028	0.031	11	89
5	0.005	0.026	0.031	17	83
6	0.003	0.026	0.030	12	88
7	0.003	0.025	0.028	10	90
8	0.003	0.026	0.030	11	89
9	0.003	0.026	0.029	10	90
10	0.004	0.026	0.029	12	88
95% Confidence Interval	0.004 ± 0.001	0.026 ± 0.001	0.030 ± 0.001	12 ± 1	88 ± 1

(Equation 3.3) indicated that the procedure is reproducible and results from the ICP-AES analysis are comparable to the alloy content reported by the steel producer. The results also indicated that the columnar region for the medium CMn(Nb) steel prior to hot rolling

demonstrated minimal alloy segregation on a macroscopic scale. Overall, it was concluded that the reproducibility of the testing method was sufficient.

Table 4.2 Accuracy of ICP Analysis and Reported Alloy Content Using Medium CMn(Nb) for Reproducibility Testing

Sample	Total (wt% Nb)	Reported Alloy Content (wt% Nb)	Precentage Difference
1	0.029	0.030	-3
2	0.030	0.030	-2
3	0.031	0.030	3
4	0.031	0.030	3
5	0.031	0.030	3
6	0.030	0.030	-1
7	0.028	0.030	-6
8	0.030	0.030	-1
9	0.029	0.030	-2
10	0.029	0.030	-2

4.2 Influence of Niobium Content and Slab Location on Precipitation Behavior

The results concerning microalloy precipitation behaviors are discussed relative to varying niobium additions and solidification regions (i.e. slab locations) prior to hot-rolling.

4.2.1 Slab Surface Region

The slab location and specimen orientation for the edge/slab surface region are illustrated in Figure 4.2(a), and Figure 4.2(b), respectively, as sample location A. Sample location A was chosen near the slab corner to observe the extent of microalloy precipitation on the edges of the slab, where the lowest slab temperatures are experienced. Specimens were taken at both process locations (i.e. base of the caster and prior to hot rolling) for the low, medium, and high niobium steels. Ten replicate specimens were prepared for each of the alloys at each process location. The average of the ten measurements was taken to represent the microalloy precipitation behavior at the edges of the slab.

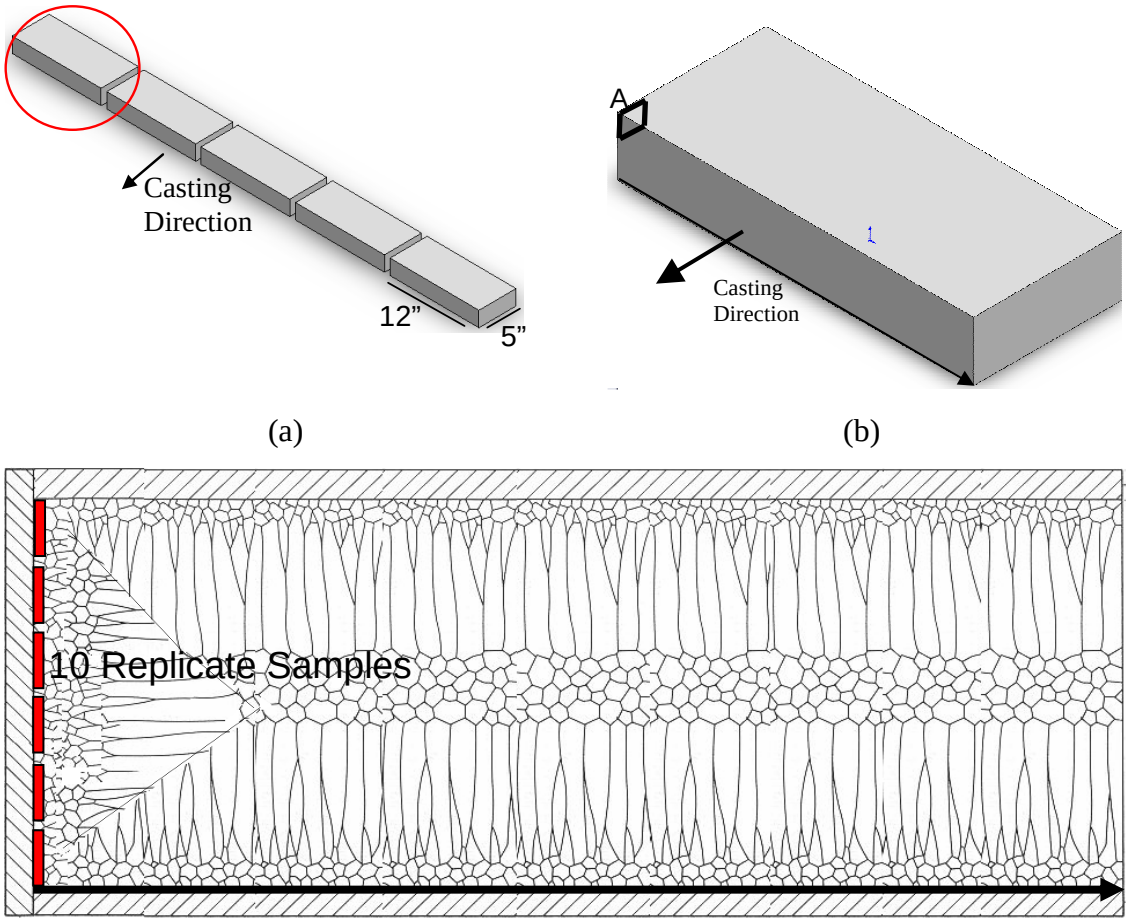

Figure 4.2 The circled section (a) was used to obtain the slab surface (b) specimens used for the examination of the precipitation behavior concerning the influence of niobium content and slab location. (c) A total of ten replicates were prepared for each condition along the slab edge.

The results from the edge location at both process locations are summarized in Tables 4.3 and 4.4. The average of the ten measurements (for each processing location) is shown in Figure 4.3 as the absolute amount of niobium precipitated (in wt. pct.) plotted against niobium content. Additionally, Figure 4.4 is a representation of the relative amount of niobium precipitated (pct. Nb) plotted against the amount of alloy given by the steel producer. Uncertainty analysis is represented by one standard deviation (Equation 4.3) [72]. The standard deviation was chosen to demonstrate the variation seen between the ten replicate samples for each steel grade and process location. Uncertainty analysis of niobium precipitated (in wt. pct.), using the 95pct. confidence interval (Equation 4.4) about the mean for the edge location, is shown in Figure A1. Table A2

presents the uncertainty analysis results for the edge location for each process location related to standard deviation and 95pct. confidence interval. The standard deviation was specifically chosen to demonstrate sample variation (rather than the 95pct. confidence interval) because a normal distribution was not assumed [72].

Table 4.3 Average Niobium Measured in Solution and Precipitate Form Edge Location at the *Base of the Caster*

Sample	Precipitate (wt% Nb)	Solution (wt% Nb)	Total (wt% Nb)	Percentage of Nb precipitated	Percentage of Nb in solution	Producer's Reported Alloy Content (wt% Nb)	Precentage Difference
Low Nb Caster	0.003	0.011	0.014	24	76	0.014	2
Med Nb Caster	0.008	0.022	0.030	28	72	0.030	-1
High Nb Caster	0.026	0.029	0.056	48	52	0.046	22

Table 4.4 Average Niobium Measured in Solution and Precipitate Form Edge Location *Prior to Hot Rolling*

Sample	Precipitate (wt% Nb)	Solution (wt% Nb)	Total (wt% Nb)	Percentage of Nb precipitated	Percentage of Nb in solution	Producer's Reported Alloy Content (wt% Nb)	Precentage Difference
Low Nb Furnace Exit	0.005	0.007	0.011	45	55	0.014	-17
Med Nb Furnace Exit	0.010	0.023	0.033	31	69	0.030	11
High Nb Furnace Exit	0.018	0.027	0.045	36	64	0.046	-3

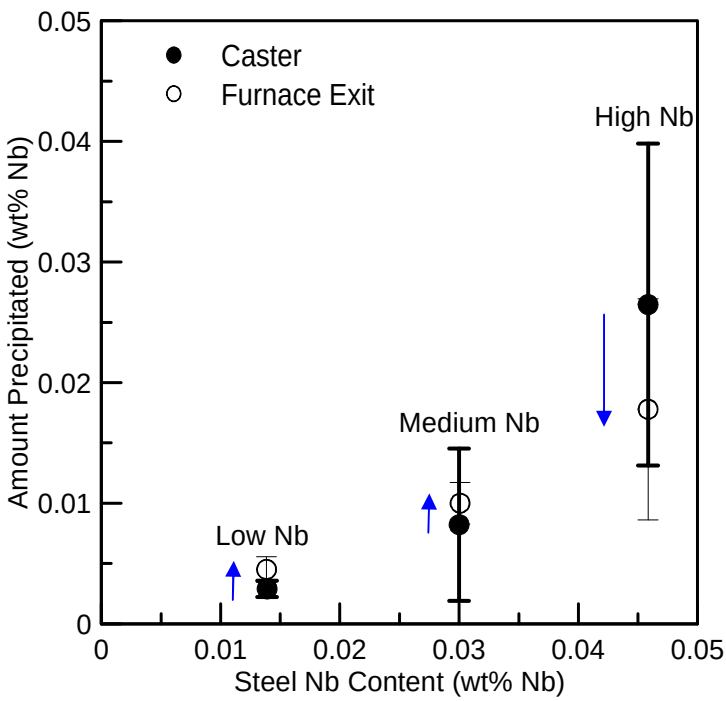

Figure 4.3 Slab surface/edge location; average niobium in precipitate form measured by ICP-AES in wt. pct. from ten replicates plotted against the reported alloy content measured by the steel producer.

The low and medium niobium steels appeared to exhibit some precipitation during equalization in the furnace prior to hot rolling. In Figure 4.3, the arrow in the "up" direction indicates that alloy precipitation was observed (through the tunnel furnace). In contrast, the high niobium steel exhibited the largest amount of precipitation (relative to niobium content) immediately after casting, followed by niobium dissolution during equalization through the tunnel furnace. Niobium dissolution (through the tunnel furnace) is represented by the "down" arrow.

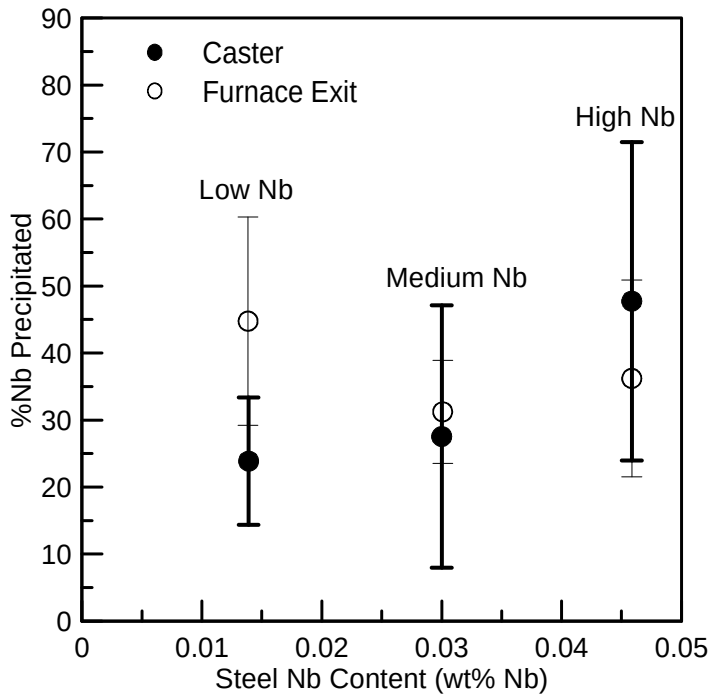

Figure 4.4 Slab surface/edge location; average niobium in precipitate form measured by ICP-AES in pct. of niobium precipitated from ten replicates plotted against the reported alloy content measured by the steel producer.

4.2.2 Columnar Region

The slab surface location and sample orientation for the columnar region are shown in Figure 4.5(a) and Figure 4.5(b), respectively, as sample location C. Specimens were taken from both process locations for the low, medium, and high niobium steels. Five replicate specimens were prepared for each of the alloys at each process location and solidification region. The columnar region presumably represented the behavior of most of the slab volume. The number of samples was reduced from that of the slab surface

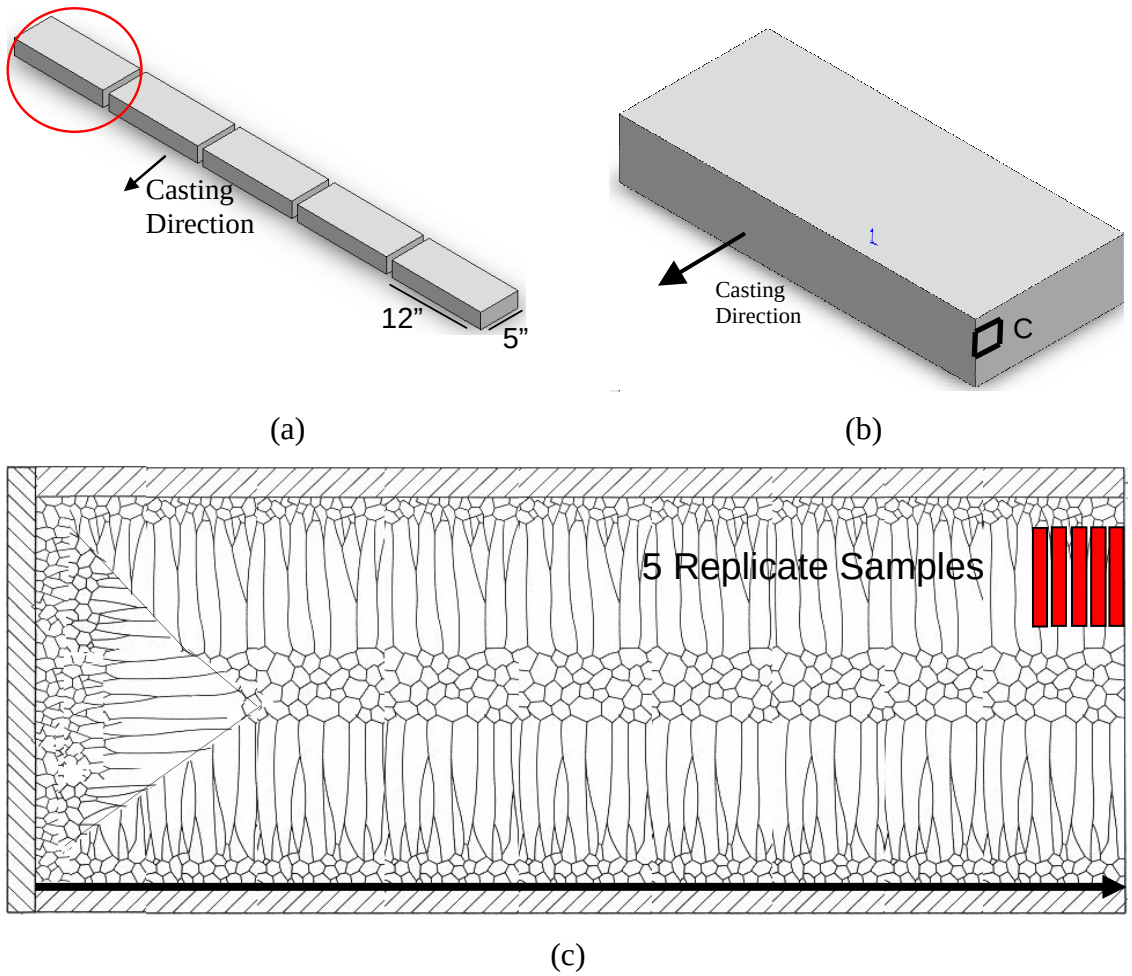

Figure 4.5 The circled section (a) was used to obtain the columnar region (b) specimens used for the examination of the precipitation behavior concerning the influence of niobium content and slab location. (c) A total of five replicates were prepared for each condition within the columnar region.

(Section 4.2.1) on the basis of the good repeatability of results from reproducibility testing, reported in Section 4.1. The average results from the columnar region for both process locations are summarized in Tables 4.5 and 4.6. Figure 4.6 presents the absolute amount of niobium precipitated (in wt. pct. Nb), and Figure 4.7 provides a graphical representation of the relative amount of niobium precipitated (pct. Nb), plotted against the amount of niobium given by the steel producer. The uncertainty analysis is shown by one standard deviation (Equation 4.3) about the mean to demonstrate the variation observed between replicates. Additional graphical representation demonstrating the 95pct. confidence interval (Equation 4.4) about the mean (for the columnar region) can

be observed in Figure A2. An uncertainty analysis for both process locations is presented in Table A2.

Table 4.5 Average Niobium Measured in Solution and Precipitate Form Columnar Location at the *Base of the Caster*

Sample	Precipitate (wt% Nb)	Solution (wt% Nb)	Total (wt% Nb)	Percentage of Nb precipitated	Percentage of Nb in solution	Producer's Reported Alloy Content (wt% Nb)	Precentage Difference
Low Nb Caster	0.003	0.010	0.013	24	76	0.014	-7
Med Nb Caster	0.004	0.027	0.031	14	86	0.030	3
High Nb Caster	0.005	0.045	0.050	10	90	0.046	9

Table 4.6 Average Niobium Measured in Solution and Precipitate Form Columnar Location *Prior to Hot Rolling*

Sample	Precipitate (wt% Nb)	Solution (wt% Nb)	Total (wt% Nb)	Percentage of Nb precipitated	Percentage of Nb in solution	Producer's Reported Alloy Content (wt% Nb)	Precentage Difference
Low Nb Furnace Exit	0.002	0.009	0.012	21	79	0.014	-16
Med Nb Furnace Exit	0.003	0.026	0.030	11	89	0.030	-1
High Nb Furnace Exit	0.007	0.047	0.054	14	86	0.046	18

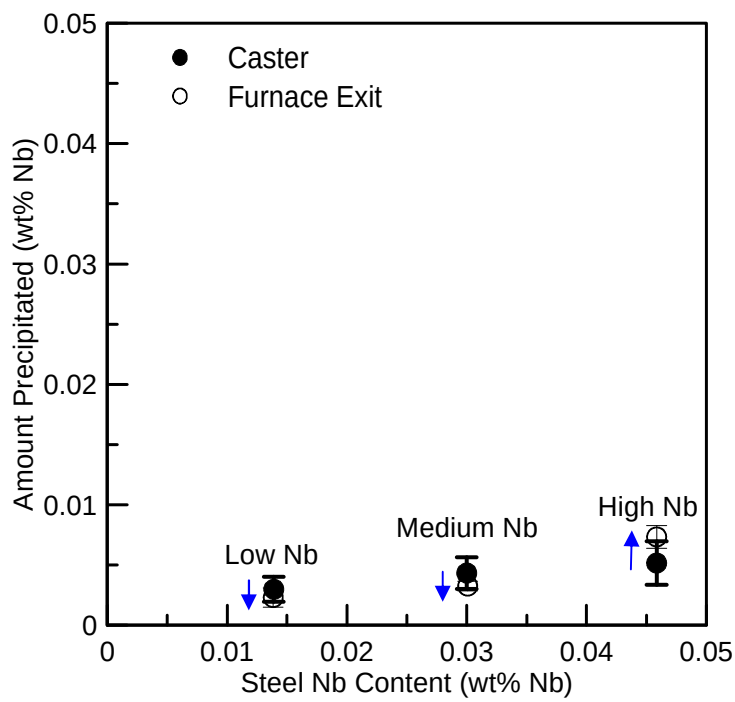

Figure 4.6 Columnar location; average niobium in precipitate form measured by ICP-AES in wt. pct. from five replicates plotted against the reported alloy content measured by the steel producer.

For the columnar region, it was observed that the absolute amount of niobium in precipitated form was greatest in the high niobium steel, while the relative amount was greatest in the low niobium steel. Substantial changes (i.e. precipitation or dissolution) during equalization in the tunnel furnace for the low and medium niobium steels were not apparent; some precipitation was indicated for the high niobium steel. It was also observed that the variability between the samples from the columnar region was generally less than the variability observed in the edge samples, based on a comparison of standard deviations, and 95 pct. confidence intervals.

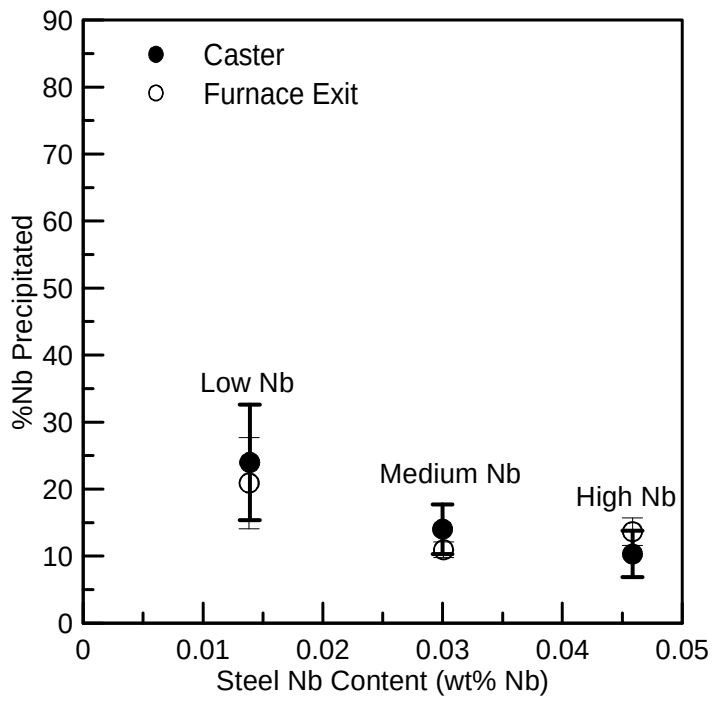

Figure 4.7 Columnar location; average niobium in precipitate form measured by ICP-AES in pct. of niobium precipitated from five replicates plotted against the reported alloy content measured by the steel producer.

4.2.3 Centerline Region

The slab location and specimen orientation in the centerline region is depicted in Figure 4.8(a) and Figure 4.8(b), respectively, as sample location B. Specimens (13 x 13 x 13 mm coupons) were taken from both process locations for the low, medium, and high niobium steels. Five replicate specimens were prepared for each of the alloys at each process location. The average results from the centerline sampling region for the base of

the caster and prior to the rolling mill are summarized in Tables 4.7 and 4.8, and graphically in Figures 4.9 and Figure 4.10, respectively. The uncertainty analysis is shown as one standard deviation (Equation 4.3) about the mean. An uncertainty analysis using the 95pct. confidence interval (Equation 4.4) about the mean is shown in Figure A3. An uncertainty analysis results for the centerline region at both process locations are presented in Table A3, related to standard deviation and 95 pct. confidence interval.

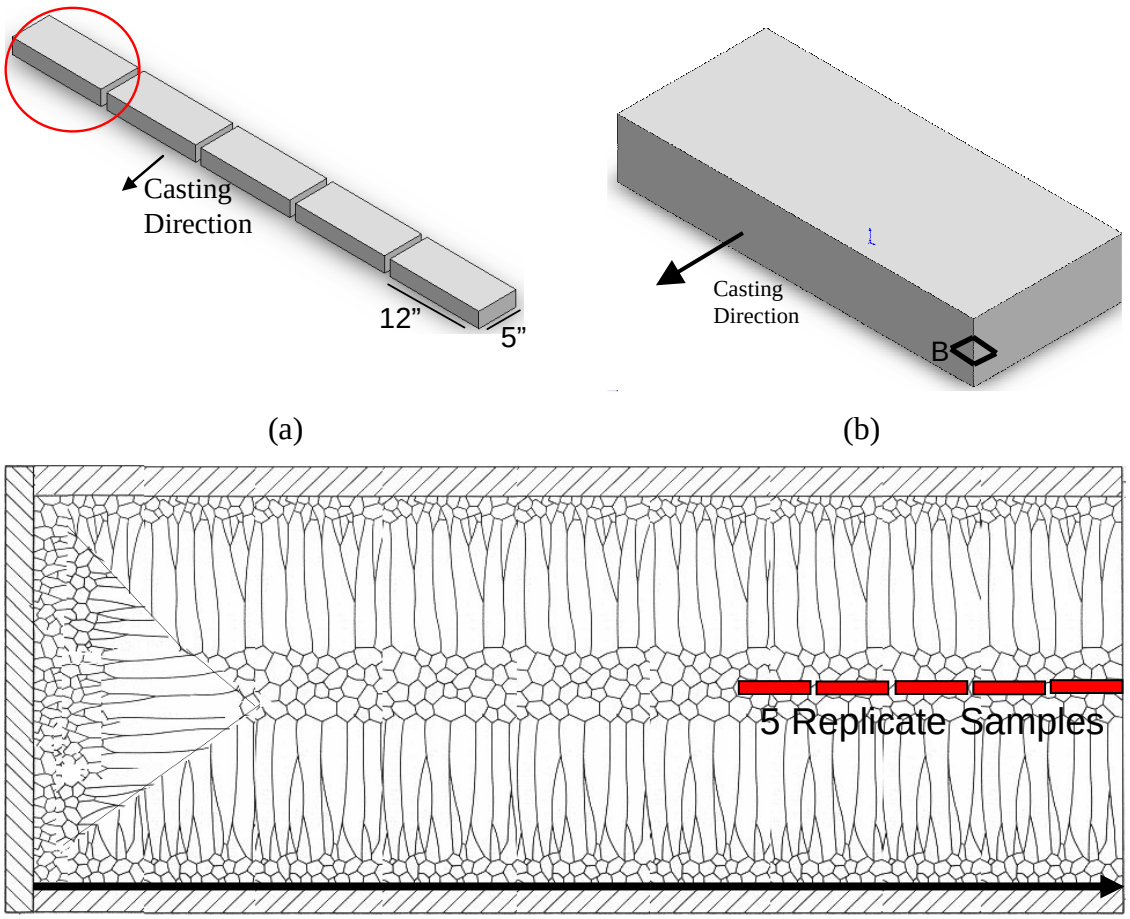

(a) (b)

(c)

Figure 4.8 The circled section (a) was used to obtain the columnar region (b) specimens used for the examination of the precipitation behavior concerning the influence of niobium content and slab location. (c) A total of five replicates were prepared for each condition within the centerline region.

Table 4.7 Average Niobium Measured in Solution and Precipitate Form Centerline Region at the *Base of the Caster*

Sample	Precipitate (wt% Nb)	Solution (wt% Nb)	Total (wt% Nb)	Percentage of Nb precipitated	Percentage of Nb in solution	Producer's Reported Alloy Content (wt% Nb)	Precentage Difference
Low Nb Caster	0.004	0.007	0.011	40	60	0.014	-23
Med Nb Caster	0.005	0.025	0.031	17	83	0.030	2
High Nb Caster	0.009	0.044	0.053	17	83	0.046	15

Table 4.8 Average Niobium Measured in Solution and Precipitate Form Centerline Region *Prior to Hot Rolling*

Sample	Precipitate (wt% Nb)	Solution (wt% Nb)	Total (wt% Nb)	Percentage of Nb precipitated	Percentage of Nb in solution	Producer's Reported Alloy Content (wt% Nb)	Precentage Difference
Low Nb Furnace Exit	0.005	0.006	0.011	50	50	0.014	-24
Med Nb Furnace Exit	0.006	0.028	0.033	17	83	0.030	11
High Nb Furnace Exit	0.015	0.040	0.055	27	73	0.046	19

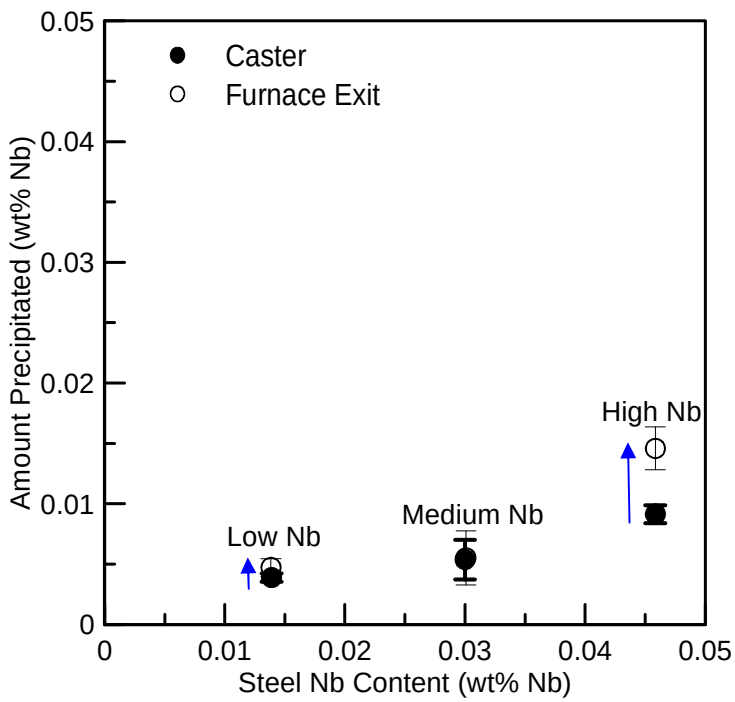

Figure 4.9 Centerline location; average niobium in precipitate form measured by ICP-AES in wt. pct. from five replicates plotted against the reported alloy content measured by the steel producer.

The results obtained from the centerline region indicated that the absolute amount of niobium precipitated was greatest in the high niobium steel, while the relative amount was greatest in the low niobium steel. Substantial changes (i.e. precipitation or dissolution) during equalization in the tunnel furnace for the low and medium niobium

steels were not apparent; some precipitation was observed in the high niobium steel. It was also observed that the variability in the centerline region (demonstrated by the standard deviation about the mean) was similar to the columnar region, but less than the variability observed at the edge location.

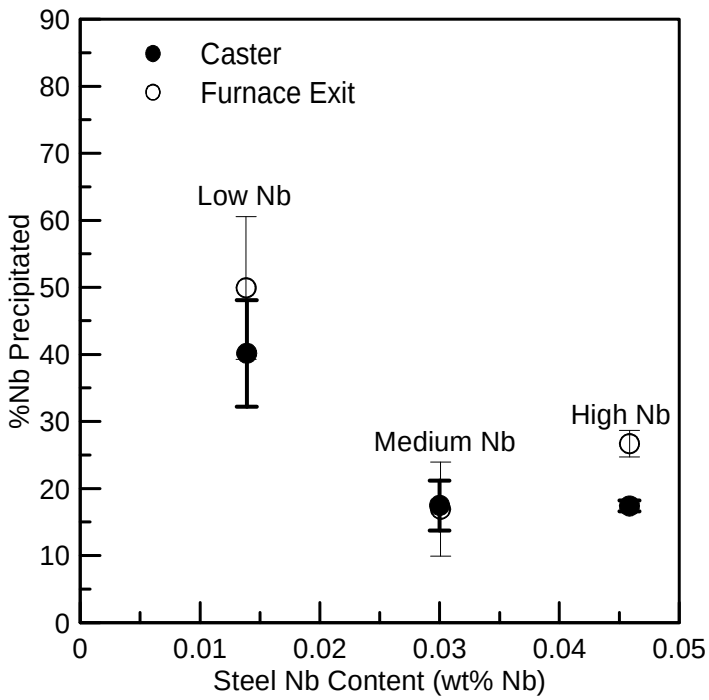

Figure 4.10 Centerline location; average niobium in precipitate form measured by ICP-AES in pct. of niobium precipitated from five replicates plotted against the reported alloy content measured by the steel producer.

4.2.4 Discussion – Electrochemical Analysis

The average results from the analysis for both process locations and sampling locations within the slab are combined in Figure 4.11 for comparison. The amount of niobium precipitated (in wt. pct.) is plotted against the through thickness position (i.e. slab surface/edge, columnar, and centerline). The results reveal that the greatest amount of alloy precipitation occurred at the edges/corners of the continuously cast slab. The measured amount of precipitation was greatest in the high niobium steel in the edge location at the base of the caster. Dissolution subsequently occurred during reheating and equalization in the tunnel furnace in the slab surface/edge of the high niobium alloy. The columnar region represented the bulk of the slab volume, and exhibited the lowest

amount of precipitated niobium in each condition. The high percentage of niobium precipitation along the slab edges can be understood in terms of the slab surface temperature and solubility of niobium carbonitrides. The lower temperature of the slab surface at the base of the caster was associated with an increasing driving force for alloy precipitation, and therefore conducive to precipitation in the surface/edge/corner regions. Increasing the niobium content possibly increased the supersaturation and allowed more niobium precipitation to occur at higher temperatures.

The electrochemical results suggest that some niobium dissolution for the high niobium alloy occurred during processing through the tunnel furnace on the corners of the slab. The soaking time and temperature within the tunnel furnace equalized the temperature profile of the slab, increasing niobium solubility in the cooler regions of the casting (i.e. at the surface). This effect was beneficial because the re-dissolved niobium in the austenite was available to enhance the thermomechanical processing response and final properties necessary for austenite conditioning as discussed previously in Section 2.3. An increased amount of niobium was also observed to precipitate within the centerline region (relative to the columnar region), presumably caused by the alloy-rich liquid present during the final stage of solidification. The medium niobium alloy also demonstrated higher precipitation along the slab surface with less precipitation within the columnar and centerline regions. This alloy showed little difference in the amount of alloy precipitated between the results from the base of the caster and prior to hot rolling. In the low niobium steel, it appears that slight niobium precipitation occurred during equalization in the tunnel furnace in the corners of the cast slab. Niobium precipitation in the columnar and centerline regions did not demonstrate notable changes (i.e. precipitation or dissolution) through the tunnel furnace. The low niobium steel demonstrated the least amount of absolute precipitation in comparison to the medium and high niobium alloys.

Consideration of (macro) alloy segregation was based on the total amount of niobium detected by ICP-AES for the varying solidification regions. From an examination of the results in Tables 4.3-4.8, it was concluded that no substantial or systematic changes (i.e. alloy rich or alloy depleted regions) were observed between the slab surface/edge, columnar, and centerline locations for the slabs evaluated in this work.

A theoretical temperature profile (provided by collaborators) was calculated based on processing parameters, alloy content, and secondary cooling within the Nucor Steel - Hickman casting facility [16]. Figure 4.12 shows the thermal profile of the slab and the corresponding "predicted" temperatures for the slab surface/edge, middle (columnar), and centerline regions as the slab travels from the base of the mold (meniscus) and through the tunnel furnace. The predicted thermal profile indicated that the slab surface experienced some reheating through the tunnel furnace, while the columnar and centerline regions experienced cooling. Temperature equalization occurs early in the tunnel furnace.

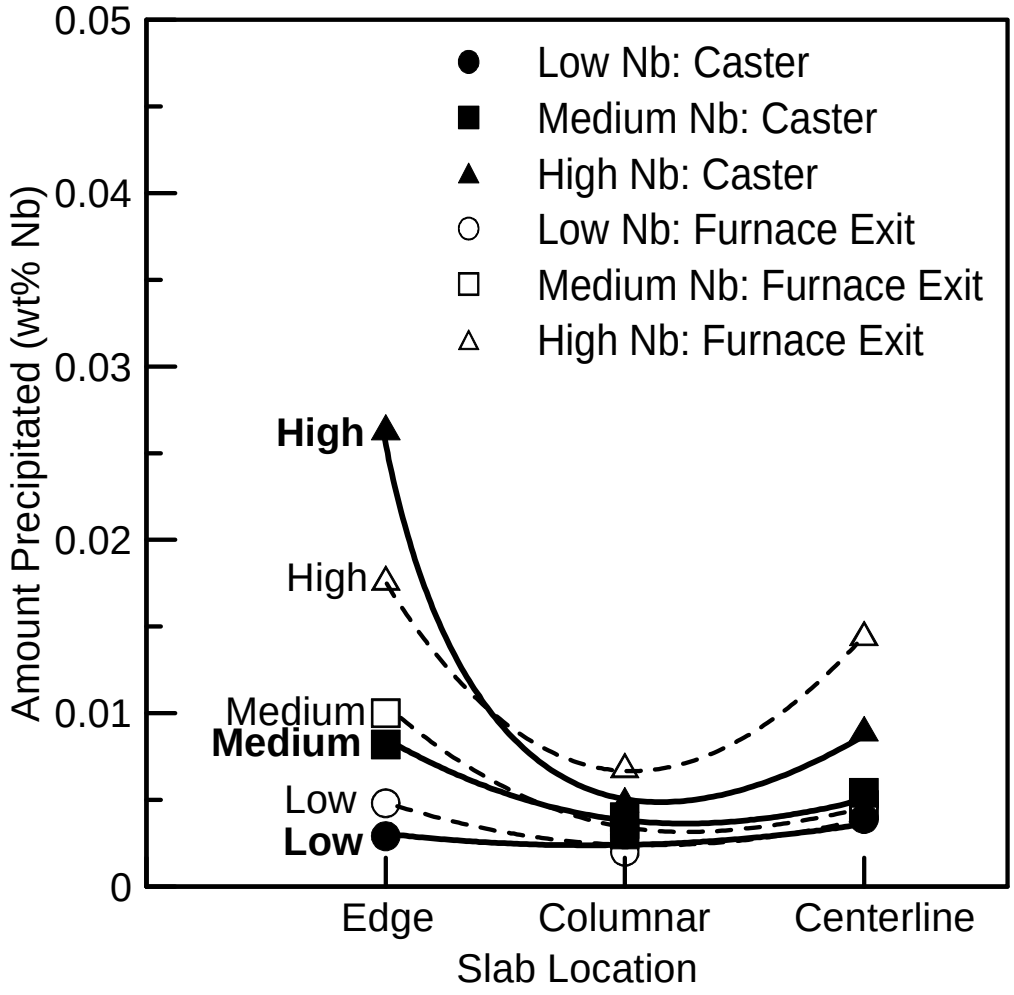

Figure 4.11 Niobium in precipitate form measured by ICP-AES (in wt. pct.) plotted against the sample location through the thickness of the slab.

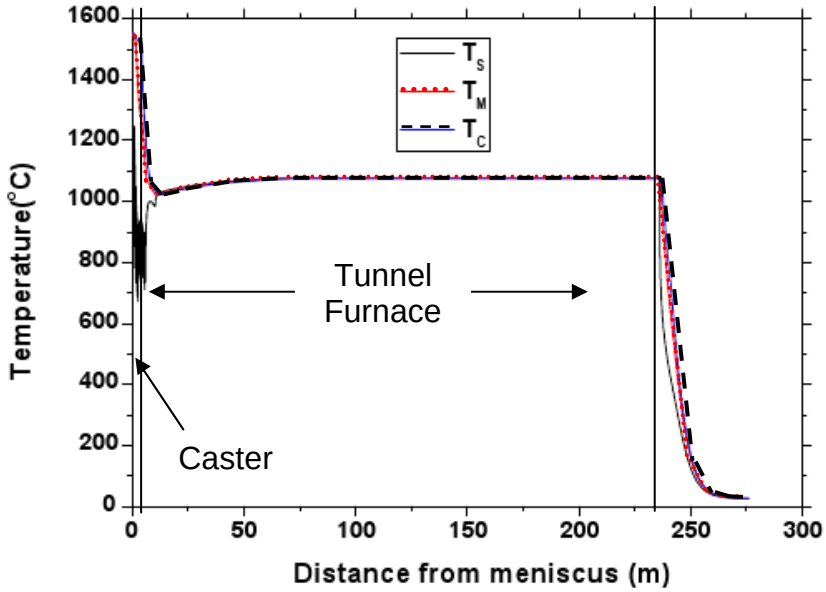

(a)

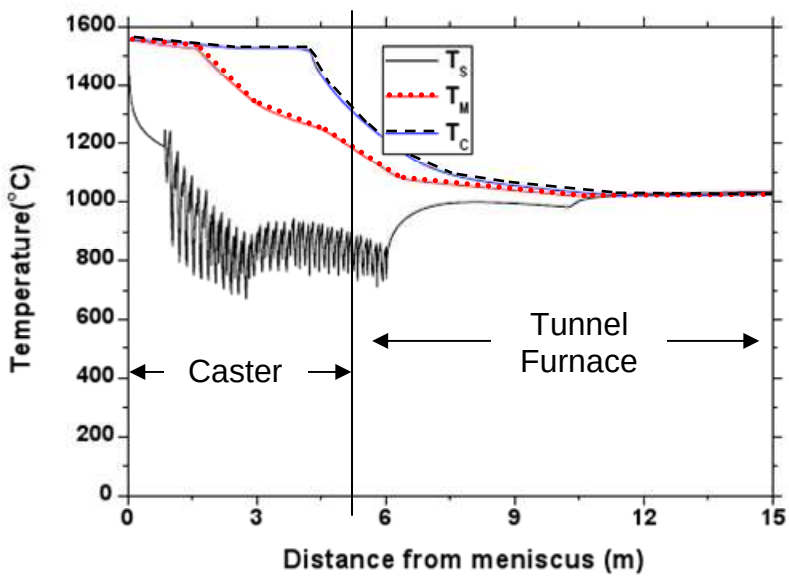

(b)

Figure 4.12 Based on processing parameters, alloy content, and secondary cooling of the Nucor Steel - Hickman casting facility; (a) temperature profile of continuous cast slab predicted from the base of the mold through the tunnel furnace, and (b) the temperature differences experienced at the base of the caster and entry into the tunnel furnace.

A quantitative analysis of the results compared to the calculated solubility relations (Figure 3.12) is shown in Figure 4.13. The reported slab surface temperature

observed at each process location and results for the associated solidification region are superimposed over the solubility relationships. Figure 4.13 shows that the amount of niobium precipitation (in wt. pct.) at the base of the caster was lower than that of the predicted niobium precipitation calculated [16] for each alloy and solidification region, even for the edge location where the actual temperatures may have approached the indicated values. However, niobium precipitation prior to hot rolling followed the

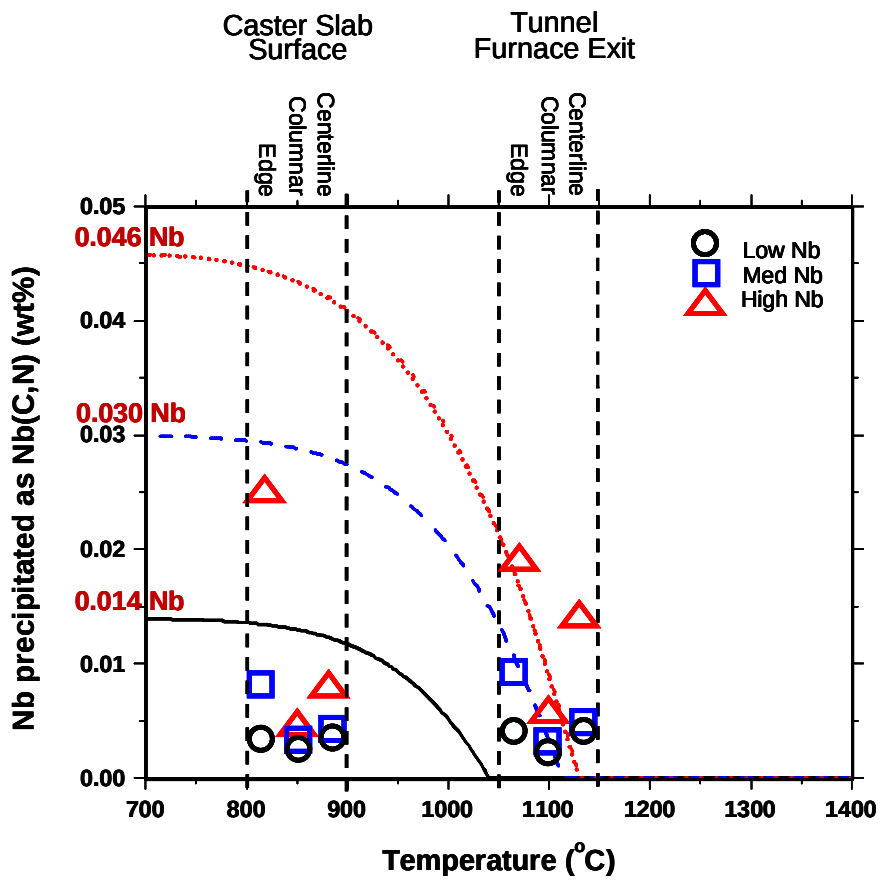

Figure 4.13 Calculated wt. pct. Nb precipitated as a function of temperature for low, medium, and high niobium additions [16], also showing approximate ranges of slab temperature and quantitative comparison between combined chemical results. The locations of the edge/columnar/centerline results do not reflect actual relationships.

expected trend for these alloys, although the low niobium steel prior to hot rolling did demonstrate some niobium precipitation, while the calculation estimated that all niobium should remain in solution. The role of segregation could be important in understanding deviations between calculations and measured values, although the segregation effects

have not been studied here in detail. The actual temperatures experienced by the columnar and centerline regions were unknown and were undoubtedly higher than the reported slab surface temperature.

4.3 Precipitate Characterization

TEM verification of the precipitation behavior observed during electrochemical analysis was completed. Selected alloys, process locations, and solidification regions chosen for this study are shown in Figure 4.14. The data presented in bold in Figure 4.14 represent the samples selected for TEM analysis. The samples include: high niobium steel at both process locations for the edge, columnar, and centerline regions, the low niobium steel prior to hot rolling for the edge, columnar, and centerline regions, and the low niobium steel at the base of the caster for the edge location. For this study, five carbon extraction replicas were made for each specimen, and analyses of at least three replicas were completed to ensure a general observation was made for each alloy, process location, and solidification region. The high niobium alloy was chosen because it demonstrated the highest amount of niobium precipitation, and the most substantial change (i.e. precipitation and dissolution) between process locations and solidification regions. The low niobium alloy was chosen because it demonstrated the least amount of niobium precipitation at each process location and solidification region. The medium niobium alloy was omitted because the results from the electrochemical analysis fell within the range of the high and low niobium alloys for each process location and solidification region. The columnar and centerline regions for the low niobium steel at the base of the caster were also omitted because niobium precipitation was similar to that observed prior to hot rolling. Because niobium precipitation behavior prior to hot rolling was the focus of this program, each solidification region at the furnace exit was examined in the low niobium alloy.

Precipitate size was found by measuring the length and width of each particle using an arbitrary line measurement function available in conjunction with the imaging process. Figure 4.15 presents a TEM bright field image showing microalloy precipitation in the as-cast slab, and associated particle measurements. The cross-sectional area of the precipitate was used to calculate the “equivalent diameter” of each particle.

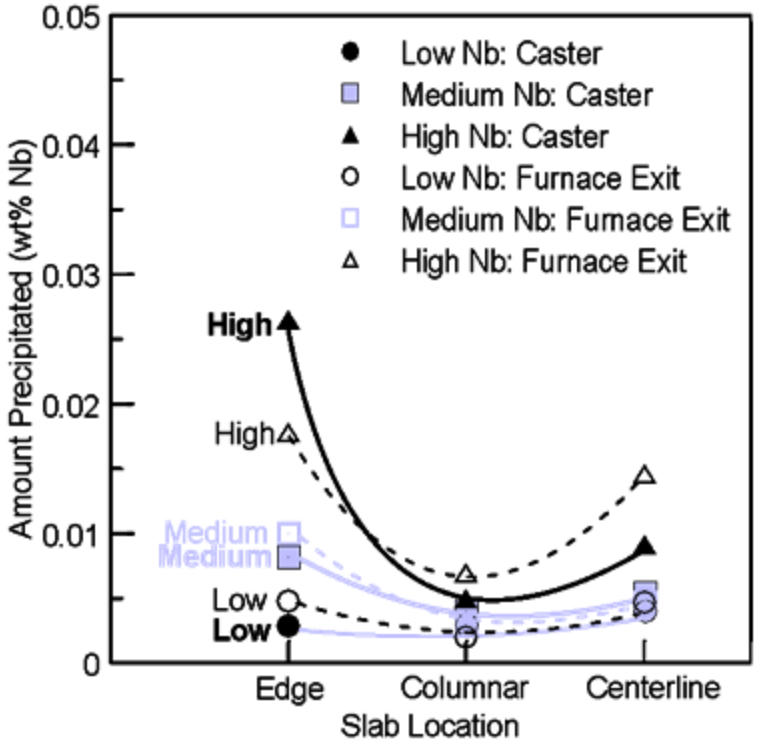

Figure 4.14 Selected Nb alloys presented in bold represent the sample locations chosen for TEM analysis and verification of the electrochemical extraction results. .

Approximately 200 particles were counted from ten fields of view over at least three different replicas (per condition), to obtain particle size distributions for the selected alloys. At least ten precipitates were analyzed using EDS analysis for each processing condition and solidification region. Some larger titanium-rich particles were observed during TEM analysis. However, the large titanium based particles were not included in the particle size distribution analysis, or the precipitate volume fraction calculations [67,68]. A TEM bright field image is shown in Figure 4.16(a), and an associated EDS spectrum in Figure 4.16(b), providing a general representation of a large titanium-rich particle observed in the columnar region at the base of the caster. The larger particles were seen primarily in the high niobium steel in both process locations. Although larger titanium-rich particles were observed primarily in the high Nb steel, titanium-containing particles were also observed in each solidification region in the low niobium alloy. It should be noted that each EDS spectrum exhibited a copper peak due to detection of the copper grid used for supporting the carbon extraction replicas.

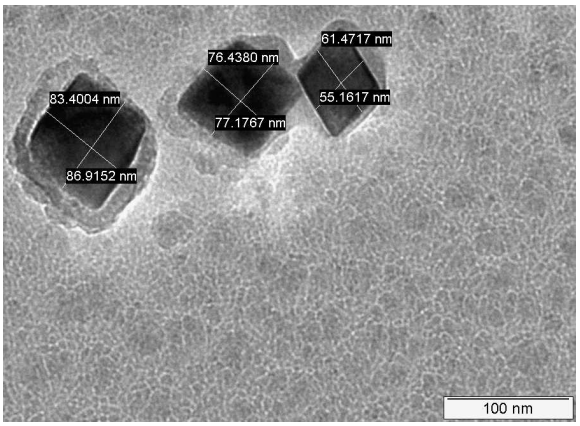

Figure 4.15 TEM bright field image of carbon extraction replica from the columnar region at the base of the caster for the high niobium steel. Equivalent particle diameter found by measuring the length and width of the precipitate and finding the associated cross-sectional area.

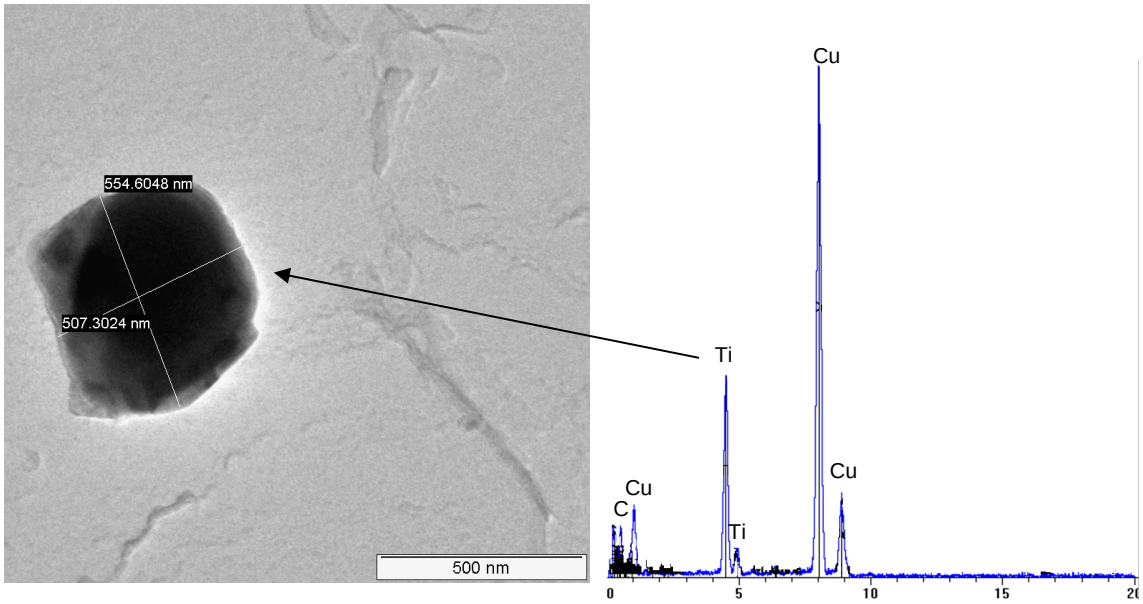

(a) (b)

Figure 4.16 (a) TEM bright field image of Ti-rich particle seen during particle size analysis in the high Nb alloy in the centerline region prior to hot rolling and (b) associated EDS spectrum.

4.3.1 Precipitate Size and Morphology

The selection of specimens from the high and low niobium steels represented the greatest contrast of the precipitation behavior observed during electrochemical analysis as discussed in section 4.2. The high niobium steel demonstrated the greatest amount of

precipitation, and showed the most substantial change (i.e. precipitation and dissolution) among the three solidification regions. The low niobium steel demonstrated the least absolute amount of niobium precipitation, and an inconsequential change between solidification regions and process locations.

Figure 4.17 presents TEM bright field images showing microalloy precipitation which occurred in the slab surface region at both process locations for the high niobium alloy. The average (equivalent) particle diameter was determined based on approximately 200 particles. For each condition, particles were counted from ten fields of view over at least three different replicas.

An example of precipitation at the base of the caster is shown in Figure 4.17(a). The associated EDS analysis is shown in Figure 4.17(b). EDS was obtained with a focused electron beam that was approximately the diameter of the circled area indicated on the micrograph. The niobium peak was determined by the amount of niobium present within the circled area. While the EDS spectrum showed that niobium was present, the relative height of the niobium peak was observed to be smaller due to a small particle size relative to the diameter of the focused electron beam. As seen in Figure 4.17(a), the circled region examined during EDS included several smaller particles for analysis. Thus, the niobium peak was smaller than a peak observed for larger particles that encompassed the full diameter of the focused electron beam.

Morphologies including irregular-cuboidal and cuboidal were present. Niobium precipitation observed in the slab surface at the tunnel furnace exit is shown in Figure 4.17(c). The electrolytic extractions for these conditions are highlighted in Figure 4.17(d). For both process locations, the slab surface region demonstrated a high number density of particles on a single carbon replica. However, there were a higher number of particles present on the replicas prepared for the base of the caster condition. The high number density of Nb-rich particles seen at the base of the caster supports the electrochemical analysis which indicated that precipitation along the slab surface at the base of the caster was greater than prior to hot rolling (in the high niobium steel). Precipitate volume fraction, related to particle number density per area (on a given replica) is discussed in detail later in this chapter (Section 4.3.3).

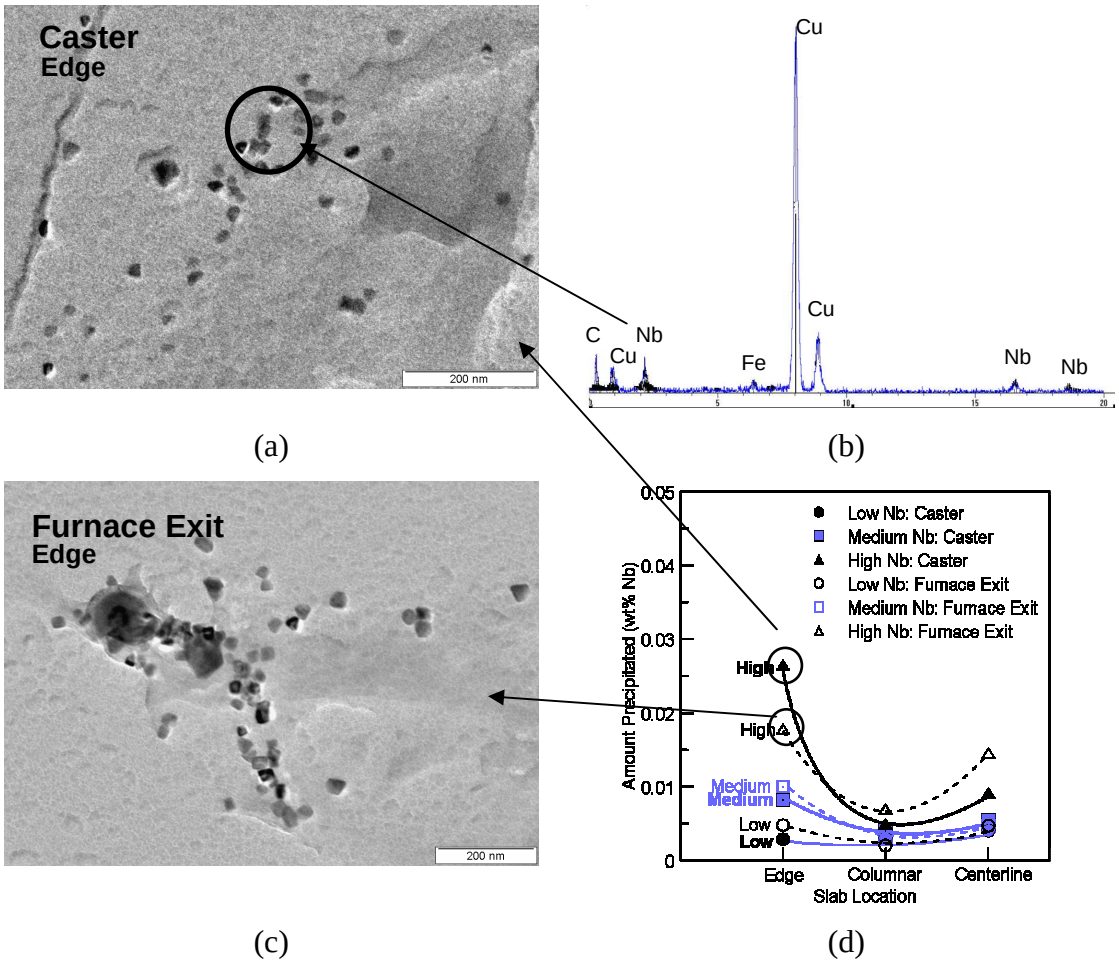

Figure 4.17 TEM analysis of precipitation behavior on the slab edge relative to process location for the high Nb steel. (a) Precipitates at the base of the caster, (b) corresponding EDS analysis, (c) Precipitation at furnace exit, and (d) process and slab location related to micrographs.

Figure 4.18 shows precipitation which occurred within the columnar region for both process locations. Figure 4.18(a) corresponds to precipitation at the base of the caster. Precipitation subsequent the tunnel furnace is shown in Figure 4.18(c). EDS was obtained with a focused electron beam that was approximately the diameter of the circled area indicated on the micrograph. The EDS results suggest that the larger particles observed at each process location also contained a minor portion of titanium, (Figures 4.18(b) and Figure 4.18(d)). The relatively large particle size and size variation prior to hot rolling suggest that some particles, which were present at the base of the caster, appeared to have sufficient time to grow through the tunnel furnace. It is not clear if smaller precipitates present at the base of the caster dissolved through the tunnel

furnace. Both process locations demonstrated a relatively low number density of particles for the columnar region, in comparison to the slab surface. Presumably, this could be because of the absence of a low temperature excursion which would promote more extensive nucleation. The microscopy results are supportive of the electrochemical extraction results which suggest that there was greater alloy precipitation present in the slab surface based on number density of precipitates per replica.

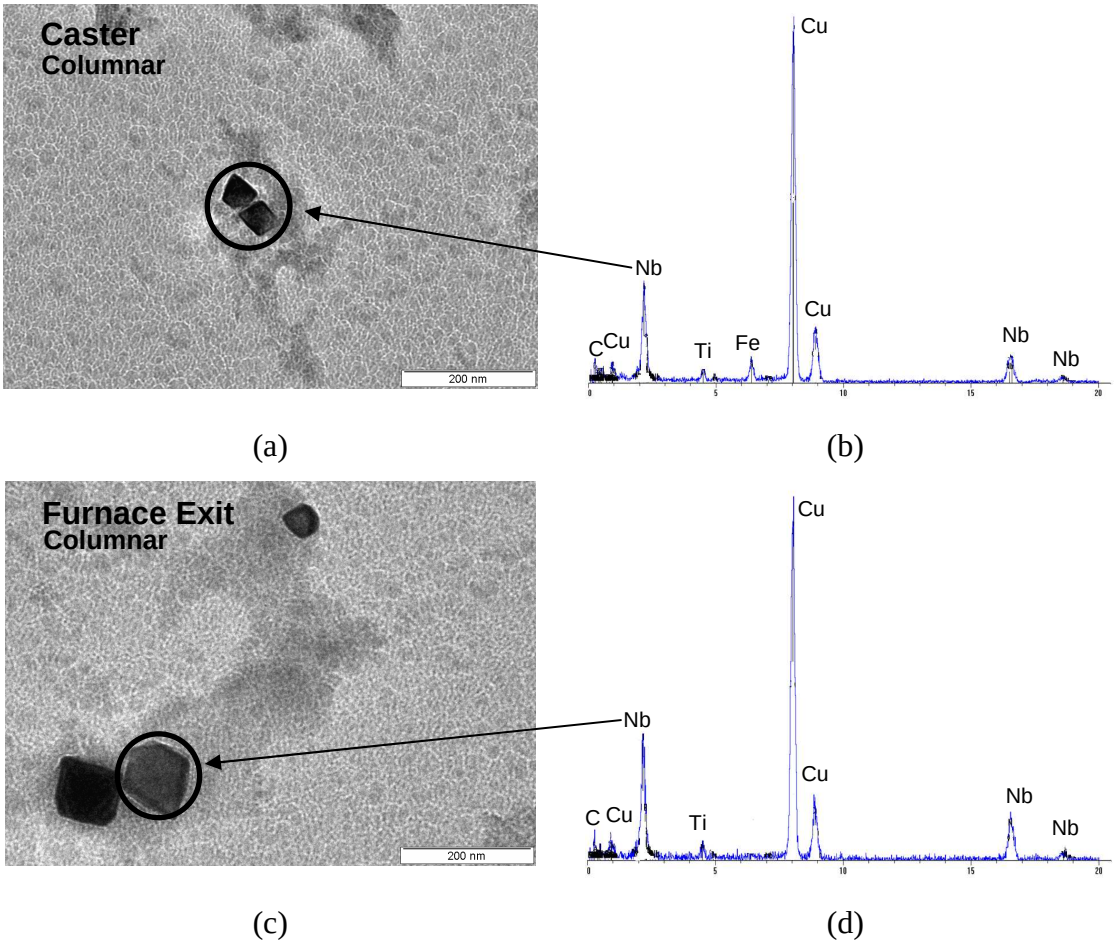

Figure 4.18 TEM analysis of precipitation behavior and corresponding EDS analysis (circled area) in the columnar region relative to process location for the high Nb steel. (a) Precipitates at the base of the caster, (b) corresponding EDS analysis, (c) precipitation at furnace exit, and (d) corresponding EDS analysis.

Figure 4.19 presents an example of precipitation in the centerline region of the as-cast slab. In Figure 4.19(a) and Figure 4.19(c) the precipitates shown are irregular-cuboidal/cuboidal, and the particle size is somewhat larger than observed in the

slab surface/edge and columnar regions. Figure 4.19(c) shows large niobium particles in the centerline region of the as-cast slab at the furnace exit. The particle size distribution demonstrates less variation in the condition prior to hot rolling and a smaller average particle size compared to those observed at the base of the caster. It was observed that the number density of particles in the centerline was greater in the condition prior to hot rolling compared to the base of the caster. The results for the particle size distribution and precipitate volume fraction are discussed in further detail in Sections 4.3.2 and 4.3.3.

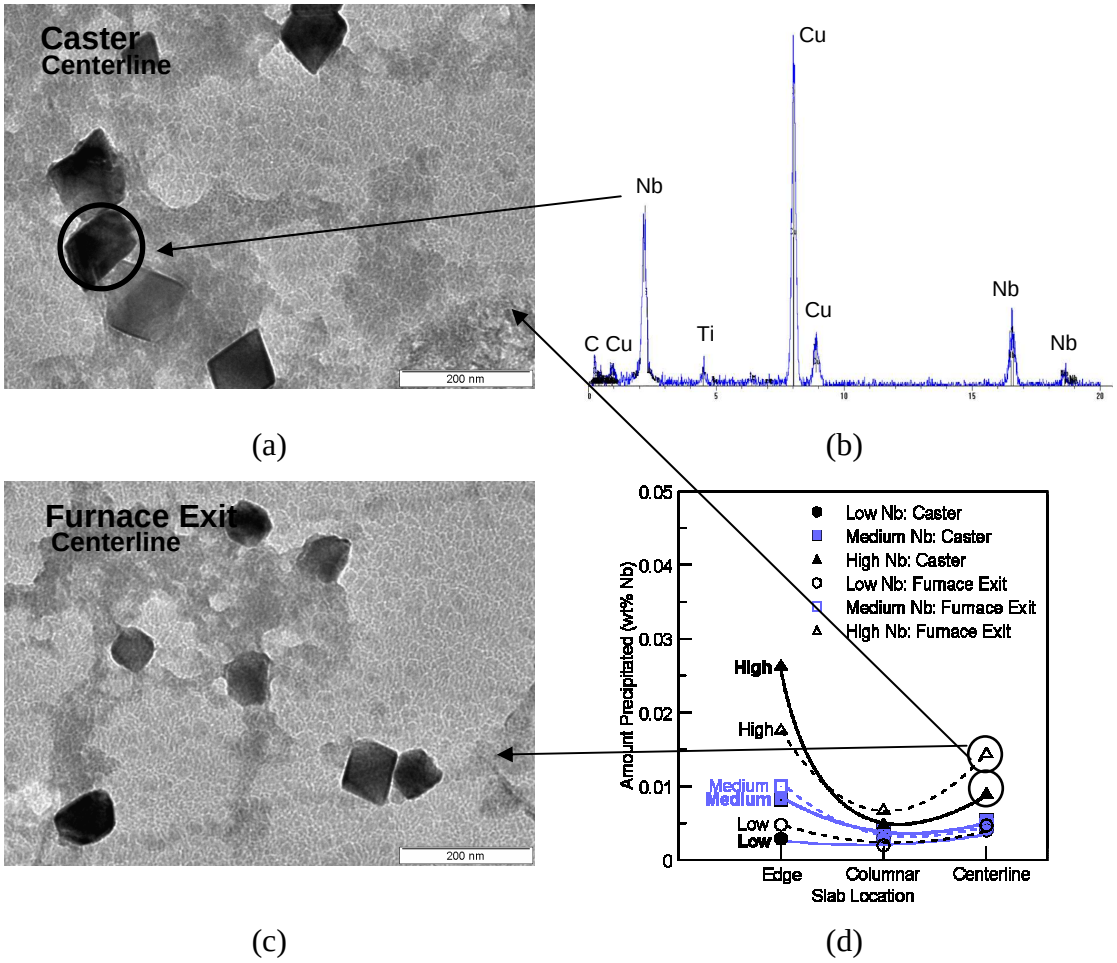

Figure 4.19 TEM analysis of precipitation behavior and corresponding EDS analysis (circled area) in the centerline region relative to process location for the high Nb steel. (a) Precipitates at the base of the caster, (b) corresponding EDS analysis, (c) precipitation at furnace exit, and (d) process and slab location related to micrographs.

Figure 4.20 presents TEM bright field images showing microalloy precipitation which occurred in the slab surface at each process location for the low niobium alloy. Figure 4.20(a) shows precipitation at the base of the caster. The associated EDS analysis is shown in Figure 4.20(b). Titanium-containing particles were present at each process location for the low niobium steel. Alloy precipitation observed in the slab surface at the tunnel furnace exit is shown in Figure 4.20(c). Morphologies including irregular-cuboidal and cuboidal were present. Figure 4.20(d) indicates the process location and alloy of each micrograph presented. For both process locations, the slab surface region demonstrated the highest number density of particles on a given carbon replica.

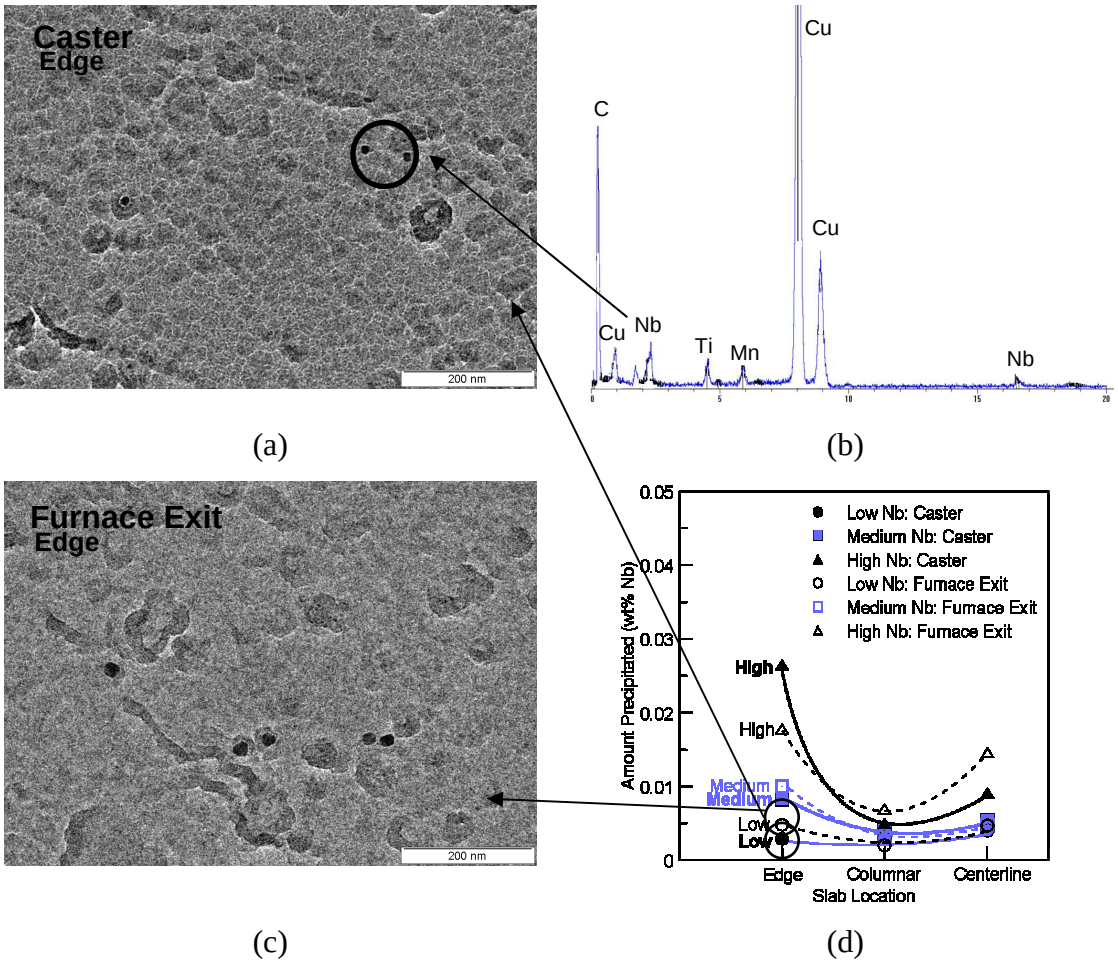

Figure 4.20 TEM analysis of precipitation behavior and corresponding EDS analysis (circled area) on the slab surface relative to process location for the low Nb steel. (a) Precipitates at the base of the caster, (b) corresponding EDS analysis, (c) precipitation at furnace exit, and (d) process and slab location related to micrographs.

However, the particle number density for the low niobium steel per carbon replica was observed to be less than that observed in the high niobium steel. The particle number density observed for the low niobium steel at the slab surface location was observed to be similar for both process locations. Precipitate volume fractions related to particle number density per area (on a given replica) are discussed in detail in Section 4.3.3.

The electrochemical extraction results for the columnar and centerline regions in the low niobium alloy showed an insignificant change (i.e. precipitation or dissolution) through the tunnel furnace. Therefore, the condition prior to hot rolling was selected to demonstrate the general behavior of niobium precipitation for the low niobium alloy. Figure 4.21(a) shows representative microalloy precipitation which occurred in the columnar region at the furnace exit prior to hot rolling for the low niobium alloy. Figure 4.21(b) is the associated EDS analysis. The precipitates observed in the low niobium steel in the columnar region demonstrated similar morphologies (i.e. irregular-cuboidal and cuboidal) as the high niobium alloy. Additionally, the columnar region demonstrated that larger precipitates were present compared to those seen on the slab surface. However, the precipitate size within the columnar region for the low niobium steel was smaller than in the high niobium steel.

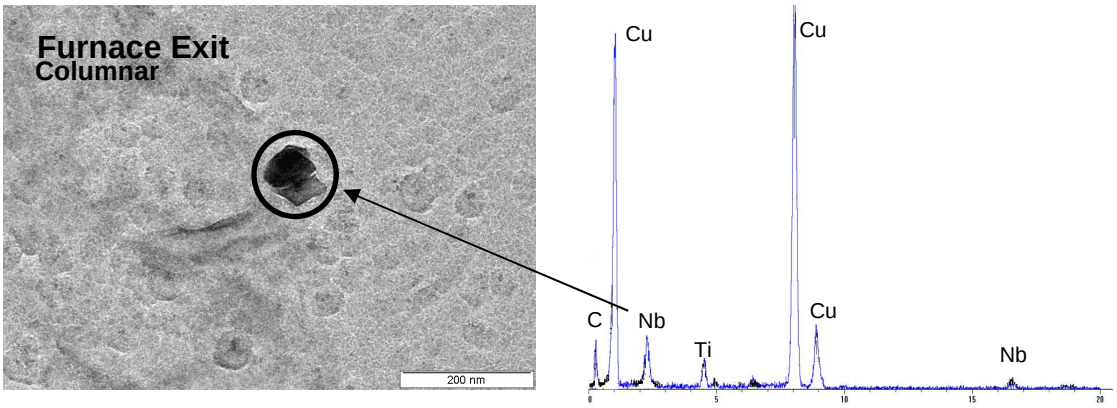

(a) (b)

Figure 4.21 TEM analysis of precipitation behavior and corresponding EDS analysis (circled area) in the columnar region relative to process location for the low Nb steel. (a) Precipitates at the furnace exit and (b) corresponding EDS analysis.

Figure 4.22(a) represents microalloy precipitation in the low niobium alloy upon furnace exit for the centerline region and the corresponding EDS analysis (Figure 4.22(b)). Niobium and titanium were both present in the particles examined. The morphology of the particles was observed to be either irregular or cruciform-type precipitates. The cruciform-type precipitates are circled on the micrograph, which demonstrated arm-like growth. The particles presented for this condition possibly resemble those observed by Wang *et al*. [65]. This observation may suggest that the centerline region for the low niobium steel presents different particle morphology compared to the accompanying specimens observed during this study.

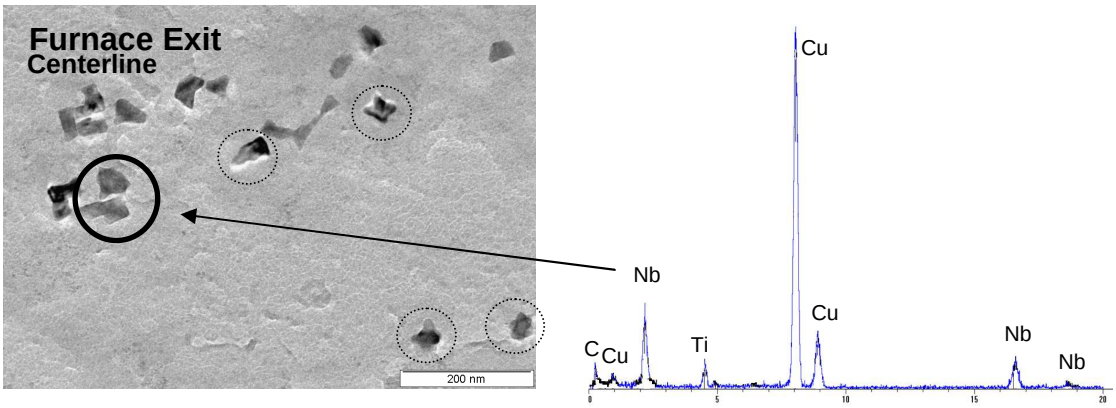

(a) (b)

Figure 4.22 TEM analysis of precipitate behavior and corresponding EDS analysis (bold circled area) in the centerline region relative to process location for the low Nb steel. (a) Precipitates at the furnace, where dashed-circled precipitates resemble cruciform-type morphology, and (b) corresponding EDS analysis.

4.3.2 Precipitate Size Distribution

For precipitate size distribution analysis, particle distributions were assumed to be normal related to the mean "diameter" and standard deviation about the mean [72]. The assumption was based on research reported earlier [67], concerning the precipitate volume fraction calculation, discussed in detail in Section 4.3.3. The equivalent diameter of each particle was found by measuring the length and width of the precipitate, calculating the cross-sectional area, and using the associated diameter (in nm) to represent particle size.

The particle size distributions for precipitation in the slab surface of the high niobium alloy for both process locations are shown in Figures 4.23(a) and 4.23(b), respectively. The particle size distributions at the base of the caster ranges from 3-40 nm, with an average equivalent diameter of approximately 14 nm, while the particle size distribution prior to hot rolling ranges from 3-100 nm, with an average particle diameter of 28 nm. The results show that the average particle in the surface region increased through the tunnel furnace.

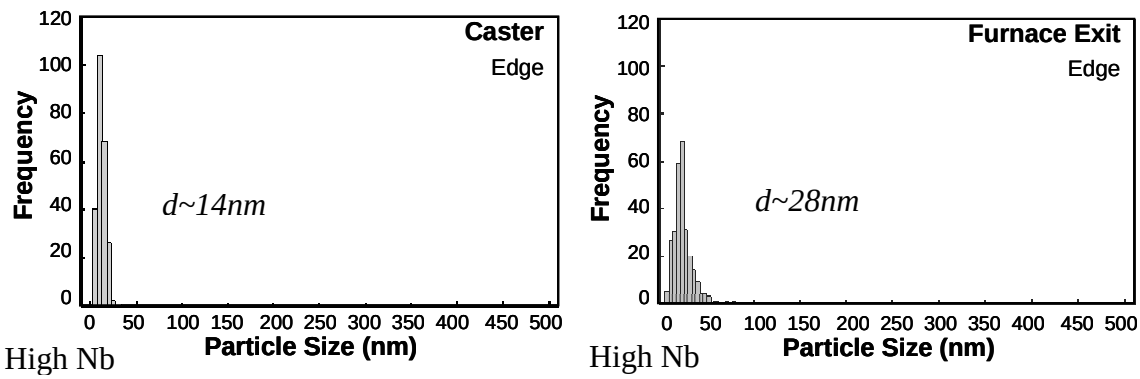

(a) (b)

Figure 4.23 Nb(C,N) particle size distributions in the high Nb alloy on the slab surface observed at (a) the base of the caster and (b) prior to hot rolling.

Figure 4.24(a) presents the particle size distributions at the base of the caster for the columnar region of the high niobium steel. Particle diameters ranged from 15-90 nm, with an average diameter of approximately 27 nm. The size distribution for alloy precipitation in the columnar region, prior to hot rolling, ranged from 10-200 nm with an average particle diameter of 81 nm, as shown in Figure 4.24(b). The relatively large particle diameter range prior to hot rolling may suggest that some particles, which nucleated at the base of the caster, had sufficient time to grow through the tunnel furnace. It is not clear if the smaller precipitates in the caster location dissolve upon equalization in the tunnel furnace or if additional nucleation also occurs.

Figure 4.25 summarizes the particle size distributions in the centerline region at both process locations in the high niobium alloy. The particle diameter at the base of the caster ranged from 10-500 nm as shown in Figure 4.25(a). The associated average

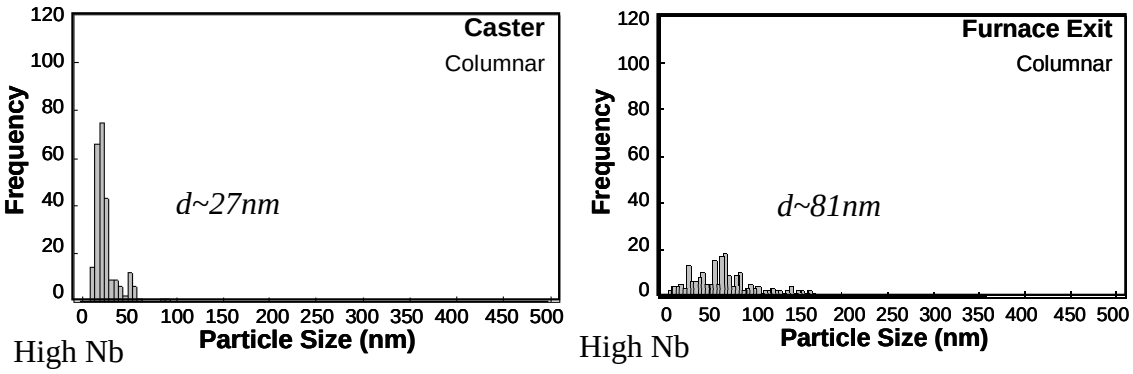

(a) (b)

Figure 4.24 Nb(C,N) Particle size distributions in the high Nb alloy in the columnar region observed at (a) the base of the caster and (b) prior to hot rolling.

particle diameter was approximately 163 nm. The size distribution for precipitation in the columnar region, prior to hot rolling, ranged from 10-200 nm as shown in Figure 4.25(b). The associated average particle diameter prior to hot rolling was 102 nm. The larger particles observed at the base of the caster were not likely the result of the formation of Nb(C,N) particle nucleation on pre-existing larger TiN particles since titanium-rich precipitates did not exhibit substantial niobium content during EDS analysis. The particle size distribution exhibited less variation in the condition prior to hot rolling and a smaller average particle diameter compared to the base of the caster. Overall for the high niobium steel, the centerline region demonstrated the largest particle diameter in conjunction with a large deviation about the mean diameter.

Figure 4.26 shows the particle size distribution in the low niobium alloy. At the base of the caster in the slab surface (Figure 4.26(a)), the particle diameters ranged from approximately 2-35 nm, with an average particle diameter of 12 nm. The particle size distributions for the slab surface, columnar, and centerline regions prior to hot rolling, are presented in Figure 4.26(b). The particle diameter ranged from approximately 5-50 nm in the slab surface prior to hot rolling, with an average particle diameter of 19 nm. The columnar region at the furnace exit exhibited a range in particle diameters from 5-100 nm, with an average particle diameter of 38 nm. The precipitates present in the centerline region prior to hot rolling for the low niobium alloy ranged from approximately 10-150 nm, with an average diameter of 53 nm. Prior to hot rolling, the average particle diameter increased through the thickness of the slab, similar to the trends

observed in the high niobium alloy. The average particle diameters present in the low niobium alloy are clearly smaller than corresponding particles observed in the high niobium grade.

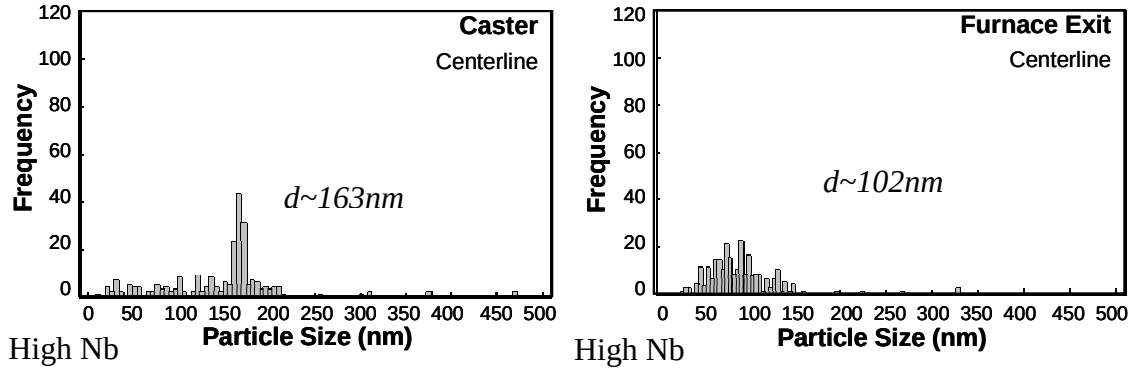

(a) (b)

Figure 4.25 Nb(C,N) Particle size distributions in the high Nb alloy in the centerline region observed at (a) the base of the caster and (b) prior to hot rolling.

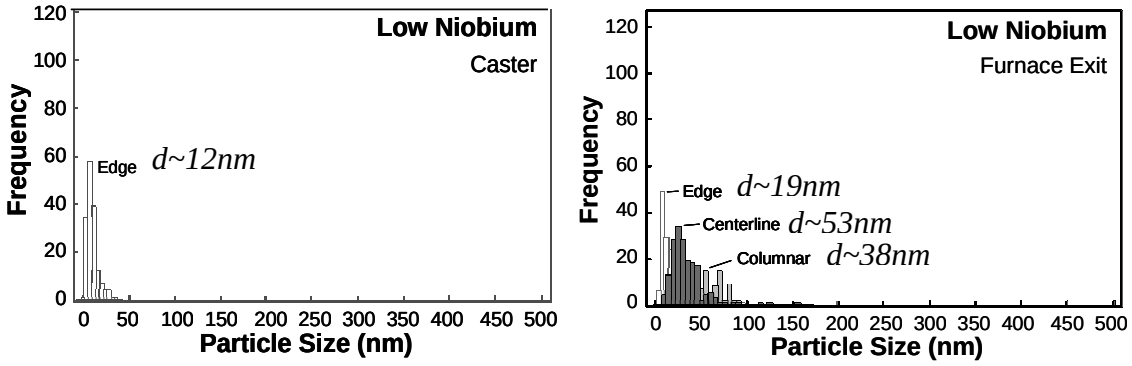

(a) (b)

Figure 4.26 Nb(C,N) particle size distributions in the low Nb alloy at (a) the base of the caster on the slab surface and (b) each solidification region prior to hot rolling.

4.3.3 Precipitate Volume Fraction

Precipitation behavior prior to hot rolling was characterized by transmission electron microscopy of carbon extraction replicas. This method was chosen to supplement the chemical analysis and observe the precipitates independently, providing precipitate size distributions and area particle number densities.

Extraction replicas have been used to demonstrate precipitate size and morphology as discussed previously. However, fewer studies have used the extraction replica method to quantify particle size distributions and volume fractions. Concerning the replica technique, there were two limitations to consider: particles less than 20Å in size could not usually be detected on the replica using standard TEM imaging, which means that the method was resolution-limited. Second, the volume fraction of precipitates was not directly measureable from replica measurements [67]. For the purposes of "volume" fraction measurements in this thesis, it was assumed that precipitation was only present if it was observed, (i.e. if it is greater than 20Å in size). Regarding the determination of precipitate volume fraction, while measurements of the area density of particles can be made, a direct relationship to precipitate volume fraction was not straightforward because the number of particles extracted successfully (extraction efficiency) and the thickness of the "extracted region" itself were not known, and may vary between replicas. Particles with diameters less than the initial etched layer thickness may have been removed during etching, thus unavailable for capture during carbon deposition on the surface. Therefore, the thickness of the extracted region influences which particles may have been available for imaging. Ashby and Ebeling, reporting on the determination of number, size, spacing, and volume fraction of precipitates using carbon replicas, assuming spherical precipitates, suggested that the precipitate volume fraction, f, is approximated by Equation 4.5 [68].

$$f = \frac{\pi}{6}\left[\frac{N_S^{'}}{\alpha}\left(\overline{X_A^2} + \sigma_A^2\right)\right] \tag{4.5}$$

where $N_S^{'}$ = measured number of precipitates per unit area on the extraction replica

α = extraction efficiency; the replicated surface depth is taken as double the arithmetic mean of particle diameters, and the extraction efficiency incorporates this variable.

$\overline{X}_A$ = arithmetic mean of particle diameters.

σ_A = standard deviation from this mean.

It was evident that the precipitate volume fraction was reliant on the extraction efficiency. The particle size distribution could also be influenced by the extraction process if extraction efficiency was size dependent. Thus, the results should be used with caution when the replica technique is used for estimating the volume fraction of precipitates. Nonetheless, a method used by Hansen, for the determination of relative precipitate volume fractions using the extraction replica techniques, employs a parameter K based on Equation 4.6 [67].

$$\mathrm{K} = N_S^{'}\left(\overline{X}_A^2 + \sigma_A^2\right) = \frac{6f\alpha}{\pi} \tag{4.6}$$

The extraction efficiency, α, was assumed independent of particle size based on the reproducibility of particle size distribution results reported by Ashby and Ebeling [68]. Thus, α was also taken to be constant for the results reported in this thesis [Equation 4.5]. Although the absolute values of the precipitate volume fraction cannot be reported, this assumption makes the parameter K, proportional to the precipitate volume fraction [67]. Equation 4.6 also included the assumption that the particle size distribution as normal and the precipitate morphology was spherical.

Figure 4.27 shows the precipitate volume fraction as a function of the K parameter plotted against the through thickness position for each sample location examined during this study. Table B1 presents the quantitative K parameter results for each process condition, alloy concentration, and solidification region. For the quantitative measurement of precipitate volume fractions, the specimens evaluated using the K parameter were the same samples examined using TEM microscopy (Figure 4.14). For this study, areas of relatively high particle number densities had been randomly chosen to photograph and characterize size distributions for each specimen. The same micrographs were later used for the determination of measured number of precipitates per unit area on the extraction replica. Similar to the size distribution analysis, the cross-sectional area of a precipitate was found by measuring the length and width of the particle. From the cross-sectional area, the equivalent diameter was calculated to represent precipitate size. For each specimen, three replicas were examined at ten fields of view per replica.

The precipitate volume fraction results indicate that the position dependency mirrors the chemical extraction results described in Section 4.2.4, where the slab surface and the centerline regions in the high niobium steel (for both process locations) exhibited a larger amount of precipitation. However, the precipitation volume fraction results (based on the K parameter) suggest that the largest amount of precipitation occurred in the high niobium steel in the centerline region. It was also evident that the high niobium steel contained a much higher precipitate volume fraction than observed in the low niobium steel. The columnar region, which represented the bulk of the slab volume, demonstrated the least amount of precipitation in terms of particle density per area on a given replica. The high niobium steel apparently experienced precipitate dissolution in the slab surface through the tunnel furnace. However, this alloy may have experienced some precipitation in the centerline region of the slab during equalization through the tunnel furnace. The amount of niobium precipitation was greatest in the centerline region in the high niobium alloy prior to hot rolling. These behaviors may be related to the temperature profile of the slab as it travels through the equalization furnace. The slab surface temperature is less than that of the tunnel furnace; thus some reheating of the slab surface occurs, which may cause precipitate dissolution within that region of the as-cast slab. Although the temperature of the centerline region is not accurately known, alloy measurements by TEM and precipitate volume fraction analysis through the tunnel furnace are consistent with the centerline cooling (rather than heating) in the tunnel furnace (see Figure 4.12). This behavior is apparent in the high niobium alloy in the centerline region of the cast slab as shown in Figure 4.27. Slow cooling of the centerline region may allow sufficient time for precipitation nucleation and growth.

4.4 General Discussion

A schematic illustration summarizing the sampling regions is shown in Figure 4.28. The average results from electrochemical dissolution for all steels and sampling locations are plotted in Figure 4.29 in comparison to the precipitate volume fraction estimated using the K parameter on carbon extraction replicas. The electrochemical extraction results showed that the greatest amount of alloy precipitation occurred in the slab surface along the edges of the continuously cast thin slab (i.e. the

slab corner location) in the high niobium steel. The precipitate volume fraction results demonstrated a similar character as chemical extraction results. However, the precipitate volume fractions indicated that the greatest amount of precipitation was present in the centerline region of the high niobium steel, rather than the slab surface. The extent of

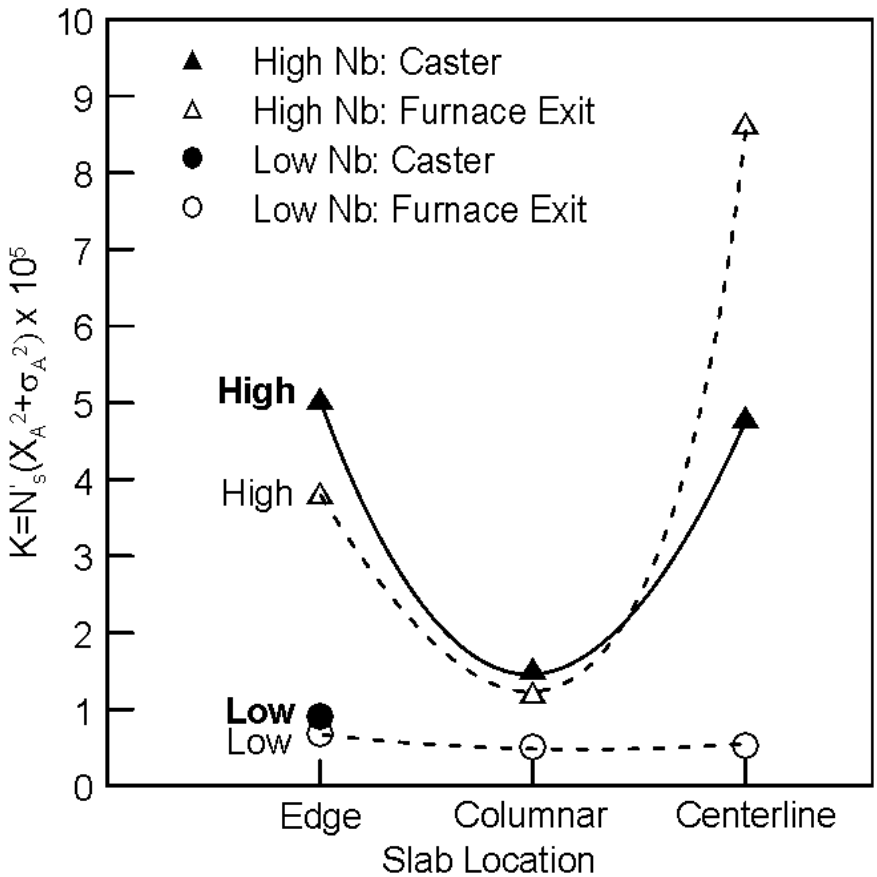

Figure 4.27 Precipitate volume fractions determined by the K parameter versus the through thickness of the slab.

precipitation appeared greatest in the high niobium steel, where dissolution of precipitates at the edge/slab surface subsequently occurred during reheating and equalization in the tunnel furnace, while some precipitation was observed in the centerline region. The columnar region represented the bulk of the slab volume, and exhibited the lowest amount of precipitated niobium. The high percentage of niobium precipitation in the slab edges can be understood in terms of the slab surface temperature and solubility of niobium carbonitrides. The lower temperatures of the slab surface at the base of the caster are associated with an increased driving force for alloy precipitation, and therefore

conditions are conducive to precipitation in the surface/edge/corner regions. Increasing the niobium content also increases the supersaturation and allows niobium precipitation to occur at higher temperatures and in greater amounts.

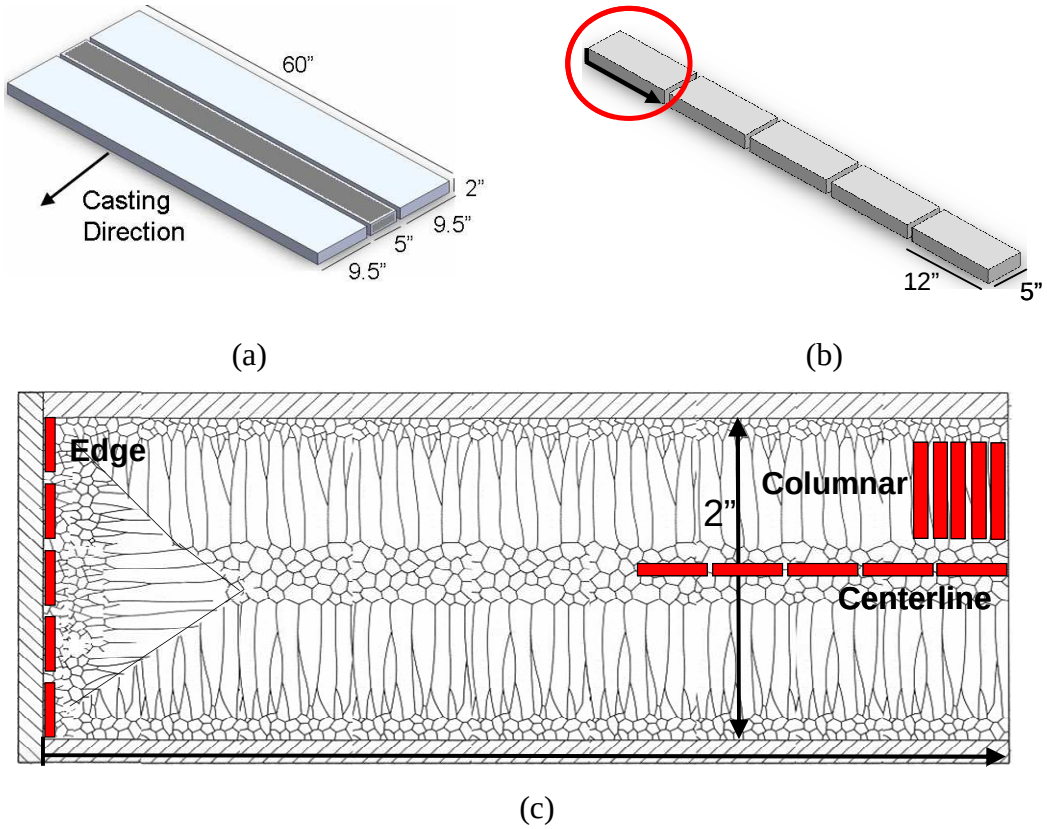

Figure 4.28 (a) Initial slab dimensions and (b) section of material studied.
(c) Sample locations and orientations in the slab.

The precipitate fraction results suggest that some niobium dissolution in the high niobium alloy occurs during processing through the tunnel furnace. The soaking time and temperature within the tunnel furnace “equalized” the temperature profile of the slab, increasing niobium solubility in the previously cooler regions of the casting (i.e. at the surface). This effect is beneficial because the dissolved niobium in the austenite is available to enhance the thermomechanical processing response and final properties. An increased amount of niobium was also seen to precipitate within the centerline region (relative to the columnar region), presumably caused by the alloy rich liquid present during the final stage of solidification. The medium niobium alloy also demonstrated more precipitation in the slab surface, with less precipitation present in the columnar and

centerline regions. In this alloy, there was little difference (i.e. precipitation and dissolution) between process locations. In the low niobium steel, it appeared that some niobium precipitation may occur during equalization in the tunnel furnace, prior to hot rolling. However, no substantial change (i.e. precipitation and dissolution) occured in this alloy between process locations and solidification regions.

Figure 4.30 shows a summary of the particle size distributions for the as-cast slab solidification and process locations for the low and high niobium alloys. It is observed that the average particle diameter at the base of the caster for the edge and columnar regions was smaller than the mean particle diameter prior to hot rolling in the high niobium alloy.

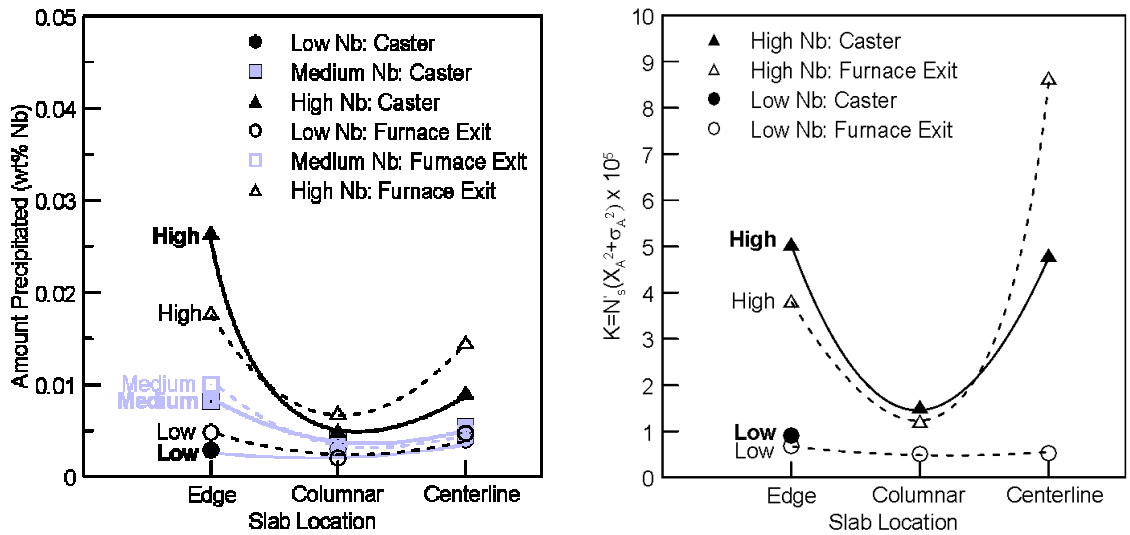

(a) (b)

Figure 4.29 (a) Niobium in precipitate form measured by ICP-AES (in wt. pct.) plotted against the sample location through the thickness of the slab and (b) precipitate volume fraction represented by the K parameter versus the slab location for selected alloys and process locations.

The precipitate morphologies can be described as irregular-cuboidal and cuboidal. The average particle diameter was smaller at the slab surface and increased through the thickness of the slab. This increase in particle diameter may suggest that the particles grow during equalization prior to hot rolling. The higher number density of particles on the slab surface could be caused by increased nucleation associated with greater cooling of the slab surface during casting.

During the production of the trial niobium alloys, the material underwent a process known as liquid core reduction (LCR). During LCR, the material is "squeezed" subsequent to the first segment and prior to the second segment of containment rolls during continuous casting. LCR is used to reduce the likelihood of centerline segregation and to pre-condition the material prior to hot rolling. Initial reduction (LCR) during casting is done primarily on niobium bearing HSLA steels due to the difficulties

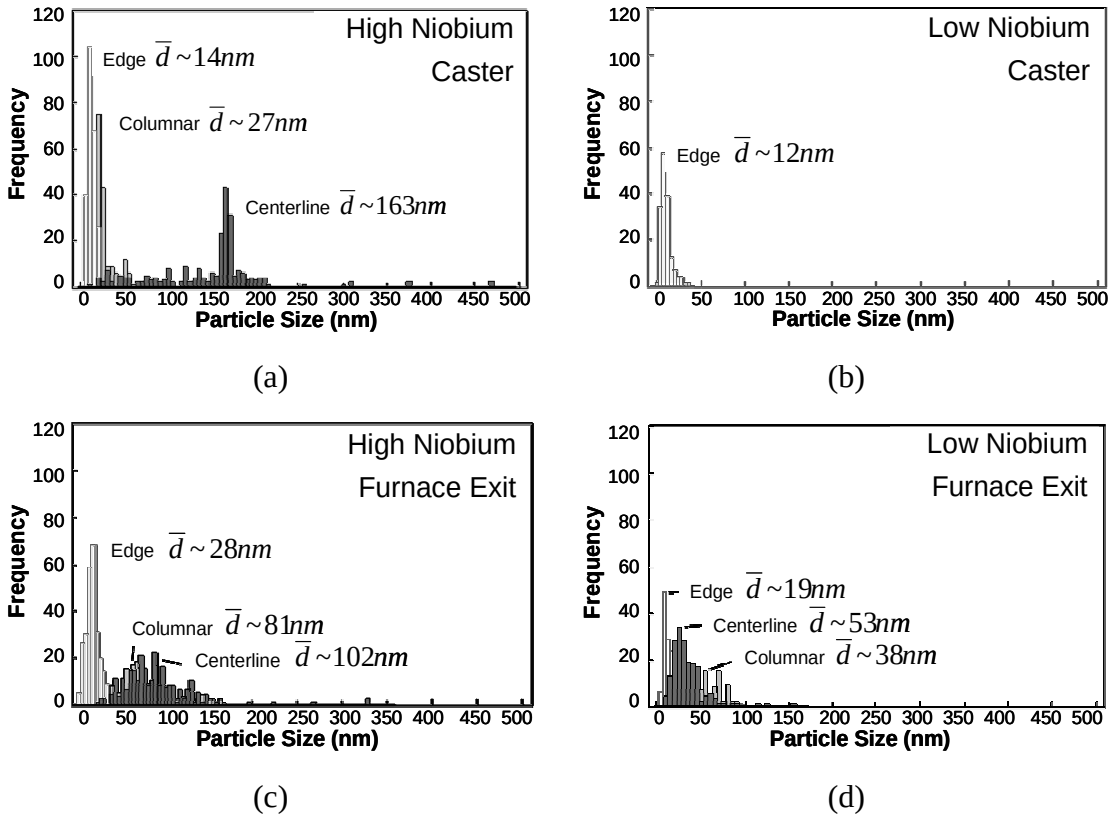

Figure 4.30 Particle size distributions relative to thermal profile of the slab and process location for the selected alloys, process locations, and solidification regions. Combined particle distributions for (a) the base of the caster for the high niobium alloy, (b) base of the caster for the low niobium alloy, (c) high niobium alloy prior to hot rolling, and (d) low niobium alloy prior to hot rolling.

encountered during rolling these specific grades [69]. LCR typically involves an average 4 mm reduction on an initial slab thickness of 60 mm (~7pct. reduction). While it is not clear that substantial strain is imported to the (colder) solidified outer shell, it is possible

that any strain imported to the slab surface during the LCR process may enhance localized precipitation on the solidified shell of the as-cast slab.

For the edge location, there appeared to be a higher number density of particles present at the base of the caster compared to the furnace exit, consistent with alloy dissolution through the tunnel furnace at the slab surface (Figure 4.29(b)). The particle number densities for the high niobium alloy at the base of the caster, for the columnar and centerline regions, were smaller than upon furnace exit, which suggests precipitation through the tunnel furnace, again consistent with the trends in Figure 4.29(a).

CHAPTER 5 : CONCLUSIONS

This research was directed towards understanding niobium precipitation in hot-charged slabs relative to alloy concentrations, process location, and solidification region within the slab. Steels containing low, medium, and high concentrations of niobium were tested at multiple slab locations. Preliminary results from a vanadium-containing steel confirmed that vanadium remained in solution prior to hot rolling and thus the quenching method used for sample collection during CSP processing was sufficient. Replicate testing also showed that the electrochemical extraction method was reproducible.

The sampled regions for electrochemical dissolution included the chill zone (i.e. slab corner), the columnar region, and the centerline of the slab. The slab surface/edge results exhibited greater variability between replicate samples and more precipitation in the high and medium niobium alloys. In the high niobium alloy, some niobium dissolution occurred during equalization in the tunnel furnace. This behavior was consistent with the lower solubility associated with higher niobium levels and lower temperature. The absolute amount of niobium in precipitated form was greatest in the high niobium steel, while the relative amount was greatest in the low niobium steel. Most notably, the high niobium alloy demonstrated the greatest amount of precipitation in the slab surface at the base of the caster, relative to corresponding conditions. The amount of precipitation in the centerline region was slightly greater compared to the columnar region. The columnar region that comprised the bulk volume of the material demonstrated less variability between samples in comparison to the edge location, and importantly, the least amount of precipitation overall.

TEM analysis was completed on selected trial niobium alloys, process locations, and solidification regions. The high niobium alloy in the slab surface/edge/corner region, for both process locations, exhibited relatively small (10-30nm) irregular-cuboidal and cuboidal precipitates. The smaller precipitate diameter and greater amount of

precipitation in the slab surface could be understood in terms of the thermal profile of the slab, and the increased driving force for alloy precipitation at lower temperatures. The columnar and centerline regions for the high niobium steel contained larger irregular-cuboidal and cuboidal precipitates. Similarly, the low niobium alloy contained the same morphologies in the slab surface and columnar regions as observed in the high niobium steel. However, the centerline region in the low niobium alloy also contained some precipitates (of cruciform-type morphology) that possibly suggested nucleation and growth on a preexisting precipitate (i.e. TiN).

The average particle diameter increased through the slab thickness (i.e. slab surface/edge, columnar, and centerline) for the low and high niobium alloys. The centerline region for the low and high niobium alloys contained the greatest average particle diameter. The average particle diameter present in the high niobium alloy (in each solidification region and process location) was greater than observed in the low niobium alloy.

The results of precipitation volume fraction measurements based on examination of carbon extraction replicas suggested that the greatest amount of precipitation (i.e. particle number density) was present in the centerline region of the high niobium alloy prior to hot rolling. In the high niobium alloy, there was a higher number density of particles in the centerline region prior to hot rolling, relative to the base of the caster, suggesting niobium precipitation occurs in the centerline during the tunnel furnace equalization. The columnar region demonstrated a relatively low number density of particles per replica. The number density of particles per replica for the centerline location (for the low and high niobium alloys) was greater than that of the columnar region, but less than the number density of particles seen at the slab surface. The particle number density in the slab edge for the high niobium alloy at the base of the caster was greater than prior to hot rolling. Thus, the slab surface experienced niobium dissolution through the tunnel furnace in the slab edge location. The overall character of the precipitation volume fraction results was similar to the chemical extraction results, except that the centerline region demonstrated the highest amount of precipitation, in the high niobium steel based on the K parameter results. Although the extraction efficiency, α, was assumed to be independent of particle size for this study, it is reasonable to expect

that extraction efficiency is influenced by particle size. The significantly larger particle size in the centerline region (as compared to the slab surface) may have influenced the observed increase in niobium precipitation in the centerline in the K parameter results, relative to the electrochemical analysis results.

CHAPTER 6 : FUTURE WORK

Although this study focused on the behavior of microalloy precipitation in hot charged slabs of niobium-bearing HSLA steels, the effects of other alloying additions on the behavior of niobium precipitation are not as well known. It would be beneficial to introduce small titanium additions in conjunction with varying amounts of niobium, and investigate the relative effects on the behavior of microalloy precipitation. In order to test the effects of microalloy precipitation prior to hot rolling and the associated mechanical properties, it would be useful to obtain samples at the base of the caster, prior to hot rolling, and subsequent hot rolling (i.e. coil product). It would also be of interest to determine the influence of microalloy precipitation behavior on the mechanical properties of the final coil product.

The vanadium-containing alloy was used primarily for the determination of the sampling method and quenching process. The CMn(VNb) alloy was characterized using single replicates for each process location (i.e. base of the caster, prior to hot rolling, and ID/OD of the coil) and solidification region (i.e. slab surface/edge, columnar, and centerline). It would be beneficial to further explore the behavior of microalloy precipitation in a similar vanadium-containing alloy and the related effects on niobium precipitation.

Other areas of interest include using the experimental results from the CMn(Nb) trial steels obtained by the electrochemical extraction technique for each alloy content, process location, and solidification region (Section 4.2), to better model alloy precipitation during prior to hot rolling. Currently, Xu *et al*. are considering the results to accurately model the kinetics of alloy precipitation necessary to predict niobium precipitation during continuous casting and quenching [16].

REFERENCES

1. P.T Mazzare, "Microalloy Precipitate Dissolution and Grain Coarsening Kinetics in 0.2 Weight Percent Carbon Steels," M.S. thesis, Colorado School of Mines, Golden, CO, 1987.

2. J.M. Gray, "Niobium Bearing Steels in Pipeline Projects," Microalloying International, Inc., Houston, Texas, USA, 1995.

3. L. Toth, "Transition metal carbides and nitrides", New York, Academic Press, 1971.

4. R. Honeycombe, *Structure and strength of alloy steels.* (London: Climax Molybdenum Co.), 1996.

5. C.P. Reip, S. Shanmugam, and R.D.K. Misra, "High strength microalloyed CMn(V-Nb-Ti) and CMn(V-Nb) pipeline steels processed through CSP thin-slab technology: Microstructure, precipitation and mechanical properties," *Materials Science and Engineering: A* 424, no. 1 – 2, May 25, p. 307 – 317, 2006.

6. G. Krauss, *Steels: processing, structure, and performance* (Materials Park Ohio: ASM International, p. 138 – 143, 2005.

7. N.T. Porter, "Reheat Furnace Dissolution Kinetics of Niobium Bearing HSLA Steels for Automotive, Pipeline, and Structural Applications," MS Thesis, Colorado School of Mines, Golden, CO, July, 2008.

8. J.A. Garrison, "Aluminum Nitride Precipitation Behavior in Thin Slab Material," M.S. thesis, T-6033, Colorado School of Mines, Golden, Colorado, 2005.

9. M.G. Akben, I. Weiss, J.J. Jonas, "Dynamic Precipitation and Solute Hardening in a V Microalloyed and Two Nb Steels Containing High Levels of Mn," *Acta Metallurgica*, 29, p. 111 – 121, 1981.

10. L.E. Collins, D.L. Baragar, J.T. Bowker, "Steckel Mill Process Optimization for Production of X70 and X80 Gas Transmission Linepipe," *Microalloying '95* , p. 141 – 147, 1995.

11. K. Hulka, "Alloy Design, Processing and Application of High Strength Steels," *Metallurgy and New Materials*, 3, p. 1 – 22, 1995.

12. L.J. Cuddy and J.C. Raley, "Austenite Grain Coarsening in Microalloyed Steels," *Metallurgical Transactions A*, Vol. 14A, p. 1989 – 1995, 1983.

13. A.L. Rivas, D.K. Matlock, and J.G. Speer, "Quantitative Analysis of the Nb in Solution in a Microalloyed Carburizing Steel by Electrochemical Etching," *Materials Characterization*, Vol. 59, p. 571 – 577, 2008.

14. A.L. Rivas, E. Vidal, D.K. Matlock, and J.G. Speer, "Electrochemical Extraction of Microalloy Carbides in Nb-Steel," *Revista de Metalurgia*, Vol 44, No 5, p. 447-456, 2008.

15. E.J. Pavlina, Colorado School of Mines, private communication, 2008.

16. K. Xu, B.G. Thomas, R. O'Malley, "Equilibrium Model of Precipitation in Microalloyed Steels," Accepted by *Metallurgical and Materials Transaction A*, in press, 2010.

17. J. K. Brimacombe, "Continuous Casting of Steel Billets, Blooms and Slabs," *Brimacombe Continuous Casting Course*, Vol. 1, Vol. 2, Reproduced in 2007.

18. E.J. Pavlina, J.G. Speer, and C.J. Van Tyne "Transformation of Austenite in Molybdenum-containing Low-carbon Steels," Colorado School of Mines, Advanced Steel Processing and Products Research Center, Research Report, MT-SRC-010-003, Section 2.0, March 2010.

19. R.C. Skagen and D.C. Gilbert, "CSP Tunnel Furnace at Nucor Steel, Hickman," Iron and Steel Engineer, Vol. 72, No. 5, p. 42 – 44, May 1995.

20. K. Hensger, "Recent Developments in Compact Strip Produciton of Nb-Microalloyed Steels," Microalloying Conference Proceedings, 2001.

21. C. Reip, "Development of CSP Processed High Strength Pipe Steels," *Materials Science Forum* Vol. 500/501, p. 287 – 294, 2005.

22. P. Lubensky, "High Strength Steel Processing Via Direct Charging Using Thin Slab Technology," Microalloy '95, Pittsburgh, PA, p. 225, June 1995.

23. K. Wunnenberg and K. Schwerdtfeger, "Principles in Thin Slab Casting," *Iron & Steelmaker*, Vol. 22, No. 4, p. 25 – 31, April 1995.

24. G. Backmann, A. Kothe, W. Loser, J. Richter, T. Schubert, S. Thiem, and L. Hering, "Investigation of the Solidification Behavior and Mechanical Properties of Thin Billets," *Stalh u. Eisen*, Vol. 113, p. 63 – 66, 1993.

25. R. J. Glodowski, "Experience in Production V-Microalloyed High Strength Steel by Thin Slab Casting Technology," International Symposium of Thin Slab Casting and Rolling – TSCR, 2002.

26. C. Klinckenberg and K.E. Hensger, “Processing of Niobium Microalloyed API Grade Steel on a Thin Slab Plant,” Materials Science Forum, Vol. 500/501, p. 253 – 260, 2005.

27. J.K. Brimacombe and I.V. Samarasekera, “The Challenge of Thin Slab Casting,” Iron & Steelmaker, Vol. 21, No. 11, p. 42 – 44, November 1994.

28. C. A. Muojekwu, D. Q. Jin, I. V. Samarasekera, and J. K. Brimacombe, “Thermomechanical History of Steel Strip During Hot Rolling- A Comparison of Conventional Cold-Charge Rolling and Hot-Direct Rolling of Thin Slabs,” 37th MWSP Conference Proceedings, Warrendale, PA, USA, ISS, Vol. 33, p. 617–633, 1996.

29. A.J. Shutts, Melt-Shop Metallurgist, Nucor Steel – Hickman, private communication, November, 2008.

30. H. Yu, Y. L. Kang, H.B. Dong, D. L. Liu, and J. Fu, “Analysis on the Behavior of Precipitates in Ultra-Thin Hot Strip of Plain Low Carbon Steel Produced by Compact Strip Production,” *Acta Metal. Sinica English Letters*, Vol. 15, p. 375 – 379, 2002.

31. X. Huo, D. Liu, Y. Wang, N. Chen, Y. Kang, and J. Fu, “Grain Refinement of Low Carbon Steel Produced by CSP Process,” *Journal of University Science and Technology Beijing*, Vol. 11, p. 133 – 137, 2004.

32. D. Zhou, J. Fu, Y. Kang, Z. Wang, J. Li, and Z. Xu, “Metallurgical Quality of CSP Thin Slabs,” *Journal of University of Science and Technology Beijing*, Vol. 11, No. 2, p. 106 –109, April 2004.

33. D. Liu, Y. Wang, X. Huo, N. Chen, W. Shao, J. Fu, and Y. Kang, “Grain Refinement and Strengthening of Low Carbon Steel by CSP Technology,” *Acta Metallurgica Sinica*, Vol. 38, No. 6, p. 647 – 651, June 2002.

34. T. Gladman, *The Physical Metallurgy of Microalloyed Steels*, Book 615, The Institute of Materials, London, 1997.

35. A.T. Davenport, L.C. Brossard, and R.E. Miner, "Precipitation in Microalloyed High-Strength Low-Alloy Steels," *Journal of Metals*, Vol. 27, p. 21 – 26, 1975.

36. H. Adrian and F.B. Pickering, "Effect of Titanium Additions on Austenite Grain-growth Kinetics of Medium Carbon V-Nb Steels containing 0.008-0.018-percent-N," *Materials Science and Technology*, Vol. 7, p. 176 – 82, 1991.

37. K. Hulka, J.M. Gray, and F. Heisterkamp, "Metallurgical Concept and Full-Scale Testing of a High Toughness, H2S Resistant 0.03%C-0.10%Nb Steel," *Niobium Technical Report*, NbTR, August, 1990.

38. G. Tither, "Steel Design for Relaxed Controlled Processing," *Steel Technology International*, Sterling Publications, London, p. 219 – 223, 1992.

39. M.G. Akben, B. Bacroix, and J.J. Jonas, "Effect of Vanadium and Molybdenum Addition on High Temperature Recovery, Recrystallization, and Precipitation Behavior of Niobium-based Microalloyed Steels," *Acta Metallurgica*, Vol. 31, p. 161 –174, 1983.

40. S. Koyama, T. Ishii, and K. Narita, "Effects of Manganese, Silicon, Chromium, and Nickel on the Dissolution and Precipitation of Niobium Carbide in Iron Austenite," *Journal of the Japan Institute of Metals*, Vol. 35, p. 1089 –1094, 1971.

41. S. Kurokawa, J.E. Ruzzante, A.M. Hey, and F. Dyment, "Diffusion of Niobium in Iron and Iron Alloys," *Metal Science*, Vol. 17, p. 433 – 438, 1983.

42. H.S. Ubhi and T.N Baker, "The Influence of Manganese and Silicon on the Precipitation of Vanadium Carbide in Steel," *Materials Science and Engineering A*, Vol. 111, p. 189 –199, 1989.

43. J.X. Dong, F. Siciliano Jr., J.J. Jonas, W.J. Liu, and E. Essadiqi, "Effect of Silicon on the Kinetics of Nb(C,N) Precipitation during the Hot Working of Nb-bearing Steels," *ISIJ International*, Vol. 40, p. 613 – 618, 2000.

44. M. Grujicic, A. M. Sarosiek, L. Kaufman and W. S. Owen, "The Carbonitride/ Austenite Equilibrium in Fe-(C+N)-V-Nb-Mn System," Calphad, 9, p. 117 – 128, 1985.

45. M. Grujicic, L. Kaufman and W. S. Owen, "The (V, Nb)(C, N) Precipitate/Austenite Equilibrium in the Fe-C-N-V-Nb-Mn System," Calphad, 10, No. 1, p. 37 – 47, 1986.

46. M. Grujicic, I. J. Wang and W. S. Owen, "On the Formation of Duplex Precipitate Phases in an Ultra-low Carbon Micro-alloyed Steel," Calphad 12, No 3, p. 261-275, 1988.

47. S.W. Thompson, D.J. Colvin, G. Krauss, “Precipitation in high strength low alloy (HSLA) steel: a TEM study,” Materials Science and Engineering A, Vol. 323, Issues 1-2, p. 285 – 292, January 2002.

48. A.J. Craven, K. He, L.A.J. Garvie, and T.N. Baker, "Complex Heterogeneous Precipitation in Titanium-Niobium Microalloyed Al-killed HSLA Steels-I," *Acta Materialia*, Vol. 48, p. 3857 – 3868, 2000.

49. S. Shanmugam, M. Tanniru, R.D.K. Misra, D. Panda, and S. Jansto, "Microalloyed V-Nb-Ti and V Steels Part 2 - Precipitation Behavour during Processing of Structural Beams," *Materials Science and Technology,* Vol. 21, p. 165 –177, 2005.

50. R. Wang, C.I. Garcia, M. Hua, K. Cho, H. Zhang, and A.J. DeArdo, "Microstructure and Precipitation Behavior of Nb, Ti Complex Microalloyed Steel Produced by Compact Strip Processing," *ISIJ International,* Vol. 46, p. 1345 –1353, 2006.

51. K.A. Taylor, "Solubility Products for Titanium-, Vanadium-, and Niobium-Carbide in Ferrite," *Scripta Metallurgica et Materialia,* Vol. 32, p. 7 –12, 1995.

52. F.H. Froes, R.W.K. Honeycombe, and D. H. Warrington, "Conditions Controlling Matrix and Stacking Fault Precipitation," *Acta Metallurgica,* Vol. 15, p. 157 – 159, 1967.

53. M. Prikryl, A. Kroupa, G.C. Weatherly, and S.V. Subramanian, "Precipitation Behavior in a Medium Carbon, Ti-V-N Microalloyed Steel," *Metallurgical and Materials Transactions A,* Vol. 27, p. 1149 –1165, 1996.

54. R.D.K. Misra, K.K. Tenneti, G.C. Weatherly, and G. Tither, "Microstructure and Texture of Hot-rolled Cb-Ti and V-Cb Microalloyed Steels with Differences in Formability and Toughness," *Metallurgical and Materials Transactions A,* Vol. 34, p. 2341 – 2351, 2003.

55. R.D.K. Misra, H. Nathani, J.E. Hartmann, and F. Siciliano, "Microstructural Evolution in a New 770 MPa Hot Rolled Nb-Ti Microalloyed Steel," *Material Science and Engineering A,* Vol. 394, p. 339 – 352, 2005.

56. J. Irvine and T.N. Baker, "The Influence of Rolling Variables on the Strengthening Mechanisms Operating in Niobium Steels," *Materials Science and Engineering A,* Vol. 64, p. 123 – 134, 1984.

57. M.A. Altuna, A. Iza-Mendia, and I. Gutierrez, "Precipitation Strengthening Produced by the Formation in Ferrite of Nb Carbides," *La Metallurgia Italiana,* p. 41 – 47, 2009.

58. M. Charleux, W.J. Poole, M. Millitzer, and A. Deschamps, "Precipitation Behavior and Its Effect on Strengthening of an HSLA-Nb/Ti Steel," *Metallurgical and Materials Transactions A,* Vol. 32, p. 1635 – 1647, 2001.

59. R.M. Poths, R.L. Higginson, and E.J. Palmiere, "Complex Precipitation Behaviour in a Microalloyed Plate Steel," *Scripta Materialia,* Vol. 44, p. 147 – 151, 2001.

60. S.G. Hong, K.B. Kang, and C.G. Park, "Strain-induced Precipitation of NbC in Nb and Nb-Ti Microalloyed Steels," *Scripta Materialia*, Vol. 46, p. 163 –168, 2002.

61. H.J. Jun, K.B. Kang, C.G. Park, "Effects of Cooling Rate and Isothermal Holding on the Precipitation Behaviour During Continuous Casting of Nb-Ti Bearing HSLA Steels," *Scripta Materialia*, Vol. 49, p. 1081 – 1086, 2003.

62. N. Maruyama, R. Uemori, and M. Sugiyama, "The Role of Niobium in the Retardation of the Early Stage of Austenite Recovery in Hot-deformed Steels," *Materials Science and Engineering A*, Vol. A250, p. 2 – 7, 1998.

63. G.I. Rees, J. Perdix, T. Maurickx, and H.K.D.H. Bhadeshia, "Effect of Niobium in Solid Solution on the Transformation Kinetics of Bainite," *Materials Science and Engineering A*, Vol. 194, p. 179 – 186, 1995.

64. S.S. Hansen, J.B. Vander Sande, and M. Cohen, "Niobium Carbonitride Precipitation and Austenite Recrystallization in Hot-Rolled Microalloyed Steels," *Metallurgical Transactions A*, Vol. 11A, p. 387 – 402, March 1980.

65. R. Wang, C.I. Garcia, M. Hua, H. Zhang, and A.J. DeArdo, "The Microstructure Evolution of Nb, Ti Complex Microalloyed Steels During the CSP Process," *Materials Science Forum*, Vol. 500-501, p. 229-236, 2005.

66. M. Suehiro, Z.-K. Liu, and J. Gren, "Effect of Niobium on Massive Transformation in Ultra Low Carbon Steels: A Solute Drag Treatment," *Acta Materialia*, vol. 44, pp. 4241-4251, 1996.

67. S.S. Hansen, "The Thermomechanical Treatment and Transformation Behavior of Niobium High – Strength, Low – Alloy Steels," Ph.D. thesis, Massachusetts Institute of Technology, February 1978.

68. M.F. Ashby and R. Ebeling, "On the Determination of the Number, Size, Spacing, and Volume Fraction of Spherical Second-Phase Particles from Extraction Replicas," *Transactions of the Metallurgical Society of AIME*, Vol. 236, p. 1396-1404, October 1966.

69. B. Hanna, Caster Engineer, Nucor Steel – Hickman, private communication, October 21, 2010.

70. J.G. Speer, J.R. Michael, S.S Hansen, "Carbonitride Precipitation in Niobium/Vanadium Microalloyed Steels," *Metallurgical Transactions A*, vol. 18A, p. 211-222, February 1987.

71. J.G. Speer and S.S. Hansen, “Austenite Recrystallization and Carbonitride Precipitation in Niobium Microalloyed Steels,” *Metallurgical Transactions A*, vol. 20A, p. 25-38, January 1989.

72. C. J. Van Tyne, Advanced Steel Processing and Products Research Center, Colorado School of Mines, private communication, November 9, 2010.

APPENDIX A

APPENDIX A: Uncertainty analyses using 95% confidence interval about the mean of electrochemical extraction results for each alloy, process location, and solidification region.

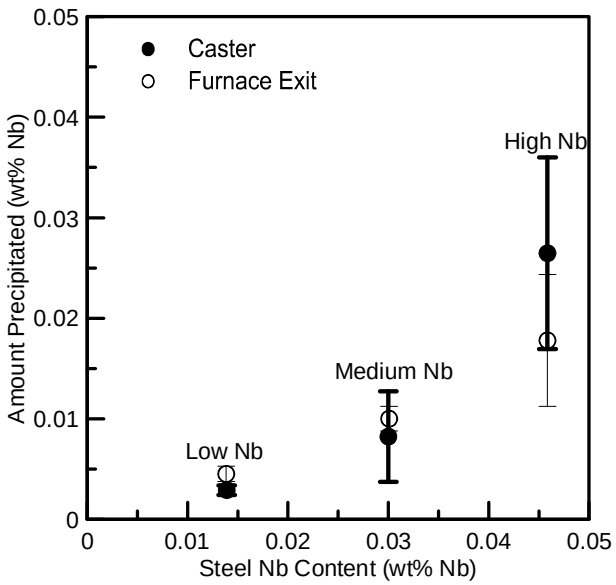

Figure A1 Slab surface/edge location; niobium in precipitate form measured by ICP-AES in wt% of niobium precipitated plotted against the reported alloy content given by the steel producer. Uncertainty analysis represented by the 95% confidence interval.

Table A.1 Uncertainty Analysis for Niobium Precipitation (wt% Nb) Edge Region at *Both Process Locations*

Sample	Precipitate (wt% Nb)	Standard Deviation (wt% Nb)	95% Confidence Interval (wt% Nb)
Low Nb Caster	0.003	0.0007	0.0005
Med Nb Caster	0.008	0.0063	0.0045
High Nb Caster	0.026	0.0133	0.0095
Low Nb Furnace Exit	0.005	0.0011	0.0008
Med Nb Furnace Exit	0.010	0.0017	0.0012
High Nb Furnace Exit	0.018	0.0092	0.0066

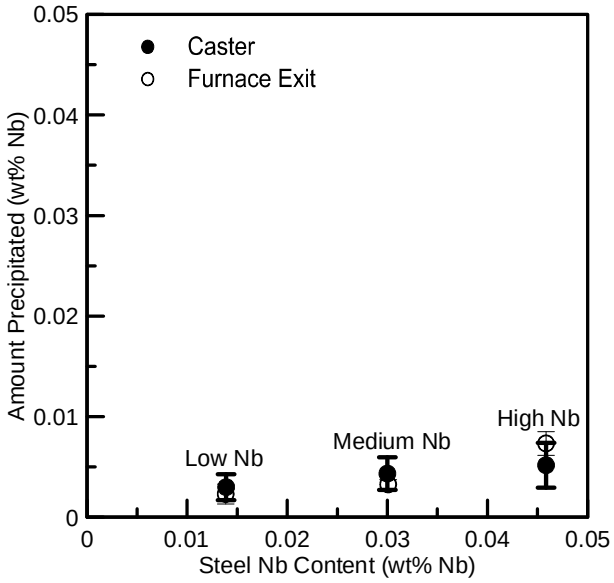

Figure A2 Columnar region; niobium in precipitate form measured by ICP-AES in wt% of niobium precipitated plotted against the reported alloy content. Uncertainty analysis represented by the 95% confidence interval.

Table A2 Uncertainty Analysis for Niobium Precipitation (wt% Nb) Columnar Region at *Both Process Locations*

Sample	Precipitate (wt% Nb)	Standard Deviation (wt% Nb)	95% Confidence Interval (wt% Nb)
Low Nb Caster	0.003	0.0010	0.0013
Med Nb Caster	0.004	0.0013	0.0016
High Nb Caster	0.005	0.0018	0.0022
Low Nb Furnace Exit	0.002	0.0008	0.0010
Med Nb Furnace Exit	0.003	0.0004	0.0005
High Nb Furnace Exit	0.007	0.0010	0.0012

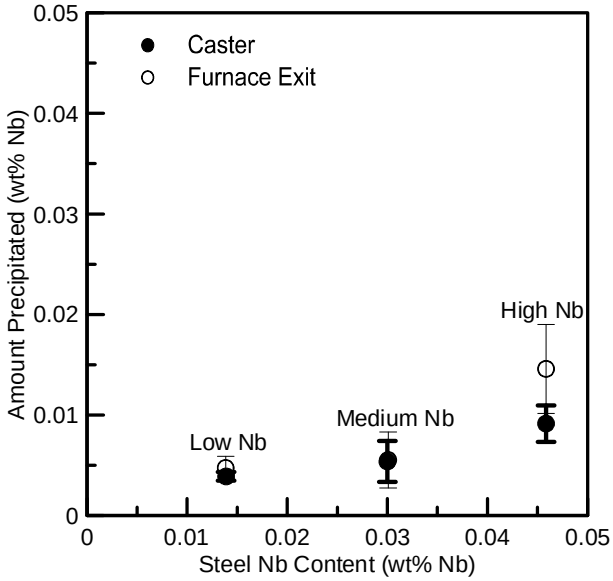

Figure A3 Columnar region; niobium in precipitate form measured by ICP-AES in wt% of niobium precipitated plotted against the reported alloy content. Uncertainty analysis represented by the 95% confidence interval.

Table A3 Uncertainty Analysis for Niobium Precipitation (wt% Nb) Centerline Region at *Both Process Locations*

Sample	Precipitate (wt% Nb)	Standard Deviation (wt% Nb)	95% Confidence Interval (wt% Nb)
Low Nb Caster	0.004	0.0003	0.0004
Med Nb Caster	0.005	0.0016	0.0020
High Nb Caster	0.009	0.0007	0.0018
Low Nb Furnace Exit	0.005	0.0007	0.0012
Med Nb Furnace Exit	0.006	0.0022	0.0028
High Nb Furnace Exit	0.015	0.0018	0.0044

APPENDIX B

APPENDIX B: Number of particles counted, average "equivalent" particle diameter, standard deviation, and calculated K parameter for selected niobium alloys.

Table B1 Precipitate Volume Fraction Measurements based on the K Parameter

Selected Alloy		N	Average X (nm)	σ	K (10^5)
High Niobium	Caster: Edge	574	25	16.0	5.0
	Caster: Columnar	18	78	49.5	1.5
	Caster: Centerline	36	95	65.8	4.8
	Furnace Exit: Edge	415	24	18.6	3.8
	Furnace Exit: Columnar	22	63	39.7	1.2
	Furnace Exit: Centerline	33	142	80.4	8.6
Low Niobium	Caster: Edge	208	10	17.9	0.9
	Furnace Exit: Edge	182	17	9.7	0.7
	Furnace Exit: Columnar	19	45	25.0	0.5
	Furnace Exit: Centerline	34	33	21.0	0.5